

2010

Observations of storm morphodynamics using Coastal Lidar and Radar Imaging System (CLARIS): Importance of wave refraction and dissipation over complex surf-zone morphology at a shoreline erosional hotspot

Katherine L. Brodie

College of William and Mary - Virginia Institute of Marine Science

Follow this and additional works at: <https://scholarworks.wm.edu/etd>



Part of the [Geology Commons](#), [Geomorphology Commons](#), and the [Remote Sensing Commons](#)

Recommended Citation

Brodie, Katherine L., "Observations of storm morphodynamics using Coastal Lidar and Radar Imaging System (CLARIS): Importance of wave refraction and dissipation over complex surf-zone morphology at a shoreline erosional hotspot" (2010). *Dissertations, Theses, and Masters Projects*. Paper 1539616582. <https://dx.doi.org/doi:10.25773/v5-ppcq-gz74>

This Dissertation is brought to you for free and open access by the Theses, Dissertations, & Master Projects at W&M ScholarWorks. It has been accepted for inclusion in Dissertations, Theses, and Masters Projects by an authorized administrator of W&M ScholarWorks. For more information, please contact scholarworks@wm.edu.

Observations of Storm Morphodynamics using Coastal Lidar and Radar Imaging System
(CLARIS): Importance of Wave Refraction and Dissipation over Complex Surf-Zone
Morphology at a Shoreline Erosional Hotspot

A Dissertation

Presented to

The Faculty of the School of Marine Science
The College of William and Mary in Virginia

In Partial Fulfillment

Of the Requirements for the Degree of
Doctor of Philosophy

by

Katherine L. Brodie

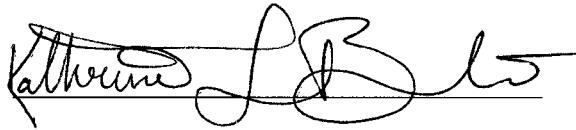
2010

APPROVAL SHEET

This dissertation is submitted in partial fulfillment of

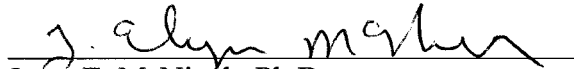
the requirements for the degree of

Doctor of Philosophy



Katherine L. Brodie

Approved, by the Committee, May 2010



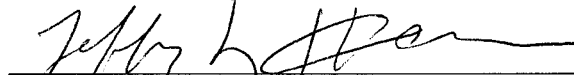
Jesse E. McNinch, Ph.D.
Committee Chairman/Advisor



Carl T. Friedrichs, Ph.D.



Mark R. Patterson, Ph.D.



Jeffrey L. Hanson, Ph.D.
U.S. Army Corps of Engineers
Duck, NC



K. Todd Holland, Ph.D.
Naval Research Laboratory
Stennis Space Center, MS

*To my Dad,
who drove me out to Duxbury Beach
during every Nor'Easter and Hurricane
to see the waves.*

TABLE OF CONTENTS

	Page
ACKNOWLEDGMENTS.....	vii
LIST OF TABLES.....	viii
LIST OF FIGURES.....	ix
ABSTRACT.....	xi
INTRODUCTION.....	1
CHAPTER 1.....	10
Abstract.....	11
1.0 Introduction.....	12
2.0 Background.....	15
2.1 <i>Relevant Remote Sensing Technologies</i>	15
2.2 <i>Development and Design of CLARIS: Robustness during Storms</i>	17
3.0 Methods.....	19
3.1 <i>CLARIS Operational Overview</i>	19
3.2 <i>Radar Morphology Mosaics</i>	21
3.3 <i>Morphology Metrics</i>	22
3.4 <i>Bathymetry Inversion Calculations</i>	24
4.0 Results and Discussion.....	26
4.1 <i>Lidar Topography</i>	26
4.2 <i>Bathymetry Inversion Error Assessment</i>	27
4.3 <i>Morphology Metrics</i>	32
4.4 <i>Seamless Topography and Bathymetry during Storms</i>	34
5.0 Conclusions.....	36
References.....	38
Figure Captions.....	44
CHAPTER 2.....	57
Abstract.....	58

1.0 Introduction.....	59
2.0 Background.....	62
2.1 Surf-Zone Morphodynamics.....	62
2.2 Three-Dimensional Shoreline Shapes.....	64
3.0 Study Area.....	65
3.1 Field Site.....	65
3.2 Reference Line.....	66
4.0 Methods.....	67
4.1 Storm Event & CLARIS Surveys.....	67
4.1.1 CLARIS – Lidar Data Analysis.....	68
4.1.2 CLARIS – Bathymetry.....	69
4.1.3 CLARIS – Morphology Mosaics.....	70
4.2 Wave Model.....	72
4.2.1 Model Setup.....	73
4.2.2 Model Performance: Duck, NC.....	74
4.2.3 Model Outputs.....	76
5.0 Results.....	72
5.1 Morphology.....	72
5.1.1 Shoreline Morphology during the Storm.....	77
5.1.2 Nearshore Bathymetry during the Storm.....	78
5.1.3 Morphological Links between Nearshore Bathymetry and Shoreline Morphology.....	78
5.1.4 Surf-Zone Morphology.....	79
5.2 Wave Model.....	76
5.2.1 Alongshore Variations in Wave Height.....	81
5.2.2 Alongshore Variations in Wave Direction.....	81
5.2.3 Alongshore Variations in Radiation Stress.....	82
6.0 Discussion.....	83
6.1 Three-Dimensional Morphology.....	83
6.1.1 Persistent Nearshore Bathymetry and Shoreline Morphology.....	85
6.1.2 Morphological Coupling of the Shoreline, Surf-Zone and Nearshore Bathymetry.....	87
6.2 Nearshore Hydrodynamics.....	89

6.2.1 <i>Wave Height and Direction</i>	90
6.2.2 <i>Gradients in Radiation Stress and Implications for Flow</i>	91
7.0 Conclusions.....	95
References.....	97
Figure Captions.....	105
CHAPTER 3	124
Abstract.....	125
1.0 Introduction.....	126
2.0 Background.....	129
2.1 <i>Maximum Runup</i>	129
2.2 <i>Wave Breaking in the Surf-Zone</i>	132
2.3 <i>Cross-Shore Sediment Transport</i>	133
3.0 Study Area.....	135
3.1 <i>Field Site</i>	135
3.2 <i>Storm Event</i>	136
3.3 <i>Reference Line</i>	138
4.0 Methods.....	138
4.1 <i>CLARIS: Coastal Lidar And Radar Imaging System</i>	138
4.1.1 <i>Maximum Swash Excursion Observations</i>	139
4.1.2 <i>Foreshore Slope, Shoreline, and Volume Extraction</i>	140
4.1.3 <i>Radar Morphology Mosaics</i>	141
4.2 <i>STWAVE-FP Modeled Wave Parameters</i>	142
4.3 <i>Stockdon et al. [2006] Runup Model</i>	142
5.0 Results.....	143
5.1 <i>Shoreline and Volume Change during the Storm</i>	143
5.2 <i>Foreshore Slope Change during the Storm</i>	145
5.3 <i>Runup Observations and Predictions</i>	146
5.4 <i>Surf-Zone Morphology</i>	150
5.5 <i>Hypothesis Tests of Alongshore Variable Change Metrics</i>	150
5.6 <i>Wave Steepness and Iribarren Number during the Storm</i>	153
6.0 Discussion.....	154
6.1 <i>Comparisons between Predicted and Observed Runup</i>	154
6.2 <i>Temporal Patterns of Beach Evolution during the Storm</i>	157

6.2.1 Importance of Wave Steepness.....	158
6.2.2 Importance of Mean Water Levels.....	160
6.3 Spatial Patterns of Beach Evolution during the Storm.....	161
6.4 Other Metrics for Predicting the Relative Magnitude and Direction of Cross-Shore Sediment Transport during Storms.....	164
7.0 Conclusions.....	167
References.....	170
Figure Captions.....	175
VITA.....	197

ACKNOWLEDGEMENTS

First and foremost, I would like to thank my advisor, Jesse McNinch, for providing me with the opportunity to work with BASIR, his “baby”. Jesse, your positive encouragement, passion for science, unwavering guidance, and most importantly, your vision of the end goal, helped keep me going, especially during the early trying days, when I often found myself face-first in the Kitty Hawk gravel under the Kuboda desperately digging to free BASIR before the rising tide. Most of all, thank you for always taking time out of your often hectic day to listen to, discuss, and thoughtfully critique any new idea I had for CLARIS along the way—alas, chapter 1 is proof that we finally prevailed!

I would also like to thank the faculty members at VIMS, particularly Courtney Harris, Carl Friedrichs, and Jerome Maa, who challenged me academically and forced me to think outside the box—you made me a better scientist and instilled in me a desire to never stop asking questions. I offer sincere gratitude to my committee members for their thoughtful input, tough questions, and constant encouragement throughout this whole process. Special thanks to Carl Friedrichs for suggesting I consider by-passing at my pre-qualifiers, and for always asking questions designed to help both of us learn something new. Todd Holland and Mark Patterson both provided great support and technical advice in the development of CLARIS. Many thanks to Jeff Hanson, a.k.a. WaveMaster, who provided many thoughtful critiques, positive encouragement, and most importantly made sure I had command of “all things waves”—I am honored to be your “Wavelet”!

I would also like to thank the entire crew at the USACE Field Research Facility in Duck, NC who provided tremendous field and technical support throughout this whole project and adopted me into their family. I am indebted to Jason Pipes, who made CLARIS a priority and spent countless hours with me in the field surveying, and to Mike Forte, who provided constant help with the RTK system, laser, and POS-LV—this project greatly benefited from both of your advice, insight, and labor. Many thanks to Ray Townsend for acquiring the blazer, to Brian Scarborough for solving any equipment conundrums, to Eve Devaliere for her programming wisdom with STWAVE, to Cliff Baron and Dan Freer for dealing with the “field” computers, and to Bill Birkemeier, Kent Hathaway, and Chuck Long for their willingness to chat science at a moment’s notice.

Finally to my friends, family, and fur pups—I couldn’t have done this without you or your support, love, and distractions during these last 4 years. I am deeply grateful to my parents for instilling in me a love of the ocean, the will to never give up, and a desire to learn. Mom, from the first science fair project to setting up my dissertation defense, and everything in between, you have been unwavering in your encouragement and support, and always knew whether I needed a hug, a kick in the butt, or a great distraction. Dad, thanks for giving me some of your geekiness, logical thinking, and problem solving skills—I wouldn’t have made it through this project without any of those! Sprague, thanks for all the sisterly distractions, support, and for providing me with a “big city” to come visit. To my friends and lab mates—Amy, Heidi, Jason, Jen, Perkey, and Mike, thanks for all of your help, support, and advice throughout, but mostly, thanks for making me smile and laugh during the tough times. To the fur pups, Polo and Chloe, thank “wooo” for being great running buddies, bedmates, and beach explorers, and for providing endless entertainment and loving kisses, when I needed them most.

To everyone else, I’ve run out of space, but many thanks are in order, so...

*“Here’s a toast to you on the coast and the sailors out at sea:
drink your ales, hoist your sails, ride the wind and think of me.”*

LIST OF TABLES

Table	Page
1. Stockdon et al. [2006] Runup Model Performance.....	180

LIST OF FIGURES

Figure	Page
CHAPTER 1	
1.0 Comparison of radar and video snapshots of a nearshore wave-field during storm conditions.....	47
2.0 Evolution of CLARIS.....	48
3.0 Morphology metric extraction.....	49
4.0 Example wavenumber calculation along a sample cross-shore profile.....	50
5.0 Example of point-cloud lidar topography.....	51
6.0 Bathymetry inversion point by point error assessment.....	52
7.0 Lidar-observed swash and inner surf zone wave parameters.....	53
8.0 Bathymetry inversion spatial error assessment.....	54
9.0 Morphology mosaic and extracted metrics.....	55
10.0 Seamless topography and bathymetry.....	56
CHAPTER 2	
1.0 Location map of study site in Kitty Hawk, NC.....	110
2.0 Nor'Easter wave conditions and CLARIS survey times.....	111
3.0 Coastal Lidar And Radar Imaging System (CLARIS).....	112
4.0 STWAVE spectrum comparison at 5-m AWAC, Duck, NC.....	113
5.0 Shoreline Morphology during the storm.....	114
6.0 Nearshore Bathymetry during the storm.....	115
7.0 Spatial alignment of morphological features.....	116
8.0 Shoreline Morphology to beach slope comparison.....	117
9.0 Shore-parallel bar and surf-zone morphology during the storm.....	118
10.0 Results of STWAVE-FP in Kitty Hawk at the peak of the storm.....	119
11.0 Analysis of alongshore variations in the modeled wave field.....	120
12.0 Relationship between isobath and shoreline curvature.....	121

13.0 Alongshore variations in wave parameters and shoreline morphology.....	122
14.0 Alongshore variations in hydrodynamic forces.....	123

CHAPTER 3

1.0 Physical characteristics of the Nor'Easter.....	181
2.0 Shoreline and volume change during and post-storm.....	182
3.0 Foreshore slope during the storm.....	183
4.0 Observed runup during the storm.....	184
5.0 Spatial predicted and observed runup comparison.....	185
6.0 Relationship between observed and predicted runup.....	186
7.0 Comparison of observed and predicted swash inundation.....	187
8.0 Predicted runup maxima during the storm.....	188
9.0 Surf-zone morphology from radar morphology mosaic.....	189
10.0 Photo and radar characterization of single vs. double barred regions....	190
11.0 Hypothesis tests of alongshore variable beach change metrics.....	191
12.0 Comparison of inter-survey beach volume change and wave steepness.	192
13.0 Iribarren number during the storm.....	193
14.0 Relationship between inner surf zone dissipation and beach volume change.....	194
15.0 Comparison of percentage of time Iribarren number is less than 0.5 (spilling breakers) to volume change.....	195
16.0 Comparison of inter-survey beach volume change and median Iribarren number.....	196

DISSERTATION ABSTRACT

Elevated water levels and large waves during storms cause beach erosion, overwash, and coastal flooding, particularly along barrier island coastlines. While predictions of storm tracks have greatly improved over the last decade, predictions of maximum water levels and variations in the extent of damage along a coastline need improvement. In particular, physics based models still cannot explain why some regions along a relatively straight coastline may experience significant erosion and overwash during a storm, while nearby locations remain seemingly unchanged. Correct predictions of both the timing of erosion and variations in the magnitude of erosion along the coast will be useful to both emergency managers and homeowners preparing for an approaching storm. Unfortunately, research on the impact of a storm to the beach has mainly been derived from “pre” and “post” storm surveys of beach topography and nearshore bathymetry during calm conditions. This has created a lack of data during storms from which to ground-truth model predictions and test hypotheses that explain variations in erosion along a coastline.

We have developed Coastal Lidar and Radar Imaging System (CLARIS), a mobile system that combines a terrestrial scanning laser and an X-band marine radar system using precise motion and location information. CLARIS can operate during storms, measuring beach topography, nearshore bathymetry (from radar-derived wave speed measurements), surf-zone wave parameters, and maximum water levels remotely. In this dissertation, we present details on the development, design, and testing of CLARIS and then use CLARIS to observe a 10 km section of coastline in Kitty Hawk and Kill Devil Hills on the Outer Banks of North Carolina every 12 hours during a Nor’Easter (peak wave height in 8 m of water depth = 3.4 m). High decadal rates of shoreline change as well as heightened erosion during storms have previously been documented to occur within the field site. In addition, complex bathymetric features that traverse the surf-zone into the nearshore are present along the southern six kilometers of the field site. In addition to the CLARIS observations, we model wave propagation over the complex nearshore bathymetry for the same storm event.

Data reveal that the complex nearshore bathymetry is mirrored by kilometer scale undulations in the shoreline, and that both morphologies persist during storms, contrary to common observations of shoreline and surf-zone linearization by large storm waves. We hypothesize that wave refraction over the complex nearshore bathymetry forces flow patterns which may enhance or stabilize the shoreline and surf-zone morphology during storms. In addition, our semi-daily surveys of the beach indicate that spatial and temporal patterns of erosion are strongly correlated to the steepness of the waves. Along more than half the study site, fifty percent or more of the erosion that occurred during the first 12 hours of the storm was recovered within 24 hours of the peak of the storm as waves remained large (>2.5 m), but transitioned to long period swell. In addition, spatial variations in the amount of beach volume change during the building portion of the storm were strongly correlated with observed wave dissipation within the inner surf zone, as opposed to predicted inundation elevations or alongshore variations in wave height.

**Observations of Storm Morphodynamics using Coastal Lidar and Radar Imaging System
(CLARIS): Importance of Wave Refraction and Dissipation over Complex Surf-Zone
Morphology at a Shoreline Erosional Hotspot**

DISSERTATION INTRODUCTION

Substantial development of our nation's coastlines and heightened hurricane activity in the last decade has placed a demand on the scientific community for accurate predictions of coastal change during storms [see Plant et al., 2010]. Unfortunately, monitoring the impact of storms on beaches has mostly focused on analysis of "pre" and "post" storm data, with sparse data *during* storms, leaving researchers with little guidance on how to improve predictive models. Complicating predictions further, storm impact is rarely homogenous along the coastline—storm response can range from rapid shoreline retreat or overwash to beach accretion to little change at all. Areas of the coastline that experience heightened erosion rates relative to areas immediately adjacent to them, are often termed "erosional hotspots", and can occur at the seasonal to decadal scale [Benton et al., 1997], or at the storm-scale [List et al., 2006], in which rapid erosion may be closely followed by accretion in weeks to months post-storm. While explanations exist for many types of erosional hotspots, such as those located near engineered structures (e.g. groins) or inlets [Kraus et al., 2001], hotspots that occur along relatively straight, uninterrupted sections of barrier islands remain unexplained and their behavior difficult to predict.

This dissertation attempts to elucidate some of the behavior of erosional hotspots during storms, through a combination of observations of the entire beach and nearshore system from dune to 1 km offshore and modeling of wave parameters over complex nearshore bathymetry. We first present details on new methodology, Coastal Lidar And Radar Imaging System (CLARIS), a mobile remote sensing system designed to operate and collect data over large distances during storms, and then use the data to analyze

patterns in beach, surf-zone and nearshore morphology with respect to modeled and observed wave parameters during a storm event. The study is conducted along a 10 km region of the Outer Banks of North Carolina previously documented to exhibit both high decadal shoreline change rates, as well as reversing-storm hotspot behavior. Data reveal that wave refraction over complex nearshore bathymetry may induce feedbacks that cause kilometer-scale shoreline embayment and megacusp morphology to persist at both the storm and seasonal scale, and that wave dissipation patterns within the inner surf zone can explain up to 50% of the alongshore variability in erosion during a storm event.

The dissertation is divided into three chapters, and each chapter is presented in standard manuscript format. Chapter 1 has been submitted to *Coastal Engineering* and chapter 2 has been accepted with revisions in the *Journal of Geophysical Research: Earth Surface* [doi: 2009JF001561]. A portion of Chapter 3 has been submitted to *Coastal Sediments '11*. The scientific context and content of each chapter is described next.

1.1 Coastal Storms

Along the east coast of the United States, Hurricanes and Nor'Easters are the two types of storms most likely to damage the beach and dune system that fronts barrier islands and protects property. Hurricanes are low pressure systems that develop in the warm waters of the tropics and threaten the region during the summer and early fall, whereas Nor'Easters are extratropical storms that develop in the mid-latitudes, threatening the coast from North Carolina to Maine during the fall, winter, and early spring. Both types of storms are characterized by strong winds which generate storm

surge and large surface gravity waves that can cause severe erosion when they reach the coastline. While Hurricanes often present more extreme cases and inflict irreversible damage, Nor'Easters can also be extreme, such as Nor'Ida in November of 2009 (a remnant hurricane turned Nor'Easter), the Halloween (Perfect) Storm of 1991, or the Ash Wednesday Storm of 1962. In most cases, however, Nor'Easters are more moderate events that may cause overwash and dune erosion, and often mild property damage. Though they are smaller scale events, research suggests that groups of successive Nor'Easters may play an important role in the medium to long-term morphological evolution of the beach [Lee et al., 1998], and that a slow moving or stationary moderate Nor'Easter may have more total wave power than a fast moving Hurricane [Birkemeier, 1998]. Along the Outer Banks of North Carolina, moderate Nor'Easters frequently batter the coast, inflicting property damage, dune erosion, and beach change, and are considered significant events at the emergency management level.

1.2 During-Storm Observations

Observing beaches during storms presents both physical and scientific challenges, as large storm waves and strong winds prevent traditional vessel-based and in-situ measurement techniques from operating. To address this problem, recent research in the last two decades has focused on developing remote sensing technologies, such as video-imaging [e.g. Lippmann and Holman, 1989; Holman et al., 1993; Holland et al., 1997], airborne lidar [e.g. Irish et al., 2000; Sallenger et al., 2003], and X-band radar systems [Bell, 1999; Ruessink et al., 2002; McNinch, 2007] which are designed to observe the beach and nearshore efficiently and remotely during most conditions. These remote sensing technologies can provide spatially dense observations of coastal morphology and wave

characteristics, including beach topography, nearshore bathymetry, surf-zone wave dissipation, and wave runup at the shoreline [Lippmann and Holman, 1989; Holland et al., 1997; Ruessink et al., 2002; McNinch, 2007]. Information on nearshore and surf-zone bathymetry can be obtained from video and radar observations of wave period and length, by inverting the linear dispersion relationship to solve for depth from wave celerity, in a process known as a bathymetry inversion [Bell, 1999; Stockdon and Holman, 2000; Holland, 2001; Plant et al., 2008]. In addition, observations of wave runup can be made by examining the leading edge of the swash from sequential video [or radar] images [e.g. Aagaard and Holm, 1989], information that quantifies storm induced water levels [Stockdon et al., 2006].

Lidar data is especially useful in the analysis of pre- to post-storm coastal changes [e.g. Sallenger et al., 2004; Sallenger et al., 2006], as well as in beach volume calculations [Irish et al., 1996], as the spatially dense data helps to reduce errors associated with interpolation and data aliasing common to more traditional profiling techniques [Plant et al., 2002; Bernstein et al., 2003]. In addition, terrestrial-based lidar can now be collected on moving vehicle platforms, enabling rapid data collection of beach topography over large areas during storms when low visibility and high winds prevent airborne collection. While all three types of technologies have advantages and drawbacks, image rectification processes for terrestrial lidar and X-band radar make them more readily transferrable to a mobile platform, which expands spatial data collection capabilities when compared to fixed installations.

In chapter 1, we present Coastal Lidar and Radar Imaging System (CLARIS), a fully-mobile system designed to operate during storms and collect topography data of the beach from a terrestrial laser scanner as well as bathymetry data from radar-derived wave celerity measurements and surf- and swash-zone morphology data from time-averaged

radar images. We provide information on the development of CLARIS, testing of various methodologies, and provide examples of applications of the data to coastal nearshore studies.

1.3 Storm-Resilient Morphology

Two decades of video images of the nearshore in combination with earlier research suggest that surf zones shorelines transform from three-dimensional forms during calm conditions to two-dimensional linear forms during storms in response to high waves [Wright and Short, 1984; Lippmann and Holman, 1990; Ruessink et al., 2000; Van Enckevort et al., 2004]. There is growing evidence, however, that some previously unexplained hotspots are related to complex nearshore bathymetric features, which may persist through storm events [McNinch, 2004; Schupp et al., 2006; Mielis, 2007]. In particular, along a 5-km region in Kitty Hawk and Kill Devil Hills, NC, a series of shore-oblique trending sandbars and troughs exists, which extend from 15 m of water depth into the surf zone in 5 m of water depth. This 5-km region is encompassed by the 10 km study site analyzed in this Dissertation.

While correlations between these bathymetric features and heightened erosion at the shoreline are well established, how the features influence shoreline morphology in the region during storms and over longer time-scales are unknown. Shoreline perturbations at many scales (from beach cusps to megacusps) are often associated with bathymetric features [e.g. Dolan, 1971; Sonu, 1973; Wright and Short, 1984; Short, 1999; Bender and Bean, 2004; Coco et al., 2005; Thornton et al., 2007], and debate regarding their formation continues. Some features, such as the megacusps that often develop in

response to dredged borrow-pit holes are well understood [Bender and Dean, 2004]. In contrast, the processes responsible for the cusp and embayment features that often develop congruently with rip currents and undulations in the shore-parallel bar are thought to be either forced by hydrodynamic processes (e.g. edge waves) or self-organized by morphodynamic feedbacks [see Coco et al., 2005 for a good discussion]. Less information exists on the formation of larger scale features such as alongshore sand-waves or megacusps [Sonu, 1968; Verhagen, 1989; Dolan, 1971], and how they evolve through storms despite the fact that they may leave portions of the coast significantly more susceptible to erosion during storms [e.g. Thornton et al., 2007].

In chapter 2, we use bathymetric inversion data from CLARIS to document the persistence of complex surf-zone and nearshore bathymetry during a Nor'Easter, and identify a spatial link between storm-resilient shoreline undulations (megacusp and embayment morphology) and the persistent shore-oblique bars and troughs. In addition, we use the STeady-state spectral WAVE model (STWAVE) to model wave refraction during the storm and suggest a possible morphological coupling [e.g. Castelle et al., 2010]. We speculate that geologically controlled bathymetry may force hydrodynamic gradients that lead to self-organized morphology and flow patterns that are able to withstand high energy events, preventing traditional storm linearization of the shoreline and surf zone from occurring.

1.4 Predicting Spatial and Temporal Variations in Beach Response to Storms

Predicting the response of the beach to storms, particularly in regions known to experience heightened erosion, at correct temporal (e.g. when will the erosion occur?)

and spatial scales (e.g. where will the most erosion occur?), is paramount for the effective management of coastal areas. Storm impact is often analyzed by determining change between surveys conducted “pre” (often many days to weeks or even months prior) and “post” (waiting for wave conditions to be favorable for vessel operations) storm surveys. Storm-induced cross-shore transport is traditionally expected to be offshore due to offshore directed undertow [Thornton et al., 1996; Gallagher et al., 1998], whereas onshore transport in calm conditions is expected due to velocity skewness and wave asymmetry [Thornton et al., 1996; Roelvink and Stive, 1989; Elgar et al., 2001; Hoefel and Elgar, 2003; Ruessink et al., 2007]. Earlier anecdotal reports have indicated, however, that significant amounts of sediment may return to the beach while wave conditions are still energetic, suggesting that onshore transport occurs during relatively energetic conditions and that the pre/post-storm approach may underestimate the storm’s real impact [Birkemeier et al., 1979]. Unfortunately, a lack of quantitative topography data in the midst of storms has prevented confirmation of this hypothesis.

In response to the severe coastal change inflicted by hurricanes in the last decade, the U.S. Geological Society has implemented a coastal change hazards research program which focuses on monitoring and predicting the extent of topographic change during extreme storms [see Plant et al., 2010 for an example]. The model they use is based on the barrier island storm impact model devised by Sallenger [2000], in which mean and wave-driven water levels are compared with beach morphology alongshore to determine the impact regime of the storm (e.g. swash, dune collision, overwash, or inundation). Wave-driven extreme runup maxima are calculated using an empirical relationship derived by Stockdon et al. [2006] which relates the two-percent exceedence elevation of

runup to foreshore slope, wave height, and wave length. While the storm-impact models perform better than random models (54% accuracy compared to 33%), there is room for improvement [Stockdon et al., 2007]. Unfortunately, it is presently unclear whether the high error stems from poor predictions of maximum runup, out-dated antecedent beach morphology, or an overly simplified modeling approach.

In Chapter 3, we use semi-daily CLARIS observations of the beach during a moderate Nor'Easter to identify spatial and temporal patterns in beach change and maximum swash excursion throughout a storm, and use these data to test three hypotheses for longshore variable beach change during storms, including the “relative runup” approach described above. Our data suggest that the timing of erosion and accretion during storms may be strongly influenced by wave steepness, with more than half of the original shoreline erosion recovered along 50% of the study site within 24 hours of the storm peak as waves remained large (>2.5 m), but transitioned to long period swell. In addition, the configuration of the inner surf zone and resulting wave dissipation amounts seemed to better predict spatial variability in beach volume change, when compared with alongshore variations in predicted relative runup or modeled breaking wave height.

CHAPTER 1

Coastal Lidar And Radar Imaging System (CLARIS):

A mobile, integrated system for measuring nearshore wave parameters,
bathymetry, and beach topography during storms

Manuscript citation: Brodie, KL and McNinch, JE (*Submitted*). Coastal Lidar and Radar Imaging System (CLARIS): A mobile, integrated system for measuring nearshore wave parameters, bathymetry, and beach topography during storms, Coastal Engineering.

ABSTRACT

Mapping systems that are capable of quantitatively measuring the elevation of the sub-aqueous and sub-aerial coastal system during storms when wave heights are large and visibility is reduced are rare. As a result, spatially extensive and temporally dense quantitative data on the evolution of beaches and surf-zones during storms are lacking, preventing adequate assessment of predictive numerical models, and leaving a reliance on "pre" and "post"-storm data sets. We present Coastal Lidar and Radar Imaging System, CLARIS, a fully-mobile system designed to operate during storms and collect topography data of the beach from a terrestrial laser scanner as well as bathymetry data from radar-derived wave celerity measurements and surf- and swash-zone morphology data from time-averaged radar images. In addition, the combined system provides information on wave spectra, including direction and period from the radar data, and wave height within the inner surf-zone from lidar data. CLARIS can survey 10-km of coastline in 2 hours and provide bathymetry from 2-m water depth to 1.2 km offshore to within 11% accuracy as well as topography of the beach and dune to within 10 cm. Surf-zone morphology metrics, such as the position of shore-parallel bars and maximum swash excursion are objectively extracted from time-averaged mosaics. Current operational limits to CLARIS include: (1) beach conditions to be drivable, (2) precipitation to be no more than a light rain, and (3) the nearshore wave-field must be sufficiently large to interact with the seafloor and be roughened at the surface by strong winds.

1. INTRODUCTION

Beaches and surf zones are dynamic environments that change rapidly during storms in response to elevated water levels and changing wave energy. Demand for accurate model predictions and a physics-based understanding of storm-induced effects (e.g. beach erosion, overwash, surge, and runup) has risen recently, following a decade (1996 to 2005) of heightened Atlantic hurricane activity that was one of the most costly in the last century [Pielke et al., 2008]. Unfortunately, high-resolution measurements of surf-zone and beach morphology, over both short enough temporal scales and large enough spatial scales to accurately develop and assess predictive models, are lacking, due mostly to the difficulty of observing beaches and surf-zones during storms with traditional surveying methods. To address this problem, extensive work over the past two decades has been devoted to developing remote sensing technologies, such as video-imaging [e.g. Lippmann and Holman, 1989; Holman et al., 1993; Holland et al., 1997], airborne lidar [e.g. Irish et al., 2000; Sallenger et al., 2003], and X-band radar systems [Bell, 1999; Ruessink et al., 2002; McNinch, 2007] that are capable of observing the beach and nearshore under almost any condition. Most of these efforts, with the exception of airborne lidar, however, are fixed installations, which limits the spatial extent of observations, and lidar is not safely flown during storm conditions. In contrast, we have developed CLARIS: Coastal Lidar and Radar Imaging System, a fully mobile system that integrates two state of the art remote sensing technologies, a terrestrial laser scanner and X-Band radar, using precise motion and location information. We demonstrate that CLARIS is a robust system capable of rapidly (up to 10 km alongshore in 2 hours) and quantitatively measuring: beach and dune topography (accuracy of 10 cm), nearshore bathymetry from radar-derived wave celerity measurements (10% accuracy), and surf-and swash-zone morphology from time-averaged radar images during storms.

Cross-shore profiling, a traditional beach surveying technique, uses field measurements of beach elevation and surf zone bathymetry to quantify nearshore morphology in the cross-shore direction at a particular point alongshore. Mounting bathymetric surveying equipment such as echo-sounders on a variety of platforms—jet-skis [Dugan et al., 2001], the Coastal Research Amphibious Buggy (CRAB) [Birkemeier and Mason, 1984], or amphibious vehicles (e.g. Lighter Amphibious Resupply Cargo (LARC)), have enabled this type of data to be collected in the surf-zone in waves up to 2 m (<http://www.frf.usace.army.mil/aboutUS/vehicles.shtml>). While cross-shore profiling enables researchers to model two-dimensional cross-shore movement of bars [Sallenger et al., 1985; Thornton et al., 1996], as well as study seasonal cycles of erosion and accretion [Aubrey, 1979; Birkemeier, 1984], the technique suffers from an inability to accurately characterize the three-dimensional nature of the nearshore system and how it evolves during storms. While swath bathymetry systems mounted on the LARC [McNinch, 2004] can accurately map three-dimensional bathymetries in shallow environments, they necessitate fairly calm conditions to work most effectively, and often are time-consuming to complete.

In addition, the collection of wave data over spatially extensive areas, particularly within the surf-zone, presents its own challenges. Traditional oceanographic methods of wave data collection in the nearshore, such as the placement of instruments on the bottom (e.g. AWACs, and pressure sensors), are less effective in the surf zone, as wave breaking processes and strong alongshore and cross-shore currents make the instruments difficult to maintain. The identification of spatial variations in the wave-field is often left to models, as instruments placed on the bottom only provide point measurements of the wave parameters. Even the rare cross-shore array of instruments [e.g. Hanson et al., 2009] only provides information along one transect, making identification of wave refraction patterns and the alongshore length scale of wave groups [e.g. Reniers et al., 2004] difficult. Within the inner

surf-zone, wave information is often constrained to height information, as pressure sensors are more easily maintained (through burial), than AWACs or Aquadops, which must be mounted such that they can withstand the force of breaking waves and remain clear of sediment.

Remote sensing technologies eliminate many of the problems of collecting *in-situ* measurements in the surf zone and can provide spatially dense data on coastal morphology, beach topography, nearshore bathymetry, and shoreline runup characteristics. Video imaging and X-band radar rely on similar principles: breaking and non-breaking waves create image intensity patterns across the surf-zone and nearshore that are exploited using a variety of techniques to provide information on wave parameters (including period, direction, speed, and dissipation) across the surf-zone and at the shoreline [Lippmann and Holman, 1989; Holland et al., 1997; Ruessink et al., 2002; McNinch, 2007]. Time averages of video frames (or radar images) provide maps of surf-zone dissipation which can be used as a proxy for shoreline and sandbar morphologies, information that is analyzed with respect to surf-zone morphodynamics [Lippmann and Holman, 1990; Ruessink et al., 2000; van Enckevort and Ruessink, 2003; Alexander and Holman, 2004; Ranasinghe et al., 2004; Van Enckevort et al., 2004; Holman et al., 2006] and integrated into realtime bathymetric models (e.g. Beach Wizard, see [see Aarninkhof et al., 2005; van Dongeren et al., 2008]). Sequential video time-stacks can also be used to study swash motions including runup-spectra, swash velocities, and maximum runup elevations [Aagaard and Holm, 1989; Holland et al., 1995; Holland, 1998; Holland and Holman, 1999; Ruggiero and Holman, 2004; Stockdon et al., 2006]. In addition, measurements of wave celerity, c , (or, alternatively, wavelength, L , since $c = L/T$, where T = wave period) from sequential radar passes [Bell, 1999] or video frames [Stockdon and Holman, 2000; Holland, 2001; Plant et al., 2008] can be used to explicitly calculate bathymetry by exploiting the intermediate and shallow-water depth dependence of wave

speed in the nearshore, referred to as a bathymetric inversion. Mobile systems, such as Bar and Swash Imaging Radar (BASIR) [McNinch, 2007] and beach or airborne Lidar systems [Stockdon et al., 2002], are particularly useful at quantifying the alongshore variability of beaches and surf zones due to their extensive range and easy mobility.

The objectives of this paper are to describe a new tool, CLARIS, that rapidly measures beach topography and nearshore bathymetry during storms and to assess its accuracy. We begin with a brief background on lidar and radar remote sensing technologies as well as some details on the design and development of a robust system for during-storm operation. We then present a description of CLARIS and its operation, as well as details on data analysis techniques including the extraction of morphology metrics and bathymetry estimates. An analysis of the accuracy of the bathymetry inversion techniques and how they can be improved through lidar-measured wave parameters, in addition to the success of the morphology metric extraction, follows. We end with a brief example of merged laser-derived topography and radar-derived bathymetry.

2.0 BACKGROUND

2.1 Relevant Remote Sensing Technologies

Lidar, radar, and video imaging are the three remote sensing technologies used most often by coastal researchers to study the beach and nearshore. Lidar and radar are “active” remote sensing systems that send out electromagnetic waves and measure the length of time it takes to return, providing information about the position or elevation of a certain feature. Video, in contrast, is a “passive” remote sensing system that merely records intensities of reflected light. Airborne lidar systems are used to rapidly and accurately map beach topography [Sallenger et al., 2003; Sallenger et al., 1999; Stockdon et al., 2002; Mitasova et al., 2010] and nearshore bathymetry [Setter and Willis, 1994; Lillycrop et al., 1996; Irish and

White, 1998; Irish et al., 2000;], and are especially useful in the analysis of pre- to post-storm coastal changes [e.g. Sallenger et al., 2004; Sallenger et al., 2006]. In addition, Irish and others [1996] demonstrate that the high data density typical of lidar systems reduces error in volumetric calculations when compared with sparser, more traditional cross-shore profiles. Airborne lidar systems, however, cannot be flown during storms, when bathymetric and topographic data are needed most to ground-truth models. In addition, airborne lidar is of limited use for mapping surf-zone bathymetry when water turbidity is high and the surf zone is fully dissipated, as most of the light is attenuated in the water column before it reflects off of the bottom [Irish and White, 1998]. Despite these drawbacks and high costs, airborne lidar systems have been the best method to densely acquire topographic data over large spatial areas. Terrestrial laser scanners are a ground based version of airborne lidar that are gaining popularity for analyzing beach morphology changes [Pietro et al., 2008]. Historically, terrestrial laser scanners were static sensors that were often cumbersome to survey large areas with, but recent technological advances have enabled mobilization through integration with motion sensing units. The ability to mount terrestrial laser scanners on ground-based vehicles makes rapid mapping of beach topography less expensive and more accessible than traditional airborne techniques.

X-band radar technology is widely used to determine wave properties and surface currents in open and coastal oceans, and recently has been employed in the nearshore [Bell, 1999; Ruessink et al., 2002; Haller and Lyzenga, 2003; McNinch, 2007]. The basic premise of applying radar technology in shallow water environments is that small capillary waves and ripples on the sea surface cause Bragg-scattering of the incoming radar energy, which is then modulated by the incoming surface gravity waves. This creates what is often termed “sea-clutter:” alternating patterns of high and low intensity radar returns corresponding to the incoming waves. In addition, “sea-spikes,” high intensity radar returns off of the foamy,

rough surface of breaking waves, are also produced and often are the dominant backscatter source in the radar image [Haller and Lyzenga, 2003]. Averaging the radar images over time produces similar images to Argus video systems [Lippmann and Holman, 1989], such that areas of high intensity returns correspond to areas of breaking waves (sandbars and swash), and areas of low intensity returns correspond to areas of less breaking (deeper troughs) [Ruessink et al., 2002; McNinch, 2007]. Initial research suggests that radar observations are well suited for use during storms when optical signals suffer more interference, both from relict foam on the sea surface [Haller and Lyzenga, 2003], or rain and mist. In addition, radar observations can be collected at any time as daylight is not needed, and are more easily rectified in space, especially when the field of view is constantly changing (i.e. on a mobile platform). Drawbacks to radar include the loss of horizontal resolution in the far range, the attenuation of the signal in heavy downpours, a reliance on extremely accurate heading information (expensive) for proper image rectification, and a need for roughened water surfaces for reflection success.

2.2 Development and Design of CLARIS: Robustness during Storms

Since one of the desired attributes of CLARIS is the ability to robustly observe the nearshore wave-field during storms, we first needed to verify that radar can adequately distinguish between relict foam and propagating bores in extremely dissipative surf-zones. While McNinch [2007] show that X-band radar can successfully reproduce sandbar and swash configurations during 3-m waves, wave-field information from single rotation images (needed for the bathymetry inversion exercises) were not previously investigated. In addition, while Haller and Lyzenga [2003] investigate the sensitivity of radar returns to relict foam, their data only include observations of waves

with heights < 1 m. To investigate the robustness of radar during storms, we compare radar snapshots of the nearshore wave field at the U.S. Army Corps of Engineer's Field Research Facility (FRF) in Duck, NC with video snapshots of the region from the Argus tower during 4-m waves on 25 September 2008 (Figure 1A and B, respectively). In contrast to the rain-obscured Argus image (Figure 1B), wherein the surf-zone is a mesh of dissipating bores and relict foam, the radar image (Figure 1A) shows clearly delineated wave-forms (the higher intensity returns) across the surf-zone. This example corroborates the previous work of McNinch [2007] and Haller and Lyzenga [2003], and demonstrates that even during 4-m storm waves in light-rain, radar can adequately distinguish propagating bores from relict foam in a dissipative surf-zone. This also confirms the choice of radar, as opposed to video, for a storm-oriented mobile remote sensing system.

To exemplify the challenges associated not only with designing a mobile system that can remotely measure wave parameters and beach topography during storms (e.g computer hardware, writing acquisition software, etc.), we include a brief description of the difficulties in simply selecting a vehicle platform that could successfully traverse the beach through a variety of substrates during elevated water levels. Earlier versions of the system include: (1) an ATV plus associated trailer that houses the radar and computers (Figure 2A), (2) an RTV with the radar and computers on the back (Figure 2B), (3) a stackable configuration in which the RTV is secured to the deck of the FRF's LARC (Figure 2C), and finally, (4) the current configuration on a military issue, 24-volt, diesel, 1986 Chevy Blazer (Figure 2D). Versions (1) and (2) perpetually ended up stuck in the sand due to a combination of low gear power, tire inadequacy, and low ground clearance.

Version (3), though successful at navigating the beach during storms, is inefficient and expensive to operate. Version (4)'s success can be attributed to its four-wheel drive gear ratios, light weight, and wide-tires that create an optimal vehicle for beach driving. In addition, the added height of the military blazer (when compared with the ATV and RTV) also decreases problems of radar shadowing in the far range from irregular beach topography, such as high berms or beach cusp horns. Though CLARIS can successfully drive through the occasional swash inundation on common beach substrates (tested in water levels up to ~ 30cm), it is not the best vehicle for beach driving during the most extreme conditions, such as those encountered during hurricane landfalls. In order to make the system fully mobile during extreme storms, the system will be mounted on a new, tracked-vehicle platform that is capable of operating while inundated in up to ~1.5m of water and can easily traverse debris-laden beaches (Figure 2E).

3.0 METHODS

3.1 CLARIS Operational Overview

CLARIS couples simultaneous collection of radar data in the nearshore with laser data of the beach, enabling mapping of near-seamless topography and bathymetry from the dune to 1 km offshore, as well as collection of wave parameters including direction and period across the nearshore, and wave height within the inner surf-zone. Roughly 10 km of beach is surveyed in 2 hours, and surveys are conducted in the two hour window centered at low tide to maximize beach width for driving and ensure relatively constant water level during the surveys.

The radar component of CLARIS is BASIR [McNinch, 2007], a mobile 4kW X-band (9410 +/- 30 MHz) beach radar system designed to remotely map the swash, nearshore bars,

and nearshore wave field. BASIR is updated in this system to include time-stamps associated with each radar shot for improved rectification and calculation of azimuth resolution during high-wind conditions. BASIR data is herein referred to as “radar data”. Radar data is collected at predetermined locations along the beach spaced roughly 800-1000m apart. The heading angle of the initial radar pulse is recorded using an Applanix© POS-LV motion system with an accuracy <0.5 degrees, and the location of the center of the radar image is recorded using Real-Time Kinematic GPS to 10 to 15 cm accuracy. At each location, the radar completes 256 rotations at ~ 0.83 Hz, for a sampling duration of about 5 minutes. Though we recognize that this sampling time will not capture the longest period surf-beat oscillations, Guza and Thornton [1985] observe that on beaches with incident waves ranging between 0.05 and 0.15 Hz, 90% of infragravity energy occurs in frequencies between 0.005 and 0.05 Hz. Thus, our sampling duration of ~ 305 s enables averaging over most variations in wave breaking due to wave groupiness and surf beat and provides a reasonable balance between sample duration and spatial coverage. Furthermore, since radar stops are spaced 800-1000 m apart and the range of the radar is 1.2 km, the overlap regions obtain a discontinuous, cumulative total of about 10 minutes (~ 610 s). Surf-zone morphology metrics, waterline position, bathymetry, and wave period and direction are estimated from the radar data.

A Riegl 3D Terrestrial Laser Scanner (Riegl VZ-390i) scans the topography starboard of the vehicle during transit between radar stops. Terrestrial laser scanner data will be referred to as “lidar data” throughout the remainder of this paper. An Applanix© POS-LV motion system is used to measure motion (pitch, roll, and orientation) of the vehicle during the lidar survey, which are post-processed using Applanix© PosPAC software for increased accuracy. The motion data are then combined with the GPS position to rectify the lidar data. Survey precision is on the order of 1.3 cm and accuracy is ± 5 -10 cm. Point-cloud density

is ~30 to 40 points per m², with higher density in the near-range and cross-shore direction. Since surveys are generally conducted while transiting shore-parallel, the lidar is aimed seaward to record foreshore topography at the same time as the radar survey. After all locations have been surveyed with the radar, CLARIS is driven back down the beach in the opposite direction so the lidar can scan the upper beach and dune, the portion of the beach least likely to have changed during the 2-hr radar survey. The lidar surveys are first edited to remove any surveyed beach-goers, birds, houses, spikes, and waves, and then gridded in IVS Fledermaus 7.0 using a weighted moving average (1 m grid, 1 m weight). Beach morphology metrics, such as beach slope, shoreline contours, and beach volume, are then extracted from and compared between consecutive lidar surveys.

3.2 Radar Morphology Mosaics

Raw, binary radar files are read into MATLAB and organized into range, azimuth, and rotation (time) space. Data manipulation on the radar returns is performed to address both range fall-off and azimuth scatter artifacts. The data are corrected using an empirically defined cubic fit (eqn. 1), to ensure that similar objects at different distances from the radar produce similar return values:

$$I_{corrected}(r, a, t) = I(r, a, t) * (1.5e^{-7}r^3 + 1.2e^{-3}r^2 + 1.5r + 188.5) \quad (1)$$

where r is range (distance from the radar, ranging from 3 to 1200 m in steps of 3m), a is each azimuthal radar bearing, t is each rotation, and $I(r, a, t)$ is the radar intensity at each range, azimuth, and time location. Range resolution is 3 m, a function of analogue to digital sampling using a 50MHz card, and temporal resolution is 1.2 s. The radar images are then

rectified through a polar transformation from azimuth-range space using heading and position information, to Cartesian coordinates (e.g. NC State Plane Easting and Northing, Horizontal Datum: NAD1983), and the centers of the radar images are removed to prevent problems with over-saturation in the near range (Figure 3A). To create the morphology mosaics, the radar data is first gridded into a study-site wide, pre-defined alongshore/cross-shore/time three-dimensional grid, using a nearest neighbor gridding algorithm (Figure 3A-B) to 3-m spatial resolution. To accommodate overlap between stops, the temporal domain is extended to 512 samples so that information from two stops alongshore (256 samples from each) can be used. While this does not create a continuous 512-point time series, and thus harmonic shifts in wave parameters may exist, the extra data are useful for averaging over surf-beat and infragravity fluctuations. Radar returns at each grid node are then averaged in time, and smoothed in the alongshore direction using a 30-m weighted-moving average, to create a seamless morphology map of the area.

3.3 Morphology Metrics

Surf-zone morphology metrics, such as bar and swash position (from radar-observed dissipation peaks), as well as the radar-defined waterline, are extracted from the time-averaged morphology mosaics by analyzing the shape of each cross-shore, time-averaged, radar intensity profile at every 3-m location alongshore. Figure 3C shows an example of a time-stack of radar intensities at a particular location alongshore—the incoming waves are visible as the streaking white lines across the image. By averaging these time-stacks through time, a cross-shore profile of radar intensities can be created (Figure 3D) which has peaks and valleys that often correspond to various morphological features. Peaks in radar intensities correspond to highly dissipative areas, such as the shore-parallel bars and swash

zones, where as the valleys correspond to the beach and nearshore shore-parallel troughs. Peaks are identified using the “findpeaks” function in MATLAB which compares each data point in the profile to its neighbors and, if it is larger than both neighbors, classifies it as a peak. Depending upon the data, some initial smoothing of the time-averaged profile (e.g. a 10-m weighted moving average) or threshold values are set to smooth out any noise in the signal. To classify the peaks, their position relative to the valley of the beach is noted: the swash peak is identified as the first peak seaward of the beach (pink dot and line in Figure 3C, D), the next peak after the swash is the first shore-parallel bar (e.g. the blue dot and line in Figure 3C,D), and any subsequent peaks correspond to outer bars (e.g. the orange dot and line in Figure 3C,D). While this methodology provides a good indicator of the number of offshore bars, it is important to note that the peak in dissipation over the bars may not necessarily correspond to the peak of the sandbar itself, as variations in water-level and wave-height, in addition to bathymetry, can influence where waves break [Ruessink et al., 2002; McNinch, 2007]. The position of the maximum swash excursion during the sampling time is found by identifying the first location with a positive slope seaward of the valley of the beach (yellow line and dot, Figure 3C-D), as this location represents the most landward position that the high intensity swash reached during the time of observations. Edges of features are found by identifying locations of maximum slope in the cross-shore intensity profile (e.g. the offshore edge of the inner bar in Figure 3D is shown by the green dot).

Once the morphological features are identified, morphology metrics pertinent to the identified research questions can then be extracted from the data. For example, to determine the number of offshore bars at any given location alongshore, the number of peaks seaward of the first swash peak is counted. To determine the width of the inner surf-zone, the cross-shore distance between the maximum observed swash excursion and inner-bar edge is found.

In addition, integrals under the time-averaged radar intensity curve may be useful proxies for wave dissipation across the surf-zone.

3.4 Bathymetry Inversion Calculations

To obtain bathymetry estimates from the radar data, wave celerity is calculated from observations of radar intensity time series using a simple 2D cross-shore cross-spectrum correlation analysis [Stockdon and Holman; Plant et al., 2008]. Each radar rotation is gridded into an 1.8 km alongshore by 1.2 km cross-shore 5 m spaced grid, and time series of radar intensities ($dt = 0.83$ Hz) are extracted at each grid node. Each time series is band-pass filtered (0.05 to 0.2 Hz), and each spatial grid (rotation) is smoothed in the alongshore direction using a 50-m weighted moving average to create more coherent wave crests. The cross-spectrum, P_{xy} , (eqn. 2a, Figure 4A) and coherence estimate, C_{xy} , (eqn. 2b, Figure 4B) are then calculated between alternating grid nodes in each cross-shore profile (e.g. node 1 to node 3, node 2 to node 4, etc.) :

$$P_{xy}(x_{i,j}, f) = Y(x_{i,j}, f)Y(x_{i+2,j}, f)^* = A_{x_{i,j}, f} \exp(\sqrt{-1}\phi_{shift_{x_{i,j}, f}}) \quad (2a)$$

$$C_{xy}(x_{i,j}, f) = \frac{|P_{xy}(x_{i,j}, f)|^2}{P_{xx}(f)P_{yy}(f)} \quad \text{where } y = x_{i+2} \quad (2b)$$

where Y indicates the Fourier transform, $*$ indicates the complex conjugate, A is the amplitude, ϕ_{shift} is the phase shift, i is the cross-shore position index, j indicates which cross-shore profile (alongshore position), and f is frequency. To find the frequency of the most coherent wave, C_{xy} is then summed alongshore for each cross-shore position, and

the frequency of maximum coherence is found for each cross-shore position. The mode of these frequencies is identified as the frequency of the most coherent wave (f), and the corresponding phase shift at that frequency is extracted from the cross-spectral estimate for all grid nodes. These phase shift measurements are then divided by Δx (the distance between the cross-spectral correlated time series) to find the wavenumber, $k = 2\pi/L = \phi_{shift} / \Delta x$ (Figure 4C). This method of estimating wavenumber assumes shore-parallel waves with no wave-current interaction, and only utilizes information from the most coherent (dominant in radar signal) wave form.

Once wavenumber is estimated at each grid node, the linear dispersion equation (eqn 3a) is inverted and solved for h , water depth (eqn 3b):

$$\omega^2 = gk \tanh(kh) \quad (3a)$$

$$h = \frac{1}{k} \tanh^{-1}\left(\frac{\omega^2}{gk}\right) \quad (3b)$$

Where $\omega = 2\pi f$ = wave radian frequency of maximum coherence, and $g = 9.8 \text{ m s}^{-2}$. As waves approach the shoreline, they become non-linear and their abrupt increase in height makes them travel faster than what is predicted by linear dispersion theory, a process known as amplitude dispersion. If this is not taken into account, the depths predicted by the above method are too deep when compared with the actual water depth [Holland, 2001]. To combat this problem, a modified cnoidal wave theory equation (eqn 4a) [Holland, 2001] is solved iteratively within the surf zone:

$$h = \frac{\left(\frac{\omega}{k}\right)^2}{g - \alpha H} \quad (4a)$$

$$\text{with } H = \gamma h, \gamma = 0.4 \text{ [Thornton and Guza, 1982]} \quad (4b)$$

To prevent a step-like feature where linear dispersion and modified cnoidal wave theory meet, equation 4a is used from the shoreline out to the theoretical breaking wave depth, h_{BW} , and equation 3b is used from the offshore edge up to $h_{BW} - I$, and spatial interpolation algorithms are used to fill in the gaps between these regions. The water depths are then subtracted from a measured water (tide) level at a nearby tide station, and thus referenced to a vertical datum (e.g. NAVD88). Bathymetry from each stop is then de-spiked and mosaicked together alongshore in IVS Fledermaus 7.0 using a weighted moving average (5-m grid, 15-m weight).

4.0 RESULTS AND DISCUSSION

4.1 Lidar Topography

The example lidar data shown in Figure 5A, B demonstrates the superiority of lidar to more traditional surveying methods: lidar provides complete spatial coverage and high data density, enabling three-dimensional features such as the beach cusps in Figure 5B to be robustly mapped without the data aliasing errors common in traditional survey methods [Plant et al., 2002]. One of the drawbacks to lidar data is a time-consuming editing process, as any beachgoers or cars present on the beach at the time of surveying (Figure 5B) are also mapped. In addition, the removal of houses is necessary to ensure proper dune elevations during gridding, and sand-fences often make the base of the dune difficult to identify. Once the lidar data is edited, it is gridded, and pertinent elevations contoured—e.g. the MHW shoreline is shown in Figure A-B (white line). In addition, the gridded lidar files can be transformed into alongshore/cross-shore space and profiles extracted at 1-m increments.

From these profiles, beach slopes and volumes are easily calculated, and changes are mapped between sequential surveys.

4.2 Bathymetry Inversion Error Assessment

The accuracy of the bathymetry inversion is assessed through a comparison with a swath interferometric bathymetry survey of a 5-km section of nearshore in Kitty Hawk, NC. This region is characterized by complex bathymetry in which a series of shore-oblique bars and troughs extend from 4 to 14 m of water depth [see McNinch, 2004; Miselis, 2007; Brodie and McNinch, *companion paper*; also Figure 8, later in this manuscript). A swath bathymetry survey of the area is used to assess the accuracy of bathymetry inversion due to the location's complex nearshore bathymetry [McNinch, 2004] which cannot be adequately mapped using single-beam profile surveys. One reason for assessing the error of the bathymetry inversion at such a complex site is to determine how much error using only the cross-shore component of wave celerity introduces to our depth calculations. Ideally, the swath and CLARIS survey would be conducted simultaneously to obtain the best error estimates. The two systems, however, require drastically different weather conditions for ideal operations: the swath survey requires calm, low wave conditions, whereas CLARIS is optimal in > 2 m waves with strong onshore winds to ensure wave coverage out to 1 km offshore. Due to the difficulty associated with forecasting a calm weather window long enough for a swath survey (in this case 2-days) that immediately precedes rough, stormy conditions, we are forced to utilize the best weather combination available. Therefore, a CLARIS bathymetry inversion from the morning of April 16 ($H_s = 2.8$ m, $T = 10.7$ s, $\theta_{\text{shoreline}} = 5$ degrees (72 degrees true north)) is compared to a swath survey from April 08 - 09, leaving one week

of separation between the two surveys. Though we also conducted a CLARIS survey on the night of April 15 (during building conditions), this survey is not used, as the wave field was a high-angle ($\theta_{\text{shoreline}} = 24$ degrees (44 degrees true north)), short-period ($T = 6.2$ s), wind-wave, and thus not ideal for the inversion exercises. Although a week separation exists between the swath bathymetry survey and the CLARIS survey, wave heights did not exceed 1.5 m in the week between the two surveys, and thus any real change in bathymetry between the two surveys is believed to be minimal and confined to the very inner-surf zone.

The two data sets are interpolated to coincident 5-m grids, and the water depth predicted by the bathymetry inversion is compared to the water depth measured by the swath survey at each grid node. This comparison produces a total of 176,259 analysis points that range in depth from 1 to 15 m (Figure 6) and cover 4.41 km². Total RMS error is 0.72 m with a mean absolute error of 0.54 m and a standard deviation of 0.12 m. Mean percent error and RMS percent error are also calculated for the total data set and found to be 8.3% and 11.6% respectively. Maximum errors range from -2.4 m to 3.8 m, with negative numbers indicating too deep of a prediction and positive indicating too shallow of a prediction. Total RMS percent error and absolute mean percent error, compare well with those of Holland [2001] but are significantly smaller than those of Stockdon and Holman [2000] (RMS error = 34%). Stockdon and Holman's analysis does not include any compensation for amplitude dispersion, and as such, their RMS error estimate is improved (29%) during low wave conditions ($H \leq 1$ m). Our comparably lower error estimates, even during highly non-linear storm wave conditions, confirm

Holland's [2001] finding that the use of the modified cnoidal wave equation can significantly improve the performance of bathymetry inversions.

RMS error and RMS percent error are also calculated for each wave region: intermediate waves, shallow-water waves, and breaking waves. Similar to other bathymetry inversion studies, our analyses show increased accuracy with depth (where the linear dispersion equation is more applicable). RMS percent error is smallest in the intermediate water depths at 7.8%, followed by the shallow water region at 10.3%, and the surf-zone water depths at 15.4%. RMS absolute error is opposite, with the surf-zone region having a RMS error of 0.59 m, the shallow water region at 0.63 m and the intermediate region at 0.8 m. As depicted in Figure 6, in the shoaling region between ~7 m and the edge of the surf zone, estimates are consistently deeper than observed. Wave data from the cross-shore array at the Duck FRF pier during the survey show shoaling did occur in this region during the survey, with wave height increasing from 2.8 m in 8 m of water depth to 3.1 m in 6 m water depth, suggesting that amplitude dispersion needs to be compensated for in this region as well as in the breaking region. Unfortunately, as of yet no remotely sensed techniques have been developed to provide spatial coverage of wave heights across and along the surf zone during storms. While the input of a constant alongshore wave height at a few points cross-shore (e.g. from the rare cross-shore wave array) may be helpful on alongshore-uniform shorefaces, it will not adequately describe the wave field above complex features [e.g. Munk and Traylor, 1947] such as those found in this study site.

The high errors within the breaking region (RMS percent error = 15.4%) are most likely due to (1) the non-linear properties of breaking waves; and (2) spatial interpolation

schemes forced to interpolate down to the too-deep estimates at the edge of the shallow-water wave region. Error assessment between the shoreline and depths less than 2 m can not be assessed in this study due to inaccessibility of the region with the swath system. Error is assumed very high in this region due to (1) the extreme non-linear relationship between water depth and bore (as opposed to wave) celerity in the inner surf zone [Stive, 1984; Svendsen et al., 2003; Bonneton et al., 2004]; and (2) the large importance of infragravity contributions to water depth (their amplitudes are often a significant proportion of the water depth) in this region [Guza and Thornton, 1982; Wright et al., 1982; Guza and Thornton, 1985]. To help improve accuracy between the shoreline and 2-m water depth, we are investigating how to derive helpful parameters such as bore celerity, wave height, and water level from simultaneously collected laser data of the inner surf zone.

Preliminary results suggest that time series of offshore-directed laser scans of the swash and inner surf-zone (fixed, narrow swaths across the surf-zone) collected during the 6-minute radar stops provide tremendous amounts of data on swash and bore heights. For example, Figure 7A shows ~1.5 s of instantaneous water level measurements ($dt = 5$ Hz), in which incoming bores and down-rushing swash are visible. These data are then averaged through time to reconstruct the inner-surf zone setup profile (Figure 7B), or analyzed for wave spectra to obtain infragravity heights (Figure 7C), among other physical processes, including wave-runup or even breaking wave type from the shape of incoming bores. Error associated with this methodology, including (1) that induced by spectral analysis over relatively short time-series to resolve infragravity motions, and (2) the potential for shadowing of the troughs in the far range, still needs to be quantified and

compared against more common methodologies, such as video-imaging or pressure sensors.

Spatial patterns of bathymetry-inversion error are also assessed (Figure 8). Visually, the swath bathymetry (Figure 8A) and the CLARIS bathymetry inversion (Figure 8B) compare well, with both showing the expression of three large shore-oblique troughs cutting across the nearshore. High errors are seen in the region over the shore-parallel bar, the region most likely to have changed during the one week lapse time. The swath survey appears to define the shore-oblique bars slightly more clearly. This is evident in the spatial percent error map (Figure 8C), where a spatially coherent pattern of “too-deep” errors is apparent: the highest errors are located on the inshore portions of the shore-oblique bar crests immediately adjacent to the shore-oblique troughs on the down-drift side. This could be due to three factors: (1) wave height, and thus amplitude dispersion, is significantly amplified in these locations from wave-crest convergence as the waves refract over the bathymetry; (2) our assumption of shore-parallel waves is violated due to wave refraction patterns, and thus cross-shore wave number is greater than total wave number; or (3) an on-shore current is artificially increasing wave celerity in these regions. Future implementation of a full 2D cross-spectrum analysis [e.g. Plant et al., 2008] will eliminate our current assumption of shore-parallel waves and help to reduce some of the error associated with refraction over complex bathymetry. Overall, 3.2 km² of our area has an error of less than 10%, which represents 72% of the total region.

4.3 Morphology Metrics

Morphology metrics extracted from the time-averaged radar data provide important information about the surf-zone, especially the inner surf-zone, a region where bathymetric data from the bathymetry inversion is less robust. Figure 9A shows an example of a time-averaged radar morphology mosaic with identified morphological features. The morphology mosaic is from the same location in Kitty Hawk, NC where the bathymetry inversion error is assessed. Using the peak-classification scheme described in the methodology section, the morphology mosaic is interpreted in Figure 9B, with regions of wave breaking shown in white, and regions of less wave breaking shown in blue. The cross-shore location of peak dissipation over the outer shore-parallel bar varied significantly alongshore, and is adequately located by the peak-picking technique. Since the location of wave breaking over the bar can vary significantly with changes in water level (tide) or wave height, rarely does the crest of the sandbar align directly with the peak in wave dissipation above it, [Lippmann and Holman, 1989; Ruessink et al., 2003]. Despite the potential for environmental conditions affecting dissipation patterns above the bar, the position of the crest of the outer bar derived from the swath bathymetry survey from a week prior (black dot-dash line, Figure 9A) compares well with the peak in dissipation over the outer bar identified by the peak-picking technique. Notable discrepancies occur at around 5000 m alongshore, and between ~5500 and 6500 m alongshore, and may be due to a variety of factors including true movement, water level effects, or confused peak identification due to complex bathymetry. It is important to note that the highly irregular shape of this outer shore-parallel bar is most likely due to its dissection by the shore-oblique bar and trough features shown in Figure 8A and B. Thus, the peak-picking technique appears to be robust despite the highly three-dimensional nature of this study site.

The inner surf-zone is characterized by an inner bar that is around 75 m offshore between 3000 and 4500 m alongshore, moves ~25 m closer to the shoreline between ~4500 and 5500 m alongshore, and eventually appears to merge with the beach between ~5300 and 7300 m alongshore (narrow and thick black lines in Figure 9A). Since the swath survey did not extend within 2-m of water depth up to the beach, comparison with actual inner surf-zone morphology is impossible; however, the objective peak-picking technique confirms our visual interpretation of both the image and field-based observations of wave breaking patterns during the survey. The offshore edge of the inner bar is mapped using the steepest slope technique described previously. The technique seems fairly insensitive to dissipation cause by any shore-oblique features (e.g. at ~4300 and 5000 m alongshore), most likely because the extended cross-shore dissipation over these features produces low slopes, and thus a position closer to the peak of the inner bar is identified.

Figure 9C shows two example morphology metrics that are extracted from this data set: (1) number of offshore bars (blue stars) and (2) width of the inner surf-zone (red line), defined here as the distance between the objectively identified offshore edge of the dissipation over the inner shore-parallel bar and the radar-observed waterline. Recent research suggests that the configuration of the surf-zone, notably the number of offshore shore-parallel bars, may have significant impacts on the type and severity of erosion occurring at the beach [Lippmann et al., 2004; Shand et al., 2004]. In addition, the inner surf-zone is one of the most crucial areas for modelers to correctly parameterize in order to predict sediment transport at the shoreline, as its morphology affects the amount of energy and momentum that reach the shoreline and is ultimately available for sediment transport. For example, shorelines that have wider surf-zones, and therefore more wave-dissipation and onshore directed radiation stress, may experience higher wave-setup than areas with narrower surf-zones [Longuet-Higgins and Stewart, 1964]. In addition, the slope of the sub-aqueous

foreshore and inner surf-zone may have important implications for the type of wave-breaking occurring at the shoreline (e.g. spilling vs. plunging breakers), and therefore the sediment transport response [Beach and Sternberg, 1996; Voulgaris and Collins, 2000]. While not explicitly measuring the physical processes at work (e.g. dissipation, radiation stress, or breaking wave shape), these morphology metrics may be simple methods for parameterizing otherwise complicated physical processes, and have potential for integration into predictive models.

The position of the radar-observed waterline can also be intersected with lidar-measured topography, providing an accurate elevation of the waterline. This measurement thus provides the elevation associated with the most shoreward swash excursion during the time of observation at locations spaced 3-m alongshore. This technique may have potential for quantifying alongshore variations in wave-runup over large distances during storms; however, how this measurement compares with the 2% exceedence elevation used in current maximum runup models [Stockdon et al., 2006] is still being assessed. Potential sources of error associated with this technique include: the short sampling time compared to longer infragravity fluctuations, and the low spatial resolution of radar (when compared to video, for example) which can add error to the location of the swash front.

4.4 Seamless Topography and Bathymetry during Storms

Figure 10 shows an example of merged lidar topography data of the beach with radar-derived bathymetry inversion data of the surf-zone and nearshore. Since neither the lidar data nor bathymetry data are anisotropic like traditional survey data [e.g. Bernstein et al., 2003], the two data sets are merged using IVS Fledermaus 7.1 and gridded to a 5-m grid using a weighted moving average of 5-m as opposed to more complicated gridding

algorithms techniques [e.g. Mitas and Mitasova, 1999; Mitasova et al., 2005]. Bathymetry data is clipped at 1-m of water depth, and lidar data is given preference over bathymetry inversion data anywhere that overlap occurs (occasionally, the lidar may record elevations down to 1-m of water depth during swash run-down). The cross-shore profile shown in Figure 10B illustrates the seamless topography from dune to 15-m of water depth. The inner and outer shore-parallel bars, as well as a portion of a shore-oblique feature, are clearly visible. Future work will aim to improve the high error between the sub-aqueous foreshore and inner-bar, visible as a pronounced “kink” in the profile at around 50-m offshore. Specifically, lidar-observed bore height, speed, and water level will be explored to improve the accuracy of the bathymetry inversion in this region. In addition, dissipation information recorded by the radar may also be used in conjunction with model-predicted dissipation proxies, such as the energy of the surface roller [Aarninkhof and Ruessink, 2004], to solve for water depth, similar to the Beach Wizard approach [Aarninkhof et al., 2005; van Dongeren et al., 2008].

Seamless elevation data of the beach and nearshore during storms are invaluable for ground-truthing models, measuring morphology evolution, calculating beach and nearshore sediment volumes, and quantitatively analyzing spatial and temporal patterns of beach erosion during storms. Furthermore, CLARIS enables simultaneous analysis of the coastal system as a whole, from the dune, across the beach, through the swash and surf-zones, and into the nearshore. Though the accuracy may not be as high as more traditional surveying techniques, the ability to rapidly acquire during extreme conditions is un-paralleled. For example, Freeman and others [Freeman et al., 2004] present seamless topography and bathymetry data of a 0.5 km stretch of coastline near Cape

Hatteras, that took 5 days and required 4-different surveying methodologies (walking backpack-mounted RTK-GPS, ATV-mounted RTK-GPS, jetski-mounted echo-sounder, and a vessel-mounted interferometric swath system) to complete. In contrast, CLARIS requires only two people and one vehicle, and can easily map a 0.5 km stretch of coastline and bathymetry in under an hour.

5.0 CONCLUSIONS

We presented Coastal Lidar and Radar Imaging System, CLARIS: a mobile, remote sensing system for mapping seamless nearshore bathymetry and beach topography, as well as surf- and swash-zone morphology during storms. CLARIS can survey 10-km of coastline in 2 hours and provide bathymetry from 2-m water depth to 1.2 km offshore to within 11% accuracy, as well as topography of the beach and dune to within 10 cm. The bathymetry-inversion technique used in this study presents two new contributions to the field: (1) information from multiple locations alongshore were mosaicked together to provide roughly 10 km² of bathymetry data during large waves ($H_{sig} \geq 3$ m); and (2) the use of a modified cnoidal wave equation (eqn 6a) solved iteratively with a wave-height depth dependence (eqn 4b) for the breaking-wave region, as suggested by Holland [2001], demonstrated skill. Surf-zone morphology metrics derived from the time-averaged radar data were objectively extracted and used to characterize the inner surf-zone where bathymetry estimates have high error. Terrestrial lidar provided a fast, accurate, and spatially dense technique for mapping three-dimensional beach and dune topography. Operational limits to CLARIS include the need for: (1) beach conditions to be drivable, (2) precipitation to be no more than a light rain,

and (3) the nearshore wave-field must be sufficiently large to interact with seafloor and roughened at the surface by strong winds (i.e. storm conditions are preferable).

6.0 ACKNOWLEDGEMENTS

The authors wish to acknowledge the US Geological Society (G09PG00195) and the US Army Corps of Engineers IRIP 653HC8 for their support of this research. We would also like to thank the entire crew at the USACE Field Research Facility for their technical and field support, especially M. Forte, J. Pipes, and H. Wadman.

REFERENCES

- Aagaard, T., and J. Holm (1989), Digitization of Wave Run-up Using Video Records, *J. Coast. Res.*, 5(3), 547-551.
- Aarninkhof, S. G. J., and B. G. Ruessink (2004), Video observations and model predictions of depth-induced wave dissipation, *IEEE Trans. Geosci. Remote Sens.*, 42(11), 2612-2622.
- Aarninkhof, S. G. J., B. G. Ruessink, and J. A. Roelvink (2005), Nearshore subtidal bathymetry from time-exposure video images, *J. Geophys. Res.*, 110(C6).
- Alexander, P. S., and R. A. Holman (2004), Quantification of nearshore morphology based on video imaging, *Mar. Geol.*, 208(1), 101-111.
- Aubrey, D. G. (1979), Seasonal patterns of onshore/offshore sediment movement, *J. Geophys. Res.*, 84(C10), 6347-6354, doi:10.1029/JC084iC10p06347.
- Beach, R. A., and R. W. Sternberg (1996), Suspended-sediment transport in the surf zone: response to breaking waves, *Cont. Shelf Res.*, 16(15), 1989-2003, doi: DOI: 10.1016/0278-4343(96)00029-5.
- Bell, P. S. (1999), Shallow water bathymetry derived from an analysis of X-band marine radar images of waves, *Coast. Eng.*, 37(3-4), 513-527.
- Bernstein, D. J., C. W. Freeman, J. Park, M. F. Forte, P. T. Gayes, and H. Mitasova (2003), Spatial Survey Design Analysis for 3D Mapping of Beach and Shoreface Morphology, *Proc. Int. Conference on Coastal Sediments 2003*, .
- Birkemeier, W. (1984), Timescales of Nearshore Profile Change, *Proc. of the 19th Coast. Eng. Conference*, ASCE, 1507.
- Birkemeier, W. A., and C. Mason (1984), The CRAB: A unique nearshore surveying vehicle, *J. Surv. Eng.*, 110(1), 1-7.
- Bonneton, P., V. Marieu, H. Dupuis, N. Sénéchal, and B. Castelle (2004), Wave transformation and energy dissipation in the surf zone: Comparison between a non-linear model and field data, *J. Coast. Res.*, SI 39.
- Dugan, J. P., W. D. Morris, K. C. Vierra, C. C. Piotrowski, G. J. Farruggia, and D. C. Champion (2001), Jetski-based nearshore bathymetric and current survey system, *J. Coast. Res.*, 17(4), 900-908.

- Freeman, C. W., D. J. Bernstein, and H. Mitasova (2004), Rapid Response 3D Survey Techniques for Seamless Topo/Bathy Modeling: 2003 Hatteras Breach, North Carolina, *Shore Beach*, 72(2), 3.
- Guza, R. T., and E. B. Thornton (1982), Swash oscillations on a natural beach, *J. Geophys. Res.*, 87(C1), 483-492, doi: 10.1029/JC087iC01p00483.
- Guza, R. T., and E. B. Thornton (1985), Observations of surf beat, *J. Geophys. Res.*, 90(C2), 3161-3172, doi:10.1029/JC090iC02p03161.
- Haller, M. C., and D. R. Lyzenga (2003), Comparison of radar and video observations of shallow water breaking waves, *IEEE Trans. Geosci. Remote Sens.*, 41(4), 832-844.
- Hanson, J. L., H. C. Friebel, and K. K. Hathaway (2009), Coastal wave energy dissipation: observations and STWAVE-FP performance, *11-th International Workshop on Wave Hindcasting and Forecasting*, Halifax, NS, 18-23 October.
- Holland, K. T. (2001), Application of the linear dispersion relation with respect to depth inversion and remotely sensed imagery, *IEEE Trans. Geosci. Remote Sens.*, 39(9), 2060-1072, doi: 10.1109/36.951097.
- Holland, K. T., and R. A. Holman (1999) Wavenumber-frequency structure of infragravity swash motions, *J. Geophys. Res.*, 104(C6), doi:10.1029/1999JC900075.
- Holland, K. T., R. A. Holman, T. C. Lippmann, J. Stanley, and N. Plant (1997), Practical use of video imagery in nearshore oceanographic fieldstudies, *IEEE J. Oceanic Eng.*, 22(1), 81-92.
- Holland, K. T., B. Raubenheimer, R. T. Guza, and R. A. Holman (1995), Runup kinematics on a natural beach, *J. Geophys. Res.*, 100(C3), 4985-4993.
- Holland, K. T. (1998), Beach cusp formation and spacings at Duck, USA, *Cont. Shelf Res.*, 18(10), 1081-1098.
- Holman, R. A., A. H. Sallenger, T. C. Lippmann, and J. W. Haines (1993), The application of video image processing to the study of nearshore processes, *Oceanography*, 6(3), 78-85.
- Holman, R. A., G. Symonds, E. B. Thornton, and R. Ranasinghe (2006), Rip spacing and persistence on an embayed beach, *J. Geophys. Res.*, 111(C1), doi:10.1029/2005JC002965.
- Irish, J. L., W. J. Lillycrop, and L. E. Parson (1996), Accuracy of sand volumes as a function of survey density, *Proc. on the 25th Int. Conf. on Coastal Engineering*, September 26, Orlando, vol. 111, pp.3736 - 3749.

Irish, J., J. McClung, and W. Lillycrop (2000), Airborne lidar bathymetry: the SHOALS system, *PIANC Bulletin*, 103, 43-53.

Irish, J. L., and T. E. White (1998), Coastal engineering applications of high-resolution lidar bathymetry, *Coast. Eng.*, 35(1-2), 47-71.

Lillycrop, W. J., L. E. Parson, and J. L. Irish (1996), Development and operation of the SHOALS airborne lidar hydrographic survey system, *SPIE Selected Papers, Laser Remote Sensing of Natural Waters: From Theory to Practice*, edited by Victor I. Feigles and Yuriji. Kopilevich, St. Petersburg, Russia, vol. 2694, pp. 26-37

Lippmann, T. C., and R. A. Holman (1989), Quantification of sand bar morphology: A video technique based on wave dissipation, *J. Geophys. Res.*, 94(C1), 995-1011.

Lippmann, T. C., and R. A. Holman (1990), The spatial and temporal variability of sand bar morphology, *J. Geophys. Res.*, 95(C7), 11575-11590.

Lippmann, T. C., S. Kannan, and J. List (2004), The Relationship Of Nearshore Sandbar Configuration to Shoreline Change, *Ocean Sci. Meet. Suppl.*, Abstract OS32F-06, Portland.

Longuet-Higgins, M. S., and R. W. Stewart (1964), Radiation stresses in water waves; a physical discussion, with applications, *Deep Sea Res.*, 11, 529-529-562.

McNinch, J. E. (2007), Bar and Swash Imaging Radar (BASIR): A Mobile X-band Radar Designed for Mapping Nearshore Sand Bars and Swash-Defined Shorelines Over Large Distances, *J. Coast. Res.*, 23(1), 59-74.

McNinch, J. E. (2004), Geologic control in the nearshore: shore-oblique sandbars and shoreline erosional hotspots, Mid-Atlantic Bight, USA, *Mar. Geol.*, 211(1-2), 121-141.

Miselis, J. L. (2007), Nearshore morphology and lithology: links to framework geology and shoreline change, Ph.D. Dissertation, School of Marine Science, William and Mary, Williamsburg, VA.

Mitas, L., and H. Mitasova (1999), Spatial interpolation, *Geographical Information Systems: Principles, Techniques, Management and Applications*, Wiley, 481.

Mitasova, H., L. Mitas, and R. S. Harmon (2005), Simultaneous spline approximation and topographic analysis for lidar elevation data in open-source GIS, *IEEE Geosci. Remote Sens. Lett.*, 2(4), 375-379.

Mitasova, H., E. Hardin, M. F. Overton, and M. O. Kurum (2010), Geospatial analysis of vulnerable beach-foredune systems from decadal time series of lidar data, *Journal of Coastal Conservation*, , 1-12, doi: 10.1007/s11852-010-0088-1.

- Munk, W. H., and M. A. Traylor (1947), Refraction of ocean waves: a process linking underwater topography to beach erosion, *J. Geol.*, 55(1), 1-26.
- Pielke Jr, R. A., J. Gratz, C. W. Landsea, D. Collins, M. A. Saunders, and R. Musulin (2008), Normalized Hurricane Damage in the United States:1900-2005, *Nat. Hazards Rev.*, 9(1), 29-29-42.
- Pietro, L. S., M. A. O'Neal, and J. A. Puleo (2008), Developing terrestrial-LIDAR-based digital elevation models for monitoring beach nourishment performance, *J. Coast. Res.*, 24(6), 1555-1564.
- Plant, N. G., K. T. Holland, and M. C. Haller (2008), Ocean Wavenumber Estimation from Wave-Resolving Time Series Imagery, *IEEE Trans. Geosci. Remote Sens.*, 46(9), 2644-2659.
- Plant, N. G., K. T. Holland, and J. A. Puleo (2002), Analysis of the scale of errors in nearshore bathymetric data, *Mar. Geol.*, 191(1-2), 71-86.
- Ranasinghe, R., G. Symonds, K. Black, and R. A. Holman (2004), Morphodynamics of intermediate beaches: a video imaging and numerical modelling study, *Coast. Eng.*, 51(7), 629-655.
- Reniers, A. J. H. M., J. A. Roelvink, and E. B. Thornton (2004), Morphodynamic modeling of an embayed beach under wave group forcing, *J. Geophys. Res.*, 109(C1), doi:10.1029/2003JC002083.
- Ruessink, B. G., P. S. Bell, I. M. J. van Enckevort, and S. G. J. Aarninkhof (2002), Nearshore bar crest location quantified from time-averaged X-band radar images, *Coast. Eng.*, 45(1), 19-32.
- Ruessink, B. G., I. M. J. van Enckevort, K. S. Kingston, and M. A. Davidson (2000), Analysis of observed two- and three-dimensional nearshore bar behaviour, *Mar. Geol.*, 169(1), 161-183.
- Ruggiero, P., and R. A. Holman (2004), Wave run-up on a high-energy dissipative beach, *J. Geophys. Res.*, 109(C6), 1-12, doi: 10.1029/2003JC002160.
- Sallenger Jr, A. H., P. Howd, J. Brock, W. B. Krabill, R. N. Swift, S. Manizade, and M. Duffy (1999), Scaling winter storm impacts on Assateague Island, MD, VA, *Proc. Int. Conference on Coastal Sediments 1999*, New York, June 21-23, 1999.
- Sallenger Jr, A. H., W. B. Krabill, R. N. Swift, J. Brock, J. List, M. Hansen, R. A. Holman, S. Manizade, J. Sontag, and A. Meredith (2003), Evaluation of Airborne Topographic Lidar* for Quantifying Beach Changes, *J. Coast. Res.*, 19(1), 125-133.

Sallenger Jr, A. H., R. A. Holman, and W. A. Birkemeier (1985), Storm-induced response of a nearshore-bar system, *Mar. Geol.*, 64(3-4), 237-257, doi: DOI: 10.1016/0025-3227(85)90107-0.

Sallenger, A. H., C. W. Wright, K. Guy, and K. Morgan (2004), Assessing storm-induced damage and dune erosion using airborne lidar: Examples from Hurricane Isabel, *Shore Beach*, 72(2), 3-7.

Sallenger, A., H. Stockdon, L. Fauver, M. Hansen, D. Thompson, C. Wright, and J. Lillycrop (2006), Hurricanes 2004: An overview of their characteristics and coastal change, *Estuaries and Coasts*, 29(6), 880-888.

Setter, C., and R. J. Willis (1994), LADS--From development to hydrographic operations, *Proc. US Hydro. Conf*, The Hydrographic Society Spec. Pub. No. 32, pp 134-139.

Shand, R. D., P. A. Hesp, and M. J. Shepherd (2004), Beach cut in relation to net offshore bar migration, *J. Coast. Res.*, .

Stive, M. J. F. (1984), Energy dissipation in waves breaking on gentle slopes, *Coast. Eng.*, 8(2), 99-127, doi: DOI: 10.1016/0378-3839(84)90007-3.

Stockdon, H. F., J. Sallenger A.H., J. H. List, and R. A. Holman (2002), Estimation of Shoreline Position and Change using Airborne Topographic Lidar Data, *J. Coast. Res.*, 18(3), 502-513.

Stockdon, H. F., and R. A. Holman (2000), Estimation of wave phase speed and nearshore bathymetry from video imagery, *J. Geophys. Res.*, 105, doi: 10.1029/1999JC000124.

Stockdon, H. F., R. A. Holman, P. A. Howd, and J. Sallenger Asbury H. (2006), Empirical parameterization of setup, swash, and runup, *Coast. Eng.*, 53(7), 573-588.

Svendsen, I. A., W. Qin, and B. A. Ebersole (2003), Modelling waves and currents at the LSTF and other laboratory facilities, *Coast. Eng.*, 50(1-2), 19-45.

Thornton, E. B., and R. T. Guza (1982), Energy saturation and phase speeds measured on a natural beach, *J. Geophys. Res.*, 87(C12), 9499-9508.

Thornton, E. B., R. T. Humiston, and W. Birkemeier (1996), Bar/trough generation on a natural beach, *J. Geophys. Res.*, 101(C5), 12097-12110.

van Dongeren, A., N. G. Plant, A. Cohen, D. Roelvink, M. C. Haller, and P. Catalán (2008), Beach Wizard: Nearshore bathymetry estimation through assimilation of model computations and remote observations, *Coast. Eng.*, 55(12), 1016-1027.

van Enkevort, I. M. J., and B. G. Ruessink (2003), Video observations of nearshore bar behaviour. Part 1: alongshore uniform variability, *Cont. Shelf Res.*, 23(5), 501-512.

Van Enkevort, I. M. J., B. G. Ruessink, G. Coco, K. Suzuki, I. L. Turner, N. G. Plant, and R. A. Holman (2004), Observations of nearshore crescentic sandbars, *J. Geophys. Res.*, 109(C6), doi:10.1029/2003JC002214.

Voulgaris, G., and M. B. Collins (2000), Sediment resuspension on beaches: response to breaking waves, *Mar. Geol.*, 167(1-2), 167-187, doi: 10.1016/S0025-3227(00)00025-6.

Wright, L. D., R. T. Guza, and A. D. Short (1982), Dynamics of a high-energy dissipative surf zone, *Mar. Geol.*, 45(1-2), 41-62, doi: 10.1016/0025-3227(82)90179-7.

FIGURE CAPTIONS

Figure 1. Comparison of radar and video snapshots of a nearshore wave-field during storm conditions. Panel A shows a single rotation image from the radar with clearly defined wave-forms (horizontal high-intensity, linear features). The location of the Argus tower is noted, and the approximate view-field of camera c1 is illustrated by the white trapezoid. Panel B shows a video snapshot of the same area from 10 minutes prior to the radar. Peak wave parameters recorded by the 8-m array (white star, panel A) at 1000 EST were: $H_s=4.1$ m, $Dir = 88^\circ$, $T_p=13.6$ s.

Figure 2. Evolution of CLARIS. Panels A through C are earlier versions of the system, and panel D shows the current configuration and integration of the radar, lidar, RTK-GPS, and POS-LV (motion) data. The extreme-storm vehicle platform is shown in panel E, and can be safely inundated in up to 1.5 m of water.

Figure 3. Morphology metric extraction. Each radar rotation (panel A) from every radar stop is gridded into an alongshore/cross-shore/time grid (panel B). Morphology metrics are extracted by averaging cross-shore time stacks of radar intensities (panel C) through time, and identifying peaks, valleys, and slope changes in the cross-shore intensity profile (panel D).

Figure 4. Example wavenumber calculation along a sample cross-shore profile. The amplitude of the co-spectrum is shown in panel A, with the coherence estimate shown in panel B. The frequency of peak coherence at each location in the cross-shore profile is

denoted by the black stars, and the resulting wavenumber (solid) and wavelength (dashed) calculation, is plotted in panel C.

Figure 5. Example of point-cloud lidar topography. Panel A shows a wide-angle view of lidar data from Kitty Hawk, NC, and panel B is a zoom-in (black box, panel A) illustrating the detail recorded by the lidar data.

Figure 6: Bathymetry inversion point by point error assessment. The solid black line represents the 1:1 line and the dashed black lines indicate plus or minus 10%. Note the depth bias between ~ 7 and 4 m.

Figure 7. Lidar-observed swash and inner surf-zone wave parameters. In panel A, incoming bores and down-rushing swash are visible in an example 7 lidar “sweeps” during a lidar time-series. Meaning all of the recorded lidar elevations through time (blue dots, panel B) enables calculation of the shoreline setup profile (magenta line, panel B). In addition, wave spectra (H, T) can be calculated at each location (in this case, every 10 cm) along the profile (panel C).

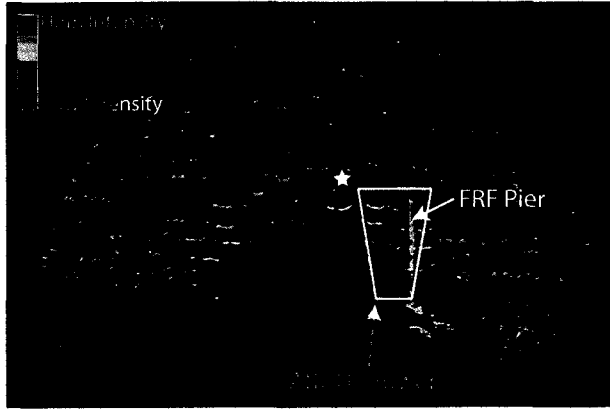
Figure 8: Bathymetry inversion spatial error assessment. Swath bathymetry (panel A) shows more detailed features than the smoother bathymetry inversion (panel B). Percent error assessment (panel C) suggests the highest errors occur over the complex, steep features, as exemplified around 4300 m, 5800 m and 6800 m alongshore.

Figure 9: Morphology mosaic and extracted metrics. In panel A, a radar morphology mosaic is shown with objectively identified morphological features from dissipation peaks, as well as the crest of the outer shore-parallel bar from the swath bathymetry data (dash-dot line). In panel B, the morphology mosaic is interpreted based on the objectively identified features, and shows an inner bar merging with the swash between ~5200 m alongshore and 7300 m alongshore. In panel C, two example morphology metrics, # of offshore bars (blue stars) and inner surf-zone width (red line), are plotted.

Figure 10: Seamless topography and bathymetry. Merged lidar and bathymetry data from Kitty Hawk, NC are shown in panel A, with lidar point-cloud data overlaid. Morphological features such as an inner, outer, and shore-oblique bar are visible in the cross-shore profile (A – A') shown in panel B.

Figure 1

A. Radar Single Rotation Image (25 Sep 2008 0910 EST)



B. Video Snapshot Camera c1 (25 Sep 2008 0900 EST)



Figure 2

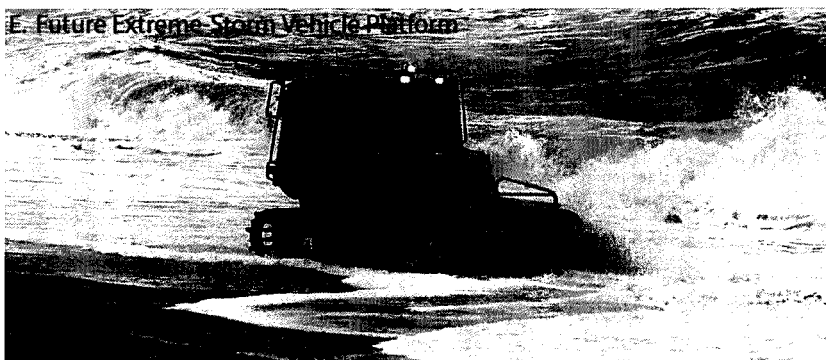
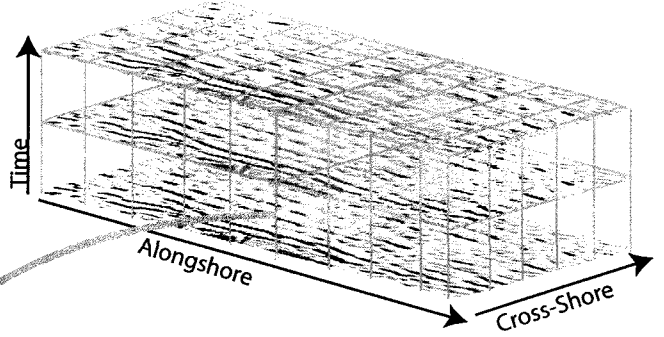
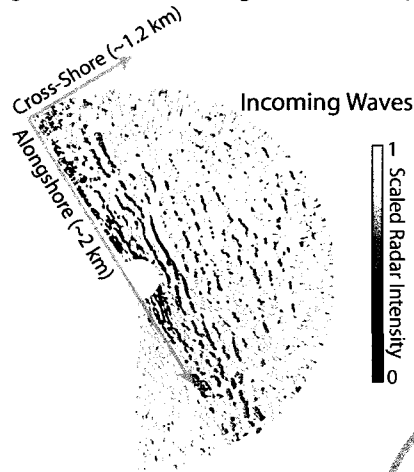


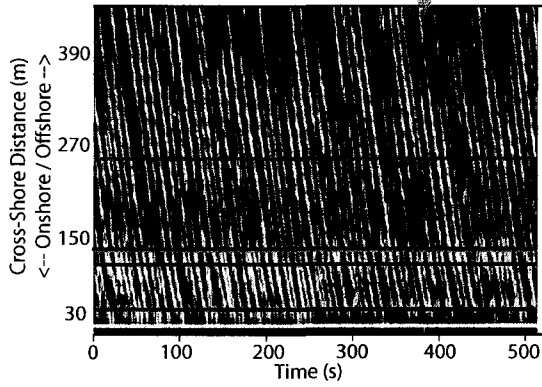
Figure 3

A. Single Rotation Radar Image in Cartesian Space:

B. Radar data gridded in Alongshore/Cross-Shore Space and Time



C. Time Stack of Radar Intensities



D. Time-averaged Radar Intensity Profile

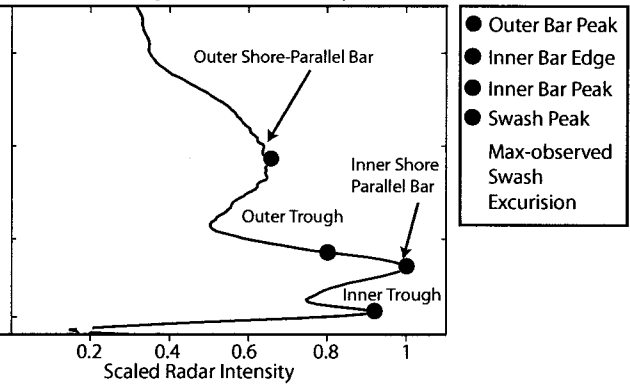


Figure 4

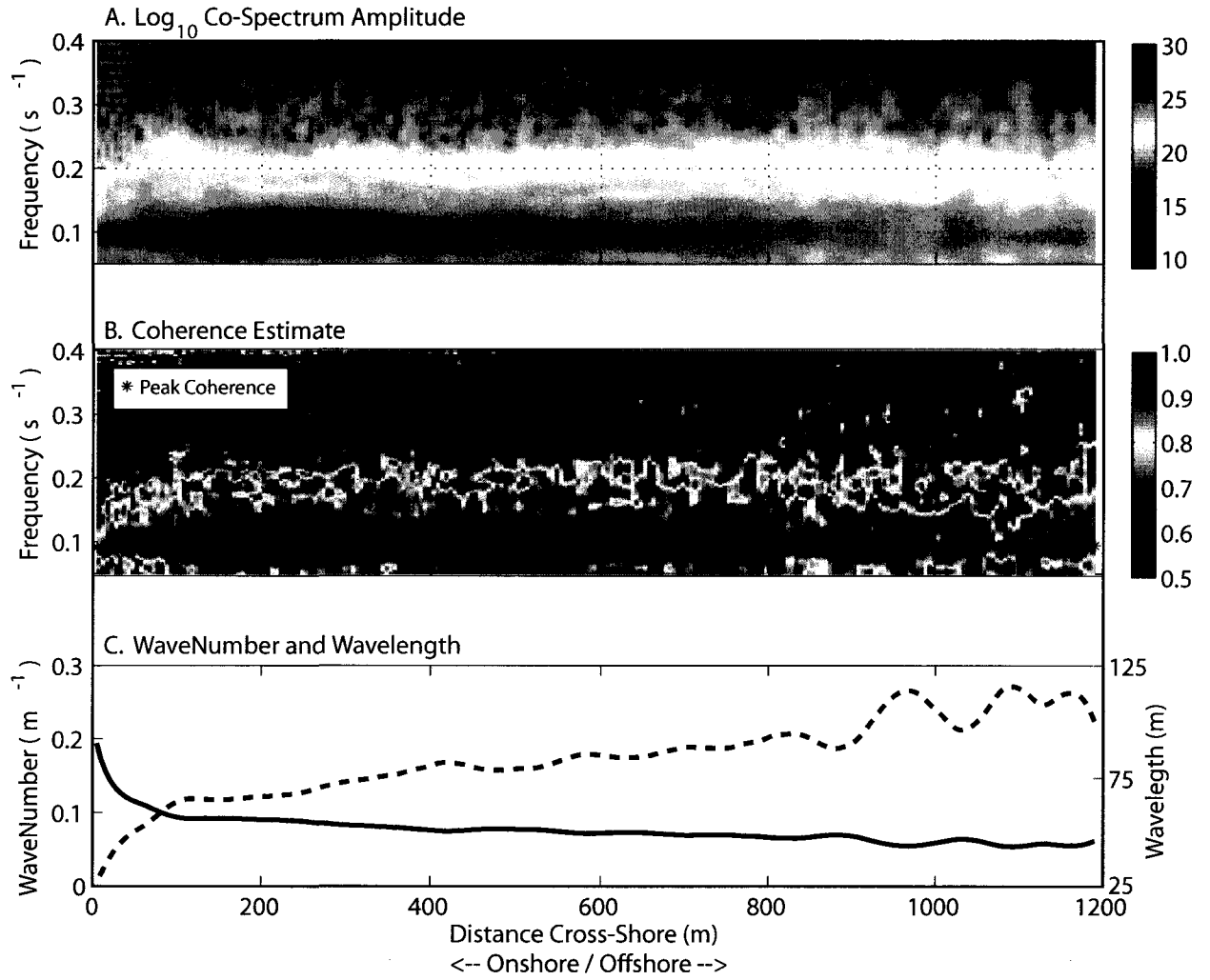


Figure 5

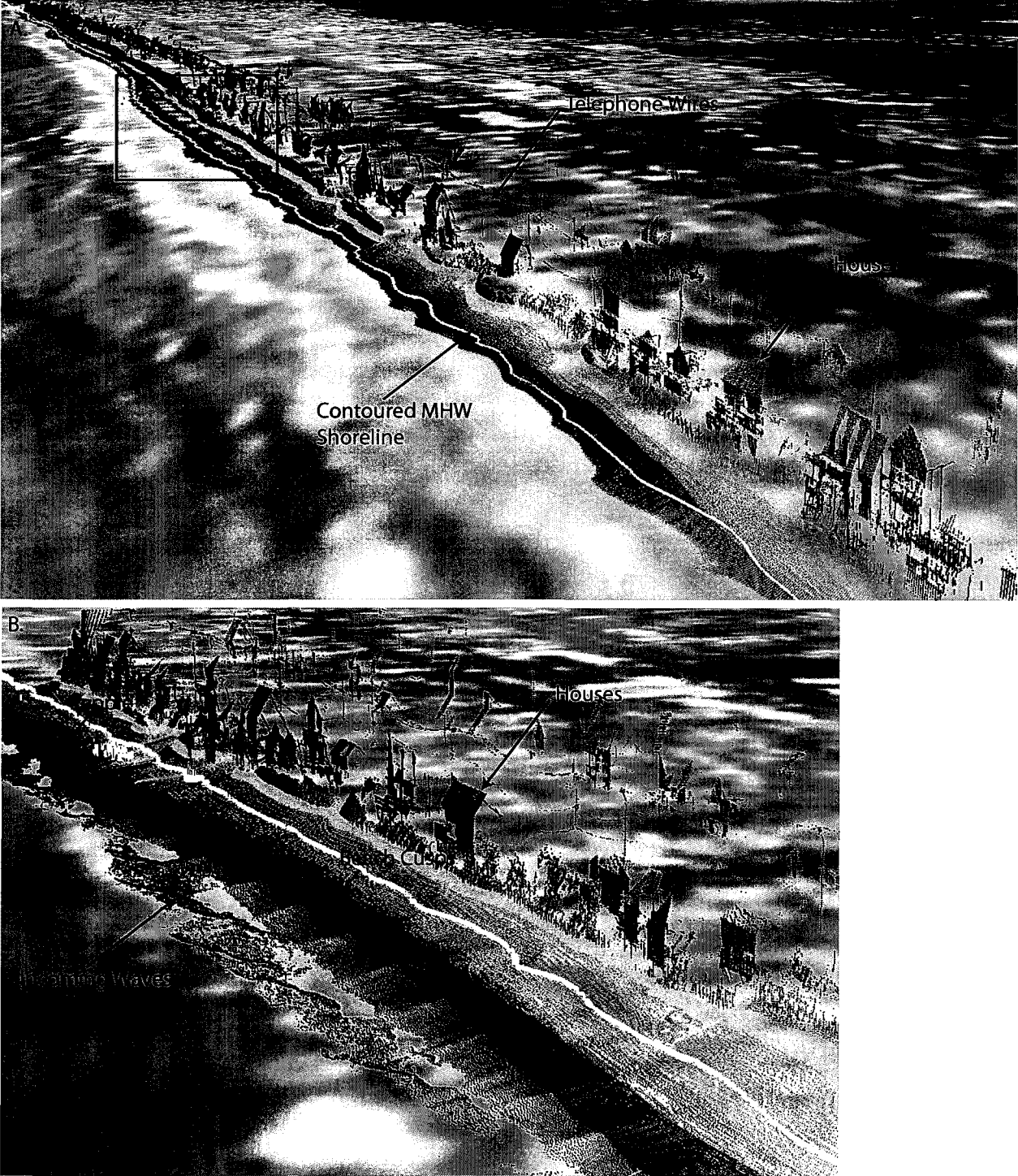


Figure 6

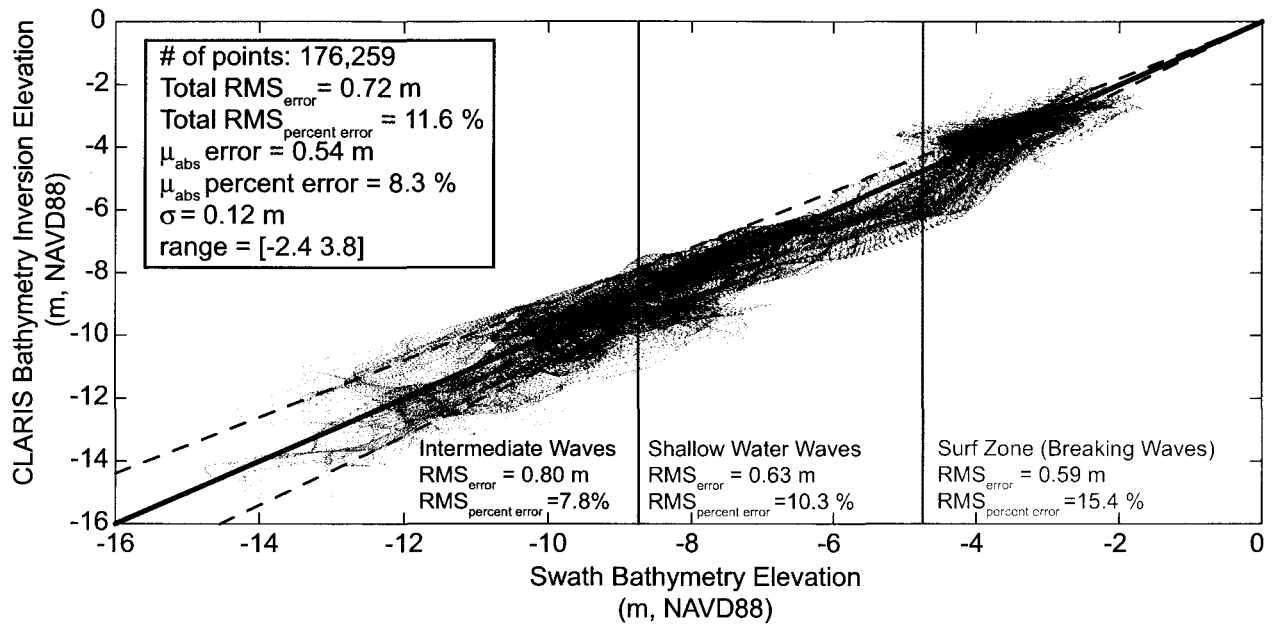


Figure 7

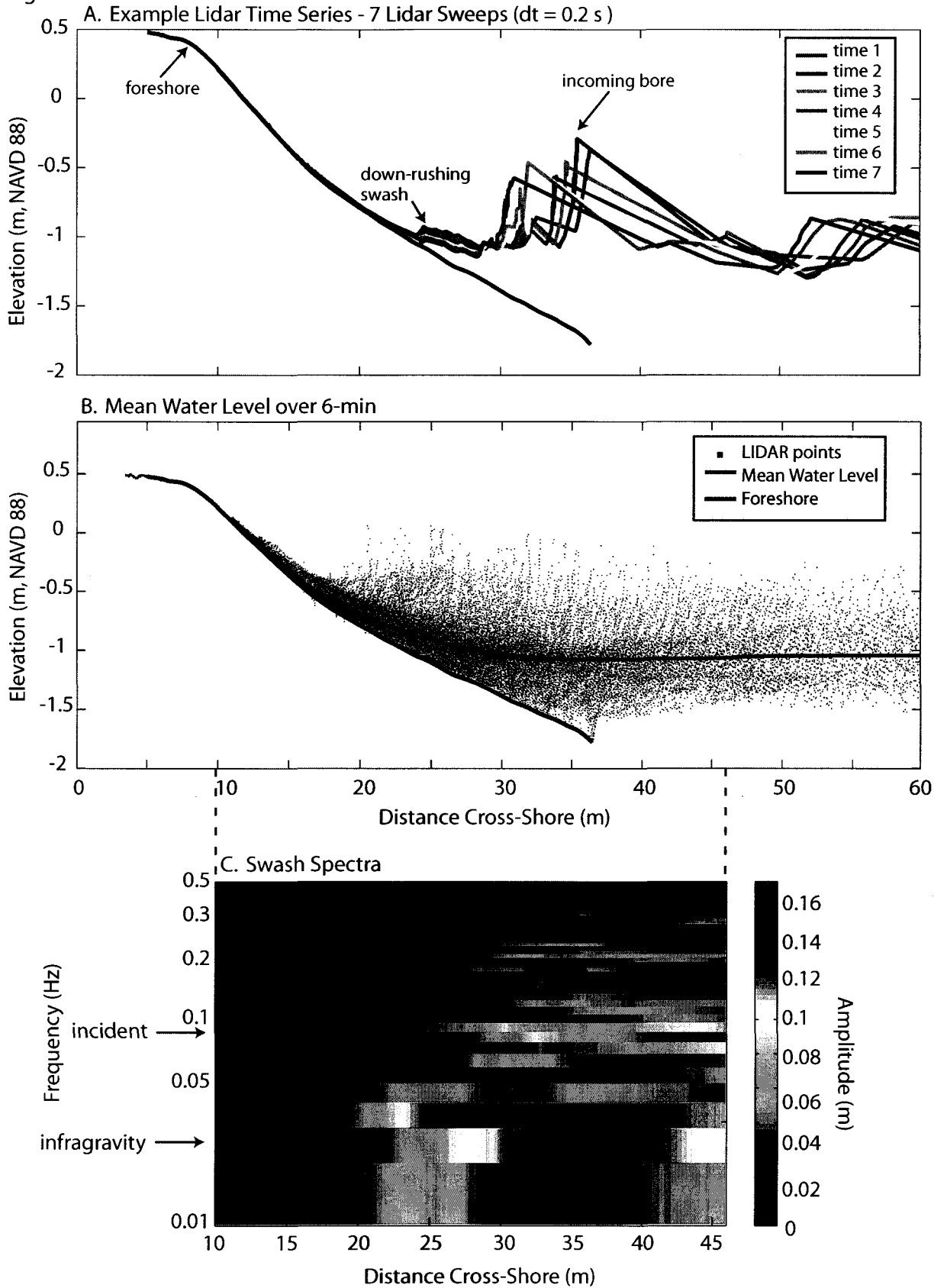


Figure 8

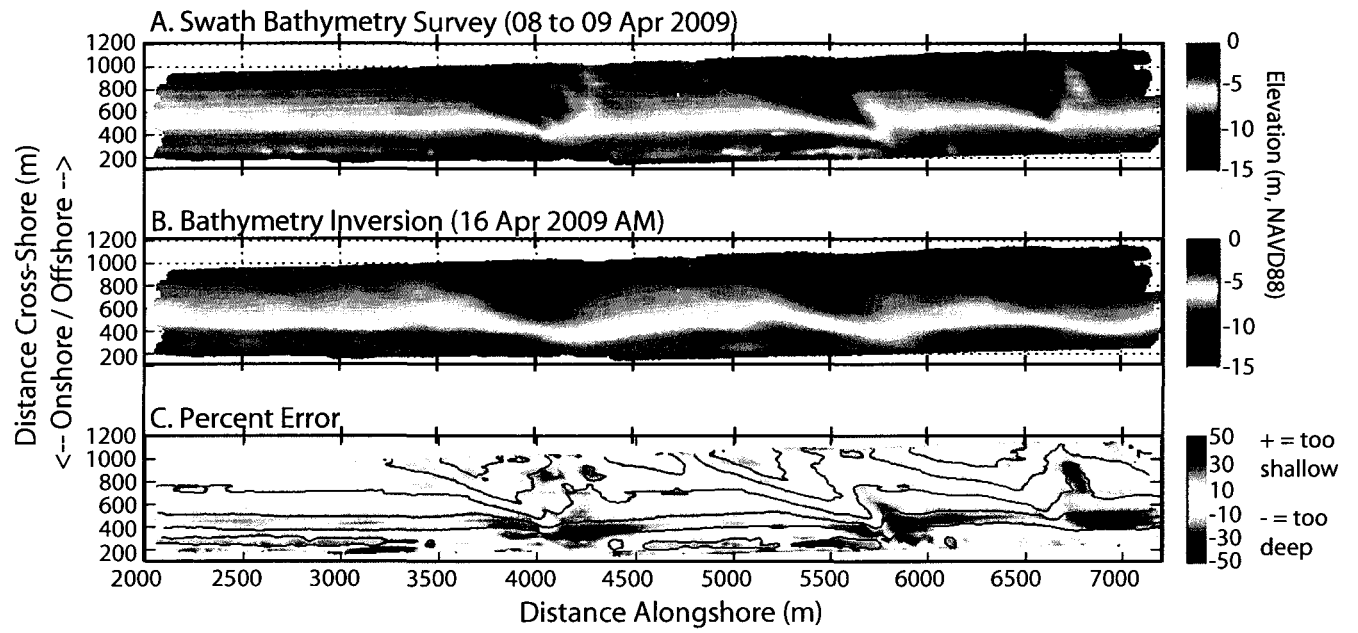


Figure 9

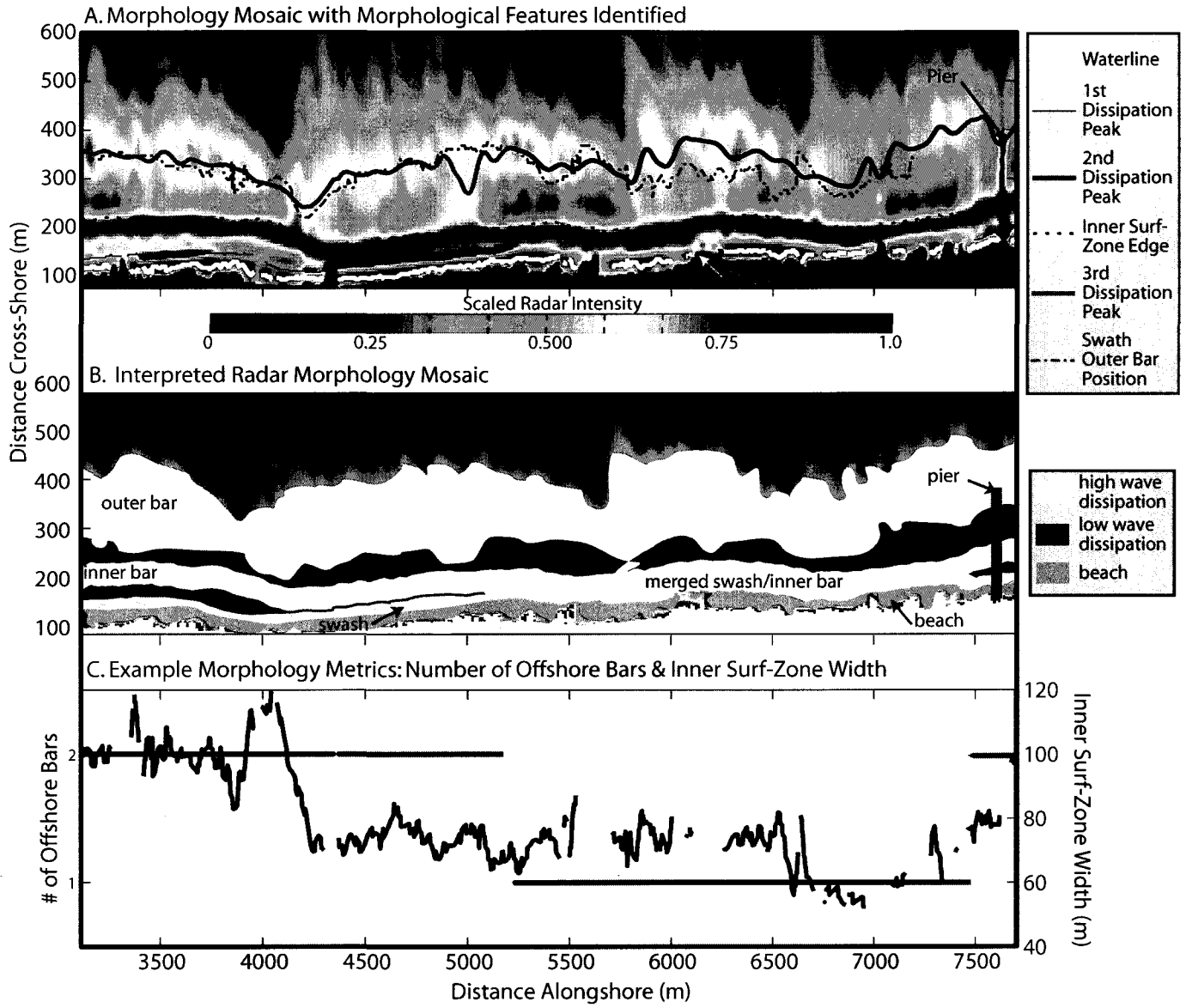
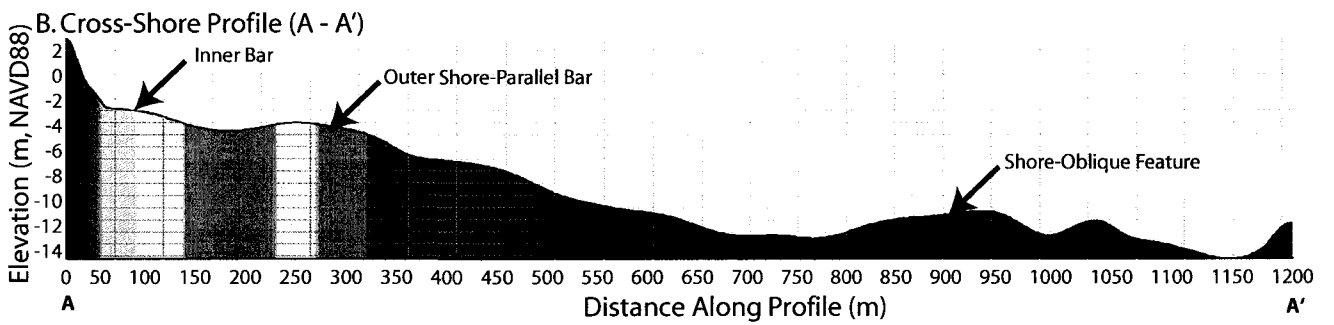
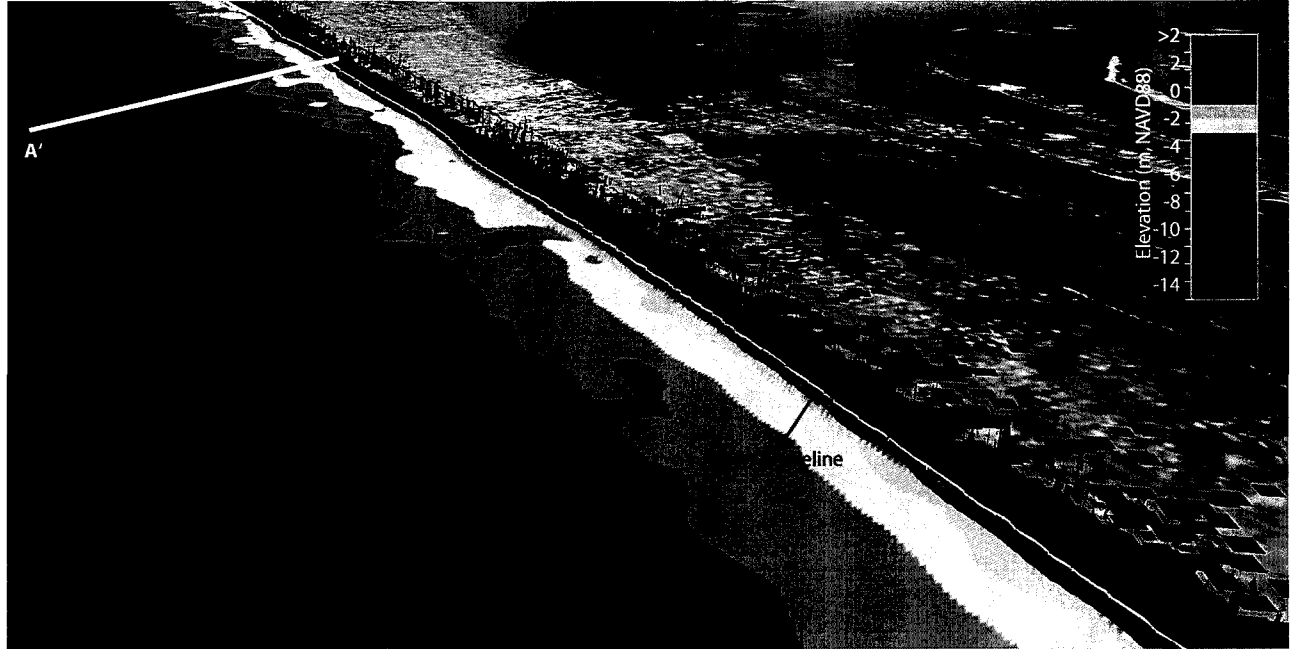


Figure 10
A. Merged Bathymetry and Lidar: Kitty Hawk, NC



CHAPTER 2

Storm morphodynamics at shoreline erosional hotspots:
persistent three-dimensional morphology measured by CLARIS

Manuscript citation: Brodie, KL and McNinch, JE (*Accepted*). Storm morphodynamics at shoreline erosional hotspots: persistent three-dimensional morphology measured by Coastal LiDAR and Radar Imaging System (CLARIS). *Journal of Geophysical Research: Earth Surface*, doi: 2009JF001561.

ABSTRACT

During storms, conventional theory suggests shorelines and surf-zones linearize into two-dimensional forms. Shoreline hotspots interrupt this behavior, introducing anomalous behavior and alongshore variability in storm-induced beach erosion, and challenging our understanding of storm-morphodynamics. The physical processes driving shoreline hotspots are not well understood due, in part, to the difficulty of observing them during high-energy conditions with traditional in-situ surveying methods. This work presents semi-daily ($dt = 12$ hours) observations of shoreline hotspots along 10 km of coastline on North Carolina's Outer Banks during a storm ($H_{sig,8m} > 3$ m) using Coastal Lidar And Radar Imaging System, CLARIS. CLARIS couples X-Band radar with a 3D terrestrial laser scanner, providing observations of beach topography and nearshore bathymetry from radar-derived wave celerity measurements. In addition, the Steady-State Spectral Wave Model, STWAVE, is used to model wave transformation during the storm. We demonstrate that three-dimensional shoreline, shore-parallel bar, and nearshore morphologies persist through the storm, and as a result wave dissipation is also alongshore variable. The shape of the beach and outer shore-parallel bar mirror the nearshore bathymetry, with the curvature of shoreline perturbations an order of magnitude smaller than bathymetry perturbations. We propose that the shoreline is morphologically coupled to nearshore bathymetry by hydrodynamic feedbacks induced by wave transformation over geologically controlled, persistent features. Gradients in wave height, direction, and radiation stress are strongest during shore-parallel swell conditions due to oblique nearshore contours, and may induce convergent and divergent longshore transport or 2D circulation that enhances shoreline morphology and focuses erosion.

1. INTRODUCTION

The morphological evolution of beaches and surf-zones has been the topic of many studies [e.g. Wright and Short, 1984; Lippmann and Holman, 1990], and as such, down-state morphology evolution during calm conditions is well understood and modeled [Ranasinghe et al., 2004]. A lack of observations during storms, when beaches and surf-zones become high- energy dynamic environments, has created a reliance on “pre” and “post” storm data in the analysis of storm-response of the coastal system. A common observation for event-response of the nearshore system is that three-dimensional features, such as crescentic or transverse bars in the surf-zone and cusp features on the shoreline, are smoothed or “reset” into linear forms post-storm [Wright and Short, 1984; Lippmann and Holman, 1990; Ruessink et al., 2000; Van Enckevort et al., 2004]. Despite this storm-driven linearization, there is growing evidence that pre-storm alongshore-variable beach or nearshore morphology may leave certain areas of the coastline more susceptible to erosion, perhaps contributing to the existence of shoreline hotspots [Sallenger Jr, 2000; McNinch, 2004; Schupp et al., 2006; Stockdon et al., 2007; Thornton et al., 2007; Houser et al., 2008]. Here we explore the relationship between shoreline morphology and complex nearshore bathymetry, and the apparent persistence of these features at a shoreline hotspot during a storm event. Specifically, we present daily, spatially extensive (10 km alongshore and 1 km in the cross-shore direction) observations of beach topography and nearshore bathymetry along a shoreline hotspot during a storm and investigate the observed morphological evolution with respect to modeled wave transformation. These data reveal a possible morphologic coupling between shoreline dynamics and storm-resilient, geologically controlled nearshore bathymetry that counters

traditional ideas of storm morphodynamics. Namely, we demonstrate (1) the persistence of three-dimensional morphology during storms; (2) the development of a complex wave-field during low-angle waves; and (3) a spatial coupling between nearshore bathymetry and shoreline morphology that is likely driven by self-organized flow patterns forced by a bathymetric template.

Shoreline hotspots are regions of coastline that experience excessive erosion or accretion during storms, and thus are characterized by anomalously high shoreline change rates (see McNinch, 2004 for a complete description of types of hotspots). While some shoreline hotspots, such as those located near engineering structures [see Kraus et al., 2001], inlets [Dean and Work, 1993; Fenster and Dolan, 1996], or certain bathymetric irregularities such as borrow-pit holes [Bender and Dean, 2004; Benedet and List, 2008] are well understood, hotspots that occur along relatively straight, un-interrupted shorelines [McNinch, 2004; Fenster and Dolan, 1993; Kraus and Galgano, 2001; List et al., 2006], are an example of a type of alongshore-variable storm response that can not yet be predicted by physics-based models. Extensive field work along the Outer Banks of North Carolina and southern Virginia has spatially correlated shoreline hotspots with nearshore shore-oblique sandbars and troughs, nearshore heterogeneous sediment deposits, and underlying paleo-channels [McNinch, 2004; Schupp et al., 2006; Browder and McNinch, 2006; Miselis, 2007], but the morphodynamics explaining the cause of these hotspots are still unknown. In fact, it is still unclear whether the associated irregular bathymetry persists throughout storms, thus altering the storm wave field and influencing surf-zone dynamics, or whether it is smoothed and reforms post-storm [McNinch and Miselis, 2009]. This work is motivated in large part to measure nearshore,

surf-zone, and shoreline morphology at a shoreline hotspot during storms to test whether irregular morphology may persist through storms and if the nearshore and shoreline remain coupled.

Specific objectives of this paper are to: (1) measure the evolution of shoreline morphology and nearshore bathymetry at an erosional hotspot during a storm; and (2) identify the morphodynamic relationship between the morphology and hydrodynamics that drive this evolution. We hypothesize that: (1) three dimensional nearshore bathymetry and shoreline morphology persists during storms, and (2) wave transformation over the irregular bathymetry leads to alongshore gradients in wave height, direction, and dissipation that influence shoreline response. We use remote sensing technologies, specifically the simultaneous collection of terrestrial LiDAR and radar data from CLARIS, Coastal LiDAR And Radar Imaging System [Chapter 1, this dissertation], to investigate the evolution of the entire nearshore system along a shoreline hotspot daily over the course of a storm event. We then use the STeady-state spectral WAVE model Full-Plane version, STWAVE-FP, [Smith et al., 2001; Smith and Sherlock, 2007] to model wave transformation during the observed storm over the nearshore bathymetry of the erosional hotspot. In the following section, we present background on general theories of storm-event nearshore morphodynamics and alongshore-variable beach morphology. We then present details on the field site and the observed storm event, as well as describe the methodologies used in the study, including a brief description of CLARIS methodology and an evaluation of the wave model. Results are divided between CLARIS-derived field observations of morphology and modeled wave transformation. In the discussion, we present an analysis of the observed nearshore, surf-zone, and shoreline

morphology and use the wave-modeling results to propose ideas relating to hydrodynamic gradients driving the observed storm morphodynamics.

2. BACKGROUND

2.1 Surf-Zone Morphodynamics

On intermediate beaches, the morphology of the surf-zone is widely documented to rapidly evolve from three-dimensional bar configurations to two-dimensional shore-parallel forms, often termed “reset” events, when exposed to high energy waves [e.g. Lippmann and Holman, 1990; Ranasinghe et al., 2004; Van Enckevort et al., 2004]. Many field and modeling studies have therefore focused on understanding and predicting the 2-D, wave-driven, cross-shore movement of sediment and sandbars in response to storms [Aubrey, 1979; Birkemeier, 1984; Roelvink and Brøker, 1993; Thornton et al., 1996; Gallagher et al., 1998; Elgar et al., 2001; Plant et al., 2001; Hoefel and Elgar, 2003; van Rijn et al., 2003; Ruessink et al., 2007]. A common conceptual model for the 2-D event response of the nearshore system is that shoreline erosion and offshore movement of the shore-parallel bar during storms is closely followed by post-storm shoreline accretion and onshore shore-parallel bar movement [Aubrey, 1979; Birkemeier, 1984; Lee et al., 1995]. Sub-aerial beach erosion during storms is often attributed to elevated water levels allowing storm waves to flatten steep beach faces [Komar, 1998]. The offshore movement of the shore-parallel bar is driven by cross-shore gradients in suspended and bedload sediment transport caused by intensified undertow at or just shoreward of the bar due to concentrated breaking of large storm waves over the bar [Thornton et al., 1996; Gallagher et al., 1998; Ruessink et al., 2007]. The cause of post-storm accretion and onshore bar migration is attributed to asymmetries in wave orbital

velocity or acceleration beneath non-linear shoaling swell waves during calm conditions [Elgar et al., 2001; Hoefel and Elgar, 2003; Ruessink et al., 2007; Bowen, 1980]. Others have suggested that horizontal flow patterns associated with the return to three-dimensional bar configurations under low energy conditions may drive some of the onshore bar movement un-modeled by purely two-dimensional, cross-shore transport models [Plant et al., 2006].

While the direction of sandbar movement during storms is well understood, the mechanisms driving linearization of the shore-parallel bar (and shoreline) remain speculative, and modeling attempts at these “upstate” transitions are rare (an extensive literature search produced only one example: Smit et al. [2005]). Lippman and Holman [1990] note that transitions to linear forms can occur in less than one day following increases in wave energy associated with storms, and many others have also attributed upstate bar linearizations to high wave energy [Ranasinghe et al. 2004; Van Enckevort et al., 2004; Castelle et al., 2007]. Strong alongshore currents derived from high-angle waves during the building portion of storms may help smooth three-dimensional bar configurations into two-dimensional forms [Sonu, 1973; Komar, 1998; Lafon et al. 2005], often creating deep, continuous troughs between bars and the shoreline [Sénéchal et al., 2009]. In contrast, straightening of crescentic bars under shore-normal waves has also been observed by Van Enckevort et al. [2004] and Castelle [2007], suggesting mechanisms other than alongshore currents may also be important. While the physical processes driving surf-zone linearization may still be unclear, consensus is that sandbar-linearization is expected during high-wave storm conditions.

2.2 Three-Dimensional Shoreline Shapes

The nearshore is inherently a three-dimensional system, in which cross-shore undertow and rip currents, alongshore littoral drift, wave orbital currents, and vertical turbulent mixing all combine to create spatial gradients in sediment transport that shape the beach and the surf zone. Three-dimensional shapes on the beach, presumably built by these complex circulation patterns, have been observed at many different spatial and temporal scales and can range from beach cusps to alongshore sand waves. At the smallest scale, foreshore rhythmic beach cusps with alongshore length scales of 5 to 50 m and cross-shore excursions of 5 to 10 m, can persist from days to months [Holland and Holman, 1996]. At the next largest scale, megacusp/embayment features, thought to be related to rip currents and rhythmic alongshore bars, have alongshore length scales on the order of 100s of meters with cross-shore excursions up to 50 m, and also persist from days to months [Wright and Short, 1984; Lippmann and Holman, 1990; Thornton et al., 2007]. Arrhythmic megacusps with alongshore length scales of 100 to 2000 m and cross-shore excursions of up to 100 m can persist for much longer time scales (days to several years) and are poorly understood [Dolan, 1971]. Finally, alongshore sand waves, with alongshore length scales of 2 to 6 km and cross-shore excursions of up to 200 m, can persist from months to decades and often slowly migrate alongshore [Stive et al., 2002].

With the exception of small-scale beach cusps and rip current related megacusp/embayments, little research has focused on analyzing how the larger-scale three-dimensional features evolve through storms. Their presence and evolution is significant, nevertheless, as it can drastically alter the apparent width of the beach and shape of the shoreline, potentially making certain areas more susceptible to wave setup and erosion during storms. For example, Thornton et al. [2007] showed that along the coast of southern Monterey Bay in California, dune erosion is significantly pronounced behind large rip-

current related shoreline embayments, due to the swash of large storm waves covering the narrow beach associated with the embayment and colliding with the dune base. In addition, they note that these large scale features (order of magnitude ~ 200m) are often straightened during storms through both erosion of the megacusp horns and filling of the embayments (Thornton et al., 2007).

3.0 STUDY AREA

3.1 Field Site

This work is conducted along a ~10 km region of the northern Outer Banks of North Carolina from northern Kill Devil Hills north to Kitty Hawk (Figure 1). The Outer Banks are a long, linear series of wave-dominated [Hayes, 1979], microtidal barrier islands that stretch ~200 km along the Atlantic Ocean and front the Currituck, Albemarle, and Pamlico Sound estuaries. The storm season traditionally occurs during the fall, winter, and early spring and is characterized by frequent extratropical storms, colloquially known as Nor'easters [Lee et al., 1998]. Tropical storms and hurricanes can affect the area during the late summer and early fall. Storms events, defined as waves > 2 m for > 8 hours, are characterized by average maximum wave heights of 3.1 m with a standard deviation of 0.85m (from 1987 to 2008, <http://www.frf.usace.army.mil/storms.shtml>). Lee et al. [1998] have shown that successive storm events can have a large impact on beach and surf-zone morphology and play an important role in meso-scale (year to decade) cross-shore profile evolution on the northern Outer Banks. Analysis of long-term (decadal) shoreline change data and bathymetric surveys along the Outer Banks have identified areas in the nearshore with high bathymetric relief, characterized by shore-oblique sand bars and troughs, that spatially correlate with areas

experiencing anomalously high decadal shoreline-change rates and underlying geologic features such as paleo-channels [McNinch, 2004; Browder and McNinch, 2006].

This specific portion of the northern Outer Banks (Figure 1) is chosen for this study because of its classification as a decadal shoreline erosional hotspot with atypical nearshore bathymetry: a series of shore-oblique bars and troughs extend from ~500 m offshore in 4 m water depth to ~1000 m offshore in 14 m of water depth [McNinch, 2004]. The locations of the shore-oblique bars and troughs are spatially correlated with areas on the shoreline that exhibit high long-term and short-term shoreline change rates [Schupp et al., 2006]. Nearshore sediments are vertically and horizontally heterogeneous [Miselis, 2007], with muddy-gravel deposits found in the trough features of the shore-oblique bar-field. The muddy-gravel deposits are exposed fluvial infill of the Paleo-Roanoke River Valley, which suggests that underlying geology is influencing modern day coastal morphodynamics in this region [Browder and McNinch, 2006; Schupp et al., 2006]. Analysis of short-term (event-scale) shoreline change data suggests that portions of this region exhibit reversing-storm hotspot behavior, wherein high erosion is closely followed by high accretion in days to weeks after the storm [List et al., 2006a]. Longer-term (decadal) shoreline change data indicate that the region is also an erosional hotspot, having an average annual retreat rate of $\sim 2 \text{ m yr}^{-1}$ [Benton et al., 1997].

3.2 Reference Line

All data are transformed to a local alongshore/cross-shore reference coordinate system based on a reference line that begins at (905,296.743 m NC State Plane Easting, 266,063.982 m NC State Plane Northing) and trends ~ 150 degrees true north along the general angle of the coastline (Figure 1). Alongshore coordinates increase to the

southeast, and cross-shore coordinates increase in the offshore direction. The reference coordinate system allows for easy analysis of alongshore and cross-shore trends, alignments, and distances between features, as well as aids in identifying three-dimensional features that often have small cross-shore amplitude to alongshore wavelength ratios.

4. METHODS

4.1 Storm Event & CLARIS Surveys

The studied storm is a Nor'Easter that occurred from 15 April 2009 to 18 April 2009. The storm produced significant wave heights > 2 m for ~ 37 hours in 8 m of water, peaking on 16 April 2009 at 3.4 m. Reported wave parameters were observed at the 8-m array located at the U.S. Army Corps of Engineer's Field Research Facility (FRF) in Duck, NC, approximately 10 km north of the study site.

The field site was surveyed with CLARIS every 12 hours during the storm, resulting in 6 surveys (Figure 2). CLARIS is a mobile, remote-sensing tool that couples X-Band Radar with a 3D Terrestrial Laser Scanner (Figure, 3). CLARIS surveys provide bathymetry estimates from radar-measured wave celerity (accurate to within $\pm 10\%$ of the water depth), morphology maps of the nearshore from time-averaged radar intensities (similar to time-averaged Argus images), and topography of the beach and dune from terrestrial scanning lidar (accuracy of ± 10 cm). For details on specific CLARIS methodology, including operation and data manipulation, please refer to Chapter 1. The CLARIS surveys provided beach topography and morphology data for all surveys and bathymetry data for 3 surveys (16 April AM survey, 16 April PM survey, and the 17 April AM survey). A lidar-only CLARIS survey was also collected on 28 April 2009 to document

the post-storm recovery of the beach. Specific details on CLARIS-observed data are presented below.

4.1.1 CLARIS - Lidar Data Analysis

After editing to remove waves, people, and other data artifacts, the lidar data are gridded in IVS Fledermaus 7.1 using a weighted moving average (1 m grid, 1 m weight). The mean-high-water (MHW) shoreline is contoured for each survey (herein referred to as “the shoreline”), and is used to analyze morphology during the storm. The shoreline is first smoothed using a 200-m running averaged to remove small-scale undulations and morphology, such as beach cusps. Similar to Lazarus and Murray [2007], we use the curvature, κ , of the smoothed MHW shoreline to identify large scale three-dimensional morphology. Convex shapes (megacusps) are defined by positive values of curvature, and concave shapes (embayments) are defined by negative values of curvature:

$$\kappa = \frac{\frac{\partial^2 y}{\partial x^2}}{\left[1 + \left(\frac{\partial y}{\partial x}\right)^2\right]^{\frac{3}{2}}} \quad (1)$$

where x and y are alongshore and cross-shore position relative to the reference line. Zero-crossings of curvature are then used to identify the alongshore length scales of observed three-dimensional features.

Alongshore variations in mean beach slope are also investigated. To calculate mean beach slope, a best-fit linear regression line is fitted to each cross-shore profile of lidar data (spaced at 1-m alongshore) between the base of the dune and the farthest seaward extent of

the edited and gridded lidar data. These data are then smoothed using a 200-m weighted moving average for comparison with the shoreline morphology data.

4.1.2 CLARIS – Bathymetry

Bathymetry data from CLARIS are obtained by solving the linear dispersion relationship and a modified cnoidal wave theory equation for water depth [see Holland et al., 2001; Chapter 1, this dissertation] using radar-derived wave celerity measurements, called “bathymetry inversion”. Root-mean-squared accuracy of the specific bathymetry inversion technique is +/- 11.6% of the actual water depth, with the highest errors within the wave breaking region (+/- 15.4%) [Chapter 1, this dissertation]. Bathymetry is estimated for the three during-storm surveys (environmental conditions must be such that waves are large and roughened by the wind in order to be adequately observed with CLARIS) and nearshore morphology is both visually and quantitatively assessed. Due to the ~11% error in water depth associated with the bathymetry inversion, the extraction of a particular isobath is difficult. To account for the uncertainty, the cross-shore location of a select isobath from a given survey is found by meaning the cross-shore location of water-depths plus or minus 10% of the select isobath every 5 m alongshore. To statistically analyze the morphology of the nearshore during the storm, the three bathymetry inversions are averaged through time and the 5- and 8-m isobaths extracted using the method described above. Isobath curvature is then calculated and compared with shoreline curvature.

In order to statistically test relationship significance, appropriate levels of sample independence need to be defined. List et al., 2003, suggest that sample independence is on the order of ~300 m in this region based on alongshore length scales of autocorrelation

independence. A similar test of autocorrelation decay performed on the shoreline and isobath data in this study find sample independence to be on the order of 500 m. As such, sample size is reduced from 1,928 samples (spaced at 5-m increments) to 19, making the degrees of freedom (dof) equal to 18 (N-1) in the alongshore direction.

4.1.3 CLARIS - Morphology Mosaics

Time-averages of radar data over the nearshore create morphology maps based on patterns of wave dissipation in the surf-zone that are similar to time-averaged video images [Ruessink et al., 2002; McNinch, 2007]. In fact, Haller and Lyzenga [2003] show that radar is less sensitive to relict foam in the surf-zone and thus a more accurate measure of active wave-breaking processes when compared with video. These morphology maps will herein be referred to as “morphology mosaics”, as information from multiple locations alongshore are mosaicked together into one seamless image. The radar morphology mosaics are then used to characterize the morphology of the surf-zone, where bathymetry estimates have higher error, and also to identify alongshore-variations in wave-dissipation patterns.

Identification of alongshore variations in dissipation of wave energy across the surf-zone is important, as wave dissipation plays a direct role in forcing important hydrodynamic processes occurring in the surf-zone, such as water level and currents [Longuet-Higgins and Stewart, 1962; Longuet-Higgins, 1970]. In particular, the width of the surf-zone has been observed to scale with the alongshore spacing of rip currents, wave-setup elevation at the shoreline, and cross-shore transitions between the dominance of wave and wind generated currents, among other processes [Longuet-Higgins and Stewart, 1964; Bowen, 1969; Hino, 1974; Symonds et al., 1982; Huntley and Short, 1992; Feddersen et al., 1998]. In these

studies, surf-zone width is often nebulously defined as the “zone of wave-breaking”, though in practice it is a difficult measurement to make, particularly in complex bathymetric settings, as time variations in wave-height (surf beat) may occasionally induce breaking significantly seaward of the shore-parallel bar [Symonds et al., 1982]. Techniques for identifying surf-zone width have included calculations based on measured wave parameters and known beach profiles [e.g. Huntley and Short, 1992], time-averaged video images of wave dissipation [Conley et al., 2008], energy flux gradients [Feddersen et al., 1998], and the distance to the crest of the shore-parallel bar [Holman et al., 2006]. Unlike video systems, where breaking waves are clearly visible as white pixels, the contact between fully breaking waves and steep-shoaling waves in radar data is less obvious, making extraction of a radar intensity contour that corresponds to the edge of the surf-zone difficult.

Similar to Holman et al. [2006], we use the location of the shore-parallel bar as a proxy for the edge of the fully-dissipating region of the surf-zone. We define the location of the offshore edge of the shore-parallel bar by the position of the mean 5-m isobath, as calculated from the bathymetry inversion. Repeated bathymetric surveys of this area during a two-year period coincident with this study indicate that the offshore base of the outermost shore-parallel bar is routinely within +/- 30 cm of 5-m of water depth [Wadman et al., 2008]. In addition, comparisons between the bathymetry-inversion derived 5-m isobath and the approximate edge of radar dissipation in the morphology mosaics independently confirm these findings (see Figure 9, presented later in the text). Unfortunately, anomalously high rates of bar movement during the storm are observed, suggesting that present levels of uncertainty associated with the bathymetry inversion currently prevent a robust analysis of bar movement during the storm. For example, at the most extreme, we observe up to 100 m of movement of the 5-m contour in 12 hours, which is significantly higher than previously published rates of bar migration observed in the northern outer banks (up to ~1 m/hr [Holman

and Sallenger, 1993]). Therefore, we conservatively use the mean position of the 5-m isobath from the three bathymetry inversions to strictly analyze alongshore variations in wave dissipation patterns during the storm, as opposed to attempting to quantify the temporal evolution of the surf-zone or bar movement.

Other morphological features, such as the identification of shore-parallel sandbars and the radar-observed waterline, are objectively identified by finding peaks (locations of intense wave-breaking), valleys (locations of less wave breaking such as over troughs), and slope changes (edges of features, such as the waterline) in cross-shore profiles of time-averaged radar intensity [Chapter 1, this dissertation].

4.2 Wave Model

The *STeady-state spectral WAVE model Full Plane* version, *STWAVE-FP*, is used to model wave transformation over nearshore bathymetry during the storm event in order to assess spatial variations in wave height and direction (and subsequently radiation stress), the dominant hydrodynamic forcing mechanisms in the surf-zone. *STWAVE-FP* solves the steady-state conservation of spectral wave action along wave rays enabling the modeling of wave transformation (refraction, shoaling, and breaking) and wind-wave generation in the nearshore [Smith et al., 2001; Smith and Sherlock, 2007]. *STWAVE-FP* assumes a mild bottom slope with no wave reflection, a spatially homogeneous offshore wave-field, steady-state waves and winds (i.e. wave-generation from winds assumes fetch-limited or fully-developed conditions), and linear refraction and shoaling. *STWAVE-FP* is used in this study because it was recently calibrated for an optimal bottom friction coefficient using the FRF cross-shore wave array in Duck, NC [Hanson et al., 2009a]. Though *STWAVE-FP* attempts to improve wave modeling within the surf-

zone through the use of a wave-steepness breaking criterion, as opposed to a simple depth-dependence breaking criterion, the non-linear nature of breaking waves in the surf-zone makes them difficult to model using linear wave theory, and thus wave heights predicted by STWAVE-FP within the surf-zone are neglected in this study. We first evaluate the performance of STWAVE-FP for the storm of interest at the FRF in Duck, NC, and then use it to model wave transformation over the irregular nearshore bathymetry in Kitty Hawk, NC.

4.2.1 Model Setup

Model setup is identical between the Duck and Kitty-Hawk field sites, with the bathymetry grids (both 10 m x 10 m resolution) the only difference in the two runs (see Figure 1 for model grid in Kitty Hawk, NC). The model is forced hourly at the offshore boundary with spectral wave and wind data from the FRF 17-m waverider buoy (note, wave conditions at the 17-m isobath in Duck, NC and Kitty Hawk, NC are assumed similar), and is run for 10 directional sweeps to ensure maximum accuracy. Water level data is input from the FRF pier gauge and held spatially constant across the domain. Bottom friction is parameterized using a spatially constant bottom friction coefficient, with manning's coefficient set to 0.073, as calibrated by Hanson et al., [2009a]. Given the heterogeneity in sediment found at the Kitty Hawk field site (rippled gravel deposits often exposed in the shore-oblique troughs), the assumption of spatially constant bottom friction may be a source of error in the model results; however, defining spatially variable bottom friction coefficients given gross sediment parameters is beyond the scope of this study.

4.2.2 Model Performance: Duck, NC

STWAVE-FP is evaluated at the FRF in Duck, NC using observations from the cross-shore wave array [Hanson et al., 2009a]. The cross-shore wave array features a suite of AWACs and waveriders located at varying depths across the inner shelf and nearshore from 5 to 26 m water depth. For this study, data from the 5-m, 6-m, 8-m, and 11-m AWACs are used to evaluate the performance of STWAVE-FP. A comparison of the model wave spectra and time series of peak wave height and period at the 5-m AWAC during the building stage of the storm can be found in Figure 4. STWAVE-FP's performance is quantitatively evaluated using Interactive Model Evaluation and Diagnostic System (IMEDS) v2.6 [Hanson et al., 2009b; Hanson and Devaliere, 2009] which computes normalized performance scores (*PS*) at each station (location of observational data) based on error metrics such as root-mean-square-error, bias, and scatter index. *PS* are combined across error metrics using a weighted average based on sample size. The resulting normalized scores for model performance range from 0 (totally uncorrelated with observations) to 1 (perfect agreement with observations). *PS* are computed for each wave component (wind-wave, mature swell, young swell, etc.) and its attributes (e.g. height, period, and direction), as well as for the full spectrum.

Overall model performance, based on comparisons at the 5-, 6-, 8-, and 11-m AWAC, is 0.9, signifying that the errors were only within 10% of the means. Across all stations for the full spectrum, the model is better at predicting wave period and direction (*PS* of 0.93 and 0.92 respectively), than wave height (*PS* of 0.87). In addition, model predictions at all stations for wind-sea height and period (*PS* of 0.78 and 0.9 respectively)

are worse than those of the swell height and period (PS of 0.89 and 0.94 for the mature swell and PS of 0.82 and 0.95 for the young swell).

Model performance for wave height is lowest at the 5-m AWAC (0.79) with STWAVE under predicting wave height across the spectrum on average by 0.29 m, with an rms error of 0.36 m. A detailed analysis of the 5-m AWAC model/observation comparison follows, as this is close to the region where wave parameters are analyzed in Kitty Hawk. Wave height is more poorly predicted for the wind-sea component at the 5-m AWAC ($PS = 0.69$, bias = -0.53 m) when compared with the swell components ($PS = 0.85$, bias = -0.16 m for young swell and $PS = 0.89$, bias = 0.09 m for mature swell). Errors are highest during the building and falling portions of the storm, with peak wave height errors reaching > -0.60 m five times during the storm (see light blue shading, Figure 4C). The errors during the building phase of the storm are expected as strong onshore winds and short period wind-waves caused breaking, a very non-linear process, to dominate wave transformation at the 5- and 6-m AWACs [J.L. Hanson, unpublished data, 2009]. During the falling portion of the storm, light offshore winds and longer period swell produce cleaner wave conditions with shoaling dominating the wave transformation [J.L. Hanson, unpublished data, 2009]. Since STWAVE has been shown to perform well during swell-dominated clean conditions such as these [Hanson et al., 2009a], the errors are somewhat unexpected, and may be improved by using a lower bottom friction coefficient within the shallower regions [J.L. Hanson, *personal communication*].

Despite these errors, the overall model performance score of 0.9 suggests that STWAVE is well suited for the modeling of this storm, with the realization that wave

heights may be under-predicted close to shore during some portions of the storm. As such, we proceed with application of the model to the Kitty Hawk field site.

4.2.3 Model Outputs

Model results at Kitty Hawk are analyzed with respect to spatial distributions in peak wave parameters, specifically: zero-moment wave height (H_{m0}), peak wave period (T_p), and mean wave direction (α_m). These parameters are output from STWAVE-FP at each grid node for each model time step (in this case, hourly), during the storm. In addition, STWAVE-FP calculates the radiation stress tensors: S_{xx} , S_{xy} , and S_{yy} , using linear wave theory and integrating through the spectrum (see Smith et al., [2001] for equations). Pertinent gradients in radiation stress are then calculated and summed to provide the total stress exerted by the waves in both the alongshore (eqn, 2a) and cross-shore (eqn. 2b) directions:

$$\tau_y = \frac{\partial S_{xy}}{\partial x} + \frac{\partial S_{yy}}{\partial y} \quad (2a)$$

$$\tau_x = \frac{\partial S_{xx}}{\partial x} + \frac{\partial S_{xy}}{\partial y} \quad (2b)$$

5. RESULTS

5.1 Morphology

Morphological evolution of the beach and nearshore bathymetry during the storm, as observed with CLARIS, is discussed below. The shoreline morphology, nearshore bathymetry, and any spatial links between them are first explored, followed by a

presentation of the morphology of the fully-dissipating surf-zone, including shore-parallel bar shape.

5.1.1 Shoreline Morphology during the Storm

Large-scale megacusps and embayments are observed along the MHW shoreline during every survey, including the pre-storm, during-storm, and post-storm surveys (Figure 5A). The megacusps and embayments are defined by zero-crossings of the shoreline curvature (Figure 5B) where values of positive curvature correspond to convex shapes (megacusps) and values of negative curvature correspond to concave shapes (embayments). The alongshore width of the individual features, defined as the distance between zero-crossings in the curvature, range in size from ~470 to 1000 m wide, averaging ~690 m and are arrhythmic. The wavelengths of the megacusp/embayment pairs, defined as the distance between every-other curvature zero crossing, range from 1090 m to 1730 m, with an average of 1440 m, and thus are much larger than common rip-current embayment or crescentic bar related features, which scale on the order of 10s to 100s of m [e.g. Sonu, 1973; Wright and Short, 1984; Walton Jr., 1999; Thornton et al., 2007]. The megacusps and embayments begin at ~3500 m alongshore and are most well defined up to ~7000 m alongshore, although two poorly defined megacusps are observed along the remaining 3 km of the study site. Shoreline curvature changes negligibly along the three most well-defined megacusps and embayments during the storm, showing no apparent straightening of the coast during this storm.

5.1.2 Nearshore Bathymetry during the Storm

The previously-observed shore-oblique bar and trough features in this region [McNinch, 2004; Browder and McNinch, 2006; Schupp et al., 2006; Miselis, 2007] are present in the pre-storm swath survey (Figure 6A) and in all of the bathymetry inversions during the storm (Figure 6B to D). Similar to the megacusp and embayment features, the shore-oblique bars and troughs are arrhythmic and present in the study site between ~3500 m alongshore and ~10,000 m alongshore, with the three most pronounced troughs lying between ~3500 and 7000 m alongshore. The troughs trend obliquely into the shoreline at an angle of ~45 degrees to the coast. They are narrower onshore at their heads and broaden offshore. Using the same convention as the shoreline, the length scales of the shore-oblique bars are investigated using the curvature of the mean 5-m isobath. The mean width of the individual bars and troughs alongshore, is ~700 m, ranging in width from 500 m to 1100 m, and the wavelengths of the bar/trough pairs range from 1100 m to 1900 m with a mean of 1400 m. For a more thorough description of these features, see Miselis [2007].

5.1.3 Morphological Links between Nearshore Bathymetry and Shoreline Morphology

Similarities are observed in the shape of the complex nearshore bathymetry and shoreline morphology during the storm (Figure 7A and B), such that the shoreline megacusp and embayment features align with the nearshore shore-oblique bars and troughs, respectively. Specifically, a cross-correlation of mean shoreline curvature with the curvature of the mean 5- and 8-m isobath produces significant results at the 95% confidence interval or higher: $R=0.69$ at a lag of 15 m, $p\text{-value} = 0.01$, $dof=18$; and

$R=0.50$ at a lag of 280 m, $p\text{-value} = 0.05$, $\text{dof}=18$ respectively (Figure 7C and D). The positive correlation coefficient indicates that where the shoreline curvature is convex (or concave) the nearshore isobaths are also convex (or concave), with a lag that increases in the offshore direction, consistent with the oblique nature of the nearshore features. Curvature amplitudes are an order of magnitude larger for the nearshore isobaths than for the shoreline.

Alongshore variations in the mean beach slope between the dune and waterline are also observed (Figure 8A), and investigated with respect to shoreline morphology (Figure 8B). Mean beach slope ranges from as flat as 2.2 degrees on the megacusp at ~3800 m alongshore to as steep as 8.2 degrees in the northern region of the study site (~2500 m alongshore). Within the most well-defined shore-oblique bar/trough and megacusp/embayment region (between 3000 m and 7500 m alongshore), a statistically significant relationship exists between shoreline curvature and mean beach slope such that megacusps are generally flatter, and embayments are steeper ($r^2=0.72$, $\text{dof} = 8$, $p\text{-value} = 0.04$, Figure 8C).

5.1.4 Surf-Zone Morphology

In addition to the shore-oblique features, shore-parallel bars are present throughout the length of the study site, and are identified by peaks in radar intensity offshore of the shoreline/swash peak (Figure 9A). The radar image is interpreted in Figure 9B, with locations of high wave dissipation (bars and swash) shaded in white and locations of low wave dissipation (troughs and offshore) shaded in blue.

In the northern portion of the study site, two shore-parallel bars are present – peak dissipation over the inner bar is roughly 75 m offshore of the shoreline and peak dissipation over the outer shore-parallel bar is ~225 m offshore of the shoreline. Between ~4300 m and ~5300m alongshore, the inner bar moves closer to the shoreline, and is only separated from the swash by ~50 m. South of 5300 m, wave dissipation over the inner bar appears to merge with wave dissipation in the swash suggesting the inner bar has either welded to the shoreline or is close enough that wave dissipation does not decrease in the trough between the bar and shoreline. The inner bar moves back offshore under Avalon pier, merging briefly again between ~7800 m and ~8200m, and then remains offshore throughout the remainder of the study site. The outer shore-parallel bar is continuous throughout the study site and has obvious landward kinks where the shore-oblique troughs extend closer to the beach (Figure 9A, B). This three-dimensionality of the shore-parallel bar persists throughout the storm, with the morphology mosaics yielding dissipation patterns and shapes very similar to Figure 9A during all of the storm surveys. Also shown in Figure 9A is the good agreement between the 5-m isobath from the bathymetry inversion and the radar morphology mosaic representation of the outer edge of the fully-dissipating region.

The cross-shore distance between the mean radar-observed waterline and mean 5-m isobath, used as a proxy for the width of the fully-dissipating region, varied significantly alongshore during the storm (Figure 9C). This region of wave dissipation was widest where shore-oblique bars were present (up to 340 m wide) and narrowest onshore of the shore-oblique troughs (down to 220 m wide).

5.2 Wave Model

The results of STWAVE-FP for the storm in Kitty Hawk show significant alongshore variations in wave height (Figure 10A) and wave direction (Figure 10B), and subsequently in along- and cross-shore gradients of radiation stress (Figure 10C and D, respectively), as the waves transform over the irregular bathymetry during the storm. Alongshore variations in wave height, direction, and radiation stress gradients are explored along a shore-parallel strike line just outside the surf-zone (500 m offshore, solid thick black line in Figure 10). Alongshore variations in cross-shore gradients of radiation stress are also explored just inside the surf-zone, along the thick dashed line in Figure 10D. To identify temporal patterns in the alongshore-variations, hourly time-stacks of wave height and wave direction along this strike line are plotted (Figure 11A and B, respectively), and analyzed with respect to peak wave parameters at the seaward boundary in 17-m of water depth (Figure 11C - D). Due to the highly oblique waves during the building portion of the Nor'Easter, strong edge effects are observed in the northern portion of the model domain, and as such analysis is restricted to the southern ~6000 m of the domain. Some of these edge effects may be negated in the future by using nested grids.

5.2.1 Alongshore Variations in Wave Height

Wave height varied alongshore during the storm, with higher waves observed on the crests of the shore-oblique bars (Figure 10A), at roughly 3500 m, 4500 m, 6000 m, 7000m and 8500 m alongshore (Figure 11A). To analyze the temporal evolution of the alongshore variations in wave height, the range and standard deviation in wave height

alongshore are also calculated along profile a-a' during the storm (Figure 11E). Wave height is defined as significantly alongshore-variable when the range in wave height alongshore is > 0.50 m and the standard deviation in wave height alongshore is > 0.1 m. These conditions occur when wave height at the seaward boundary exceeds 1 m (between the pink lines in Figure 11A,C, and E). During this period, standard deviation and range in wave height alongshore are greatest during the building period of the storm, when waves are characterized as short period and high angle (from the start of the storm until 16 Apr at 12 pm).

5.2.2 Alongshore Variations in Wave Direction

Alongshore variations in wave direction, specifically the convergence (yellow-white-blue transitions) or divergence (blue-white-yellow transitions) of wave direction relative to alongshore, are observed along the axis of the shore-oblique bars and troughs (Figure 10B). Divergence is observed at roughly 4000 m, 5500 m, 6800 m, 8000 m, and 8500 m alongshore, where as convergence is observed at ~4500 m, 5800 m, 7000 m, and 8300 m alongshore (Figure 11B). These convergence/divergence patterns do not occur until 16 Apr at 12 pm (solid green line in Figure 11B through E), just before the peak of the storm, which coincided with the transition to both long-period swell (dash-dot line, Figure 11C) and shore-normal waves (Figure 11D).

5.2.3 Alongshore Variations in Radiation Stress

Convergences and divergences in the direction of alongshore gradients in radiation stress are denoted in Figure 10C by the transition from red-white-blue and blue-

white-red, respectively. Convergences in the alongshore radiation stress gradients are seen on the crest of the shore-oblique bars at roughly 3500 m, 4500 m, 5800 m, 6800 m and 8200 m alongshore, where as divergence is seen at 4000 m, 5500 m, and 6500 m alongshore in the shore-oblique troughs, during the peak of the storm. Spatial gradients in cross-shore radiation stress are also apparent in Figure 10D. Onshore directed gradients in radiation stress indicate zones of decreasing wave height, usually due to wave breaking, where as offshore gradients in radiation stress indicate zones of increasing wave-height, usually due to wave shoaling. Thus, the most striking feature in the spatial distribution of cross-shore radiation stress gradients, occurs on the edge of the fully-dissipating surf-zone region (transition from dark blue to red at roughly 400 m offshore in Figure 10D), where stress gradients abruptly change from offshore to onshore with the onset of wave breaking.

6. DISCUSSION

6.1 Three-Dimensional Morphology

Though the coastal zone has historically been studied as a two-dimensional system [e.g. Aubrey, 1979; Birkemeier, 1984; Roelvink and Brøker, 1993; Thornton et al., 1996; Gallagher et al., 1998; Elgar et al., 2001], the ubiquity and importance of complex, three-dimensional morphology in the shoreline, surf-zone, nearshore, and inner-shelf is now widely recognized [e.g. Lippman and Holman, 1990; Ruessink et al., 2000; McNinch, 2004; Murray and Thieler, 2004; Van Enckevort et al., 2004; Plant et al., 2006; Thornton et al., 2007]. In fact, a growing body of literature exists that correlates regions with complex bathymetry and heterogeneous sediment in the nearshore and inner shelf with regions of elevated shoreline change along barrier islands, particularly along the east

and gulf coasts of the United States [McNinch, 2004; Schupp et al., 2006; Houser et al., 2008; Everts et al., 1983; Riggs et al., 1995; Schwab et al., 2000; Harris et al., 2005]. Speculations about the physical processes driving these spatial correlations assume that the complex, three-dimensional bathymetric features persist during storm events, causing wave refraction, and ultimately gradients in sediment transport that drive alongshore patterns of focused erosion at the shoreline [McNinch, 2004; Schupp et al., 2006; Houser et al., 2008], similar to the more often studied borrow-pit associated erosional hotspots [Bender and Dean, 2004; Benedet and List, 2008; Benedet et al., 2007]. While deeper, shoreface attached sand-ridge systems have been shown to persist on long time scales [Swift et al., 1972; Swift, 1981; McBride and Moslow, 1991; Calvete et al., 2001], observations of shallower nearshore and surf-zone features during storms are difficult to obtain, and as such, the first assumption of this conceptual idea has remained un-tested until this point. In fact, traditional understanding of surf-zone morphodynamics during storms specifically contradict this idea, instead documenting the evolution of surf-zones and shorelines to two-dimensional, linear forms during storms [e.g. Lippmann and Holman, 1990; Van Enckevort et al., 2004; Ranasinghe et al. 2004]. The observations of storm-resilient three-dimensional shoreline, surf-zone, and nearshore morphology presented in this study, and discussed below, suggest a morphodynamic coupling that prevents both uniform longshore transport through this region and an evolution to a two-dimensional system during storms.

6.1.1 Persistent Nearshore Bathymetry and Shoreline Morphology

Despite an extensive data set consisting of over 10 years of swath bathymetry surveys at the Kitty Hawk, NC erosional hotspot, a lack of bathymetry data during storms prevented researchers from definitively concluding whether the shore-oblique bars and troughs persisted through storms or whether they merely re-formed in the identical locations post storm [McNinch and Miselis, *In Press*]. The results presented here, most notably in Figure 6A to D, of spatially extensive, radar-derived, during-storm bathymetry definitely show for the first time shore-oblique bar and trough features persisting during > 3-m storm waves.

Given the order of magnitude of the errors in the bathymetry inversion (mean absolute error = 0.54 m; rms error = 0.72 m) compared to the order of magnitude of the nearshore bathymetric relief (~5 m from crest to trough), we are confident in the use of the bathymetry inversion to determine the presence of the shore-oblique bars and troughs through the storm. Visual comparison of both the spatially extensive bathymetric maps and the morphology of the 8-m isobath (Figure 6), as well as the curvature analysis of the mean 5- and 8-m isobath (Figure 7C), all confirm the presence of shore-oblique bars and troughs during the storm. The persistence of these features is unexpected, as sandbars are often shown to evolve and migrate during-storms [e.g. Lippmann and Holman, 1990]. For example, Konicki and Holman [2000] studied smaller scale transverse bars in the inner and outer surf-zone at Duck, NC, and observed almost constant shifting, destruction, and formation of the features. Migration of transverse bars was also observed in a modeling study during oblique waves by Ribas et al. [2003]. In addition, larger-scale shoreface attached ridges found in 4 – 20m water depth are often observed to

migrate alongshore in the direction of storm-driven longshore currents [Swift, 1981; Calvete et al., 2001; Walgreen et al., 2003]. The persistence of the surf-zone and nearshore bathymetric features in this study during a storm supports prior assertions that their location may be geologically controlled [McNinch, 2004; Browder and McNinch, 2006].

The morphology of the outermost shore-parallel bar also remains constant during the storm and appears to mirror the nearshore bathymetry, showing landward kinks wherever it is intersected by the shore-oblique troughs. The persistence of the three-dimensionality of the shore-parallel bar is probably a result of the persistence of the shore-oblique bars and troughs—the wave breaking point is closer to shore where there are steep, deep troughs, and the wave-breaking point is farther offshore on the flatter, shallower shore-oblique bars. This creates a wider zone of wave dissipation where shore-oblique bars are present and a narrower region of wave-breaking where shore-oblique troughs are present (Figure 9C). The impact of consistent alongshore variations in surf-zone width, and thus alongshore gradients in dissipation, is explored briefly in section 6.2.2 in reference to alongshore-variable water levels and surf-zone circulation.

Persistent three-dimensional morphology is also observed in the MHW-shoreline within the shore-oblique bar and trough field. Several large-scale beach megacusp and embayment features (wavelengths $\sim O(1000\text{m})$) are documented along the study site. Within the most well-defined megacusp/embayment region, mean beach slope is correlated with shoreline shape (Figure 8C; $R=0.72$ at 0 lag, $p=0.04$), such that megacusps are generally flatter and embayments are steeper, similar to erosive rip current embayment/megacusps [Dalon et al., 2007]. The shape of the features, as defined by

shoreline curvature, changes negligibly during the storm, and their position also remains fixed. The stationary persistence of these features contradicts most other observations of large-scale ($O(100-1000\text{m})$) megacusps, which document prominent alongshore migration in the direction of longshore currents [Dolan, 1971; Walton Jr, 1999; Bruun, 1954; Sonu, 1968; Verhagen, 1989; Thevenot and Kraus, 1995; Gravens, 1999; Galal and Takewaka, 2008] or smoothing [Thornton et al., 2007] during storms. In addition, the wavelengths and arrhythmic nature of the megacusp/embayment features suggest that these features are not a result of random perturbations or edge-wave forced processes such as those that may govern the evolution of smaller scale rhythmic three-dimensional shoreline features [e.g. Guza and Inman, 1975; Coco and Murray, 2007]. Instead, we argue that these persistent shoreline morphological features are controlled by the persistent nearshore bathymetry, and thus indirectly controlled by underlying geologic features [McNinch, 2004; Browder and McNinch, 2006]. Spatial evidence of this morphological coupling [see Castelle et al., 2010] is presented below, and the hydrodynamic processes possibly responsible are explored in section 6.2.

6.1.2 Morphological Coupling of the Shoreline, Surf-Zone, and Nearshore Bathymetry

A clear spatial relationship exists between nearshore bathymetry and shoreline morphology along the field site. Shoreline morphology mimics nearshore bathymetry, with shoreline megacusps and embayments aligning with nearshore shore-oblique bars and troughs, respectively (Figure 7). The spatial alignment is demonstrated by the significant positive correlation in shoreline and 5- and 8-m isobath curvature ($R=0.69$ at a lag of 15 m, $p=0.01$; and $R=0.50$ at a lag of 280 m, $p=0.05$; respectively). The increasing

spatial lag with depth between shoreline curvature and isobath curvature is consistent with the oblique nature of the features (Figure 7).

Shoreline perturbations at many scales are often associated with bathymetric features [e.g. Dolan, 1971; Sonu, 1973; Wright and Short, 1984; Short, 1999; Bender and Bean, 2004; Coco et al., 2005; Thornton et al., 2007]. The curvature analysis of map-view expressions of nearshore isobaths and the MHW-shoreline presented here suggests that there may be a quantifiable relationship between the size of a bathymetric perturbation and the resulting amplitude of the shoreline “bump” (Figure, 12). Specifically, shoreline curvature (κ_{SL}) is found to be significantly ($R^2=0.8$, $p<<0.001$) related to isobath curvature (κ_{s-m}), by the relationship below:

$$\kappa_{SL} = 0.14\kappa_{s-m} \quad (3)$$

This relationship implies that nearshore bathymetric features must contain an order of magnitude larger relief to alter the wave field enough to create the shoreline perturbations that accompany them.

The clear spatial alignment and persistence of the nearshore, surf-zone, and shoreline three-dimensional features suggests a morphological coupling along the Kitty Hawk erosional hotspot. The idea of morphological coupling is recently presented by Castelle et al., [2010], as a mechanism that blurs the line between traditional “template-forcing” approaches and more recent “self-organization” mechanisms (see Coco and Murray, [2007] for an extensive review), as the initial hydrodynamic gradients are “forced” by a specific “template”, but the resulting morphological evolution is “self-organized”. We propose that hotspots associated with persistent, irregular bathymetry, such as the Kitty Hawk erosional hotspot studied here, are governed by a morphological

coupling in which geologically-controlled bathymetry [McNinch, 2004; Browder and McNinch, 2006] alters the storm wave-field (Figure 10) and forces hydrodynamic gradients that induce positive feedbacks between flow, sediment transport, and persisting morphology of the surf-zone and beach.

6.2 Nearshore Hydrodynamics

Wave refraction over complex bathymetry is widely documented to result in regions of elevated wave height over shallower features due to wave-ray convergence, and regions of decreased wave height over deeper features due to wave-ray divergence [Munk and Traylor, 1947; O'Reilly and Guza, 1993; Bender and Dean, 2003]. Wave modeling results from STWAVE-FP in this study expectedly show a similar development of alongshore gradients in wave height and direction as the waves transform over the bathymetry (Figure 10A-B). Since nearshore bathymetry is shown to be relatively static during the storm (Figure 6), we assume that the temporal evolution of gradients in wave height and direction presented in Figure 7, and resulting radiation stress gradients (e.g. Figure 6), are an accurate representation (within the confines of the assumptions in the wave model) of wave-driven hydrodynamic forcings operating in the nearshore during the Nor'Easter. That is, although we do not use a bed-updating model, we believe it is valid to assess temporal trends in wave-driven forcing components outside of the surf-zone, where bathymetry is shown to be relatively static during the storm.

6.2.1 Wave Height and Direction

Model results show higher, converging waves over shore-oblique bar crests and lower, diverging waves over shore-oblique troughs (Figure 10 A,B). Interestingly, while gradients in wave height exist throughout the course of the storm, the initiation of the alongshore convergence/divergence patterns in wave direction begins just before the peak of the storm when the spectrum transitions from high angle wind waves to shore-parallel swell (Figure 11B-D). While stronger refraction patterns during swell conditions are expected, since longer period waves interact more with the irregular bathymetry, the stronger refraction under shore-parallel waves is counter-intuitive, since higher angle waves are often thought to produce more complex wave fields [Hartog et al., 2008]. It is important to remember that at this site, bathymetric contours are highly oblique with features oriented along the dominant high angle wave approach (northeast)—not shore-parallel or square (such as borrow-pits). Therefore, low-angle, shore-parallel waves refracting over oblique bathymetry produce a more variable nearshore wave-field at this bathymetrically complex region.

This may also explain why our results of persistent shoreline “bumps” seem to contrast those of Lazurus and Murray [2007], who observed long-term smoothing of the coastline, arguably resulting from a persistent low-angle wave climate [Ashton and Murray, 2006]. Here, the refraction of low-angle swell waves over oblique bathymetry results in spatial variations in wave height (Figure 13A) and direction (Figure 13B) that align with shoreline morphology (Figure 13C). Thus, instead of creating a smoothing effect on shoreline morphology [Ashton and Murray, 2006; Ashton et al., 2001], low-angle waves interacting with shore-oblique bathymetric features may enhance, or at the

very least maintain, three-dimensional shoreline morphology. This idea supports observations since April 2008 [Brodie and McNinch, 2008] that show shoreline morphology in this region is relatively static, persisting not only during storms, but also on seasonal time scales, even after quiescent periods (Figure 13D). Though shoreline mobility (patterns of erosion and accretion) is apparent in Figure 13D, it is interesting to note that the shoreline merely steps back and forth, preserving its shape. Clearly, more work is needed to identify how short-term processes (storm to seasonal) might scale-up to produce the decadal patterns in shoreline evolution observed by Lazarus and Murray [2007].

6.2.2 Gradients in Radiation Stress and Implications for Flow

Spatial gradients in wave height and direction lead to spatial gradients in radiation stress, a tensor that describes the direction and magnitude of the wave-driven forces acting on the water. Gradients in the cross-shore component of the total stress exerted by the waves, τ_x , occur when wave height changes, such as during wave shoaling and breaking. The most pronounced feature in Figure 10D is the sharp gradient between on- and offshore directed τ_x at the offshore edge of the surf zone. Spatial gradients in the alongshore component of the total stress exerted by the waves, τ_y , are also apparent (Figure 10C), with the strongest gradients occurring along the axes of the shore-oblique bars and troughs (Figure 10C) where waves are converging and diverging, respectively.

Solving the balanced cross-shore and alongshore momentum equations allows for prediction of flow in the surf-zone and nearshore. In the cross-shore direction, gradients in radiation stress are balanced by pressure gradients, [Longuet-Higgins and Stewart,

1964], which can lead to alongshore-variations in water level and result in pressure (head) gradients. These head gradients, are then compared with the wave driven forces (τ_y), bed shear stress, and advective accelerations to calculate the magnitude and direction of alongshore flow. Benedet and List [2008] illustrate how un-equal balancing of these forces alongshore can induce gradients in flow and resulting sediment transport that explain hotspot formation onshore of dredged borrow-pits. While we do not solve directly for flow in this study, we do make inferences as to the importance of the pressure vs. wave driven (τ_y) components of alongshore flow based on the results of our wave modeling and radar-derived morphology observations.

Outside the surf zone along profile a-a' (Figure 10), τ_y (Figure 14A) is more spatially variable than τ_x (solid line, Figure 14B). Spatial gradients in alongshore stress, τ_y , would promote flow divergence on the axes of the shore-oblique troughs and convergence on the crests of the shore-oblique bars (Figure 10C), reinforcing their existence. Elevated waves and dissipation over the shore-oblique bars (Figure 10A), however, may lead to higher-water levels, forcing head gradients in the opposite direction. Since we observe persistence of the bathymetry during the storm, and not smoothing or filling (likely outcome from head-gradient flows), we speculate alongshore flow outside the surf zone is dominated by wave-driven forces (τ_y). Interactions between flow and alongshore-variable bed shear stress (due to sediment variations between the troughs and bars) also need to be considered. For example, elevated turbulence above the coarser troughs may prevent settling, keeping more sediment in

suspension and helping to further enhance the bathymetry [Green et al., 2004; Murray and Thielert, 2004].

Model skill of STWAVE-FP is assumed low within the surf-zone due to its linear breaking criterion and prevents the extension of our analysis of the wave model results through the surf-zone and up to the beach. We can, however, analyze alongshore variations in the onset of wave breaking along profile b-b' (dashed line on Figure 10D), and compare modeled patterns of wave breaking to radar intensities from the morphology mosaic and our calculated mean width of the fully dissipating region. Profile b-b' has a mean depth of 4.5 m, ranging from 3.5 m to 6.2 m. Significant alongshore variation is observed in both τ_x (Figure 14B, dashed line) and radar intensity (Figure 14C). For example, in the gray shaded region on Figure 14B, modeled τ_x decreases from + 60 N m⁻² to -10 N m⁻², indicating a zone of intense wave breaking is immediately adjacent to a zone of wave shoaling. Within the same shaded box, radar intensity mirrors the patterns in modeled τ_x : a region of high radar intensity (wave breaking) is immediately adjacent to a region of low radar intensity (less breaking or shoaling). In addition, the mean width of the fully dissipative surf-zone during the storm decreases by about 100 m in this same region (Figure 9C).

Since water level (wave setup) scales with the amount of wave breaking (dissipation) [Longuet-Higgins and Stewart, 1964], we speculate that water levels within the surf-zone may be highly alongshore variable in this region. In contrast to outside of the surf-zone, where pressure-gradient flows may be less important, within the surf-zone, pressure gradients may contribute significantly to flow patterns. For example, increased dissipation over shore-oblique bars may create head gradients that induce divergent

alongshore flow at shoreline megacusps. The flow would then converge in embayments, flowing offshore and out the shore-oblique troughs, similar to a rip current. This flow would help to enhance the bathymetry, as well as the morphology of the shoreline, and is possibly an example of a self-organizing behavior forced by the bathymetric template.

In addition, the possible existence of strong, offshore-directed flows could result in the eventual loss of beach and inner surf-zone sediments offshore, as opposed to the continual alongshore transport of sediments through the region. Interestingly, this region was one of the few areas along the northern Outer Banks where depth of closure was not observed within the 10-m isobath during a five year period of time from 2001 to 2006 [Birkemeier et al., 2006]. Birkemeier et al. [2006] define depth of closure as the location where cross-shore profiles merge offshore, and thus represents the seaward limit of significant sediment transport. The lack of observed closure in this region suggests that sediment is mobile out to 10 m water depth (at least during large storms), significantly deeper than other regions along the Outer Banks with more simple shore-parallel contours.

Though we have not directly solved for circulation patterns and flow in this study, we believe that our during-storm observations of (1) persistent, complex, nearshore bathymetry; (2) a three-dimensional surf-zone; (3) a persistent, undulating shoreline; and (4) wave-modeled alongshore hydrodynamic gradients, all suggest that uniform, storm-driven alongshore transport is interrupted in this region. Specifically, alongshore variations in wave- and pressure-driven flow induced by the geologically controlled bathymetry may create gradients in longshore transport, perhaps even generating 2D circulation patterns, that shape the shoreline and associated erosional hotspots.

7. CONCLUSIONS

We applied a new tool, CLARIS, to the investigation of storm morphodynamics at an erosional hotspot associated with irregular nearshore bathymetry. Three-dimensional shoreline, shore-parallel bar, and nearshore bathymetry morphologies were shown to persist through the storm event, and as a result, wave dissipation was also highly alongshore variable. The shape of the beach and outer shore-parallel bar were observed to mirror that of the nearshore bathymetry, with the plan view shoreline perturbations having an order of magnitude smaller curvature than the associated bathymetric perturbations, related specifically by equation 3.

STWAVE-FP was used to model wave transformation over the nearshore bathymetry during the storm event, and indicated that alongshore gradients in wave height existed throughout the storm, and that alongshore convergence and divergence patterns in wave direction were created just before the peak of the storm, as the wave-field transitioned from high-angle wind waves to shore-parallel swell. Alongshore-variable wave height and direction patterns aligned with the three-dimensional shoreline morphology (megacusp and embayments), and consistent patterns of refraction during low-angle waves may be responsible for the longer-term persistence of curved shoreline morphology and nearshore bathymetry in this region.

Analysis of modeled radiation stress gradients suggest longshore transport outside of the surf-zone is dominated by wave-driven forces that lead to convergence on the shore-oblique bar crests and divergence in the shore-oblique bar troughs. Within the surf-zone, model results coupled with radar-observed dissipation suggest pressure-driven forces may be important, perhaps inducing 2D circulation patterns that enhance shoreline

morphology. We propose that morphological coupling [Castelle et al., 2010] exists at erosional hotspots of this type, wherein geologically controlled bathymetry forces hydrodynamic gradients that lead to self-organized morphology and flow patterns that are able to withstand high energy events, preventing traditional storm linearization from occurring. Further hydrodynamic studies including current and water level observations, as well as process-based numerical modeling studies, are needed to test these ideas.

8. ACKNOWLEDGEMENTS

The authors wish to acknowledge the US Geological Society (G09PG00195) and the US Army Corps of Engineers IRIP 653HC8 for their support of this research. We would also like to thank the entire crew at the USACE Field Research Facility for their technical and field support, especially M. Forte, J. Pipes, and H. Wadman, as well as W. Birkemeier and K. Hathaway for their preliminary review of the manuscript. In addition we would like to thank H. Stockdon and two anonymous reviewers whose comments greatly strengthened this manuscript.

REFERENCES

Ashton, A., A. B. Murray, and O. Arnoult (2001), Formation of coastline features by large-scale instabilities induced by high-angle waves, *Nature*, 414(6861), 296-300.

Ashton, A. D., and A. B. Murray (2006), High-angle wave instability and emergent shoreline shapes: 1. Modeling of sand waves, flying spits, and capes, *J. Geophys. Res.*, 111, F04011, doi:10.1029/2005JF000422.

Aubrey, D. G. (1979), Seasonal patterns of onshore/offshore sediment movement, *J. Geophys. Res.*, 84, 6347-6354.

Bender, C. J., and R. G. Dean (2003), Wave field modification by bathymetric anomalies and resulting shoreline changes: a review with recent results, *Coast. Eng.*, 49(1-2), 125-153, doi: 10.1016/S0378-3839(03)00061-9.

Bender, C. J., and R. G. Dean (2004), Potential shoreline changes induced by three-dimensional bathymetric anomalies with gradual transitions in depth, *Coast. Eng.*, 51(11-12), 1143-1161.

Benedet, L., C. W. Finkl, and W. M. Hartog (2007), Processes Controlling Development of Erosional Hot Spots on a Beach Nourishment Project, *J. Coast. Res.*, 23(1), 33-48.

Benedet, L., and J. H. List (2008), Evaluation of the physical process controlling beach changes adjacent to nearshore dredge pits, *Coast. Eng.*, 55(12), 1224-1236, doi:10.1016/j.coastaleng.2008.06.008.

Benton, S. B., C. J. Bellis, M. F. Overton, J. S. Fisher, J. L. Hench, and R. D. Dolan (1997), North Carolina long-term average annual rates of shoreline change. Prepared for Division of Coastal Management, North Carolina Department of Environment, Health, and Natural Resources, Raleigh, NC.

Birkemeier, W. (1984), Timescales of nearshore profile change, *Proceedings of the 19th Coastal Engineering Conference*, 2, ASCE, Houston, TX, 1507-1521.

Birkemeier, W., M. Forte, and H. C. Miller (2006), New mid-Atlantic observations of the depth of closure, *Proceedings 2006 International Conference on Coastal Engineering*, ASCE.

Bowen, A. J. (1969), The generation of longshore currents on a plane beach, *J. Mar. Res.*, 27, 206-215.

Bowen, A. (1980), Simple models of nearshore sedimentation: Beach profiles and longshore bars, in the coastline of Canada, *Pap. Geol. Surv. Can*, 80(10), 1-11.

- Brodie, K. L., and J. E. McNinch (2008), Storm Observations of Persistent Three-Dimensional Shoreline Morphology and Bathymetry Along a Geologically Influenced Shoreface Using X-Band Radar (BASIR), *Eos Trans. AGU*, 89(53), Fall Meet. Suppl., Abstract OS43B-1287.
- Browder, A. G., and J. E. McNinch (2006), Linking framework geology and nearshore morphology: Correlation of paleo-channels with shore-oblique sandbars and gravel outcrops, *Mar. Geol.*, 231(1-4), 141-162.
- Bruun, P. I. (1954), Migrating sand waves or sand humps, with special reference to investigations carried out on the Danish North Sea Coast: Proc. of the 5th Conf. on Coastal Engineering, *Council on Wave Research*, 260-265.
- Calvete, D., A. Falques, H. E. De Swart, and M. Walgreen (2001), Modeling the formation of shoreface-connected sand ridges on storm-dominated inner shelves, *J. Fluid Mech.*, 441, 169-193.
- Castelle, B., B. G. Ruessink, P. Bonneton, V. Marieu, N. Bruneau, and T. D. Price (2010), Coupling mechanisms in double sandbar systems. Part 1: Patterns and physical explanation, *Earth Surf. Process. Landforms*, doi: 10.1002/esp.1929.
- Castelle, B., I. L. Turner, B. G. Ruessink, and R. B. Tomlinson (2007), Impact of storms on beach erosion: Broadbeach Gold Coast, Australia, *J. Coast. Res.*, 50, 534-539.
- Coco, G., K. R. Bryan, M. O. Green, B. G. Ruessink, and I. L. Turner (2005), Video observations of shoreline and sandbar coupled dynamics, [online]. In: Townsend, Murray Robert (Editor); Walker, David (Editor). *Coasts and Ports: Coastal Living - Living Coast; Australasian Conference 2005; Proceedings*. Barton, A.C.T.: Institution of Engineers, Australia, 2005: 471-476.
- Coco, G., and A. B. Murray (2007), Patterns in the sand: From forcing templates to self-organization, *Geomorphology*, 91(3-4), 271-290, doi: 10.1016/j.geomorph.2007.04.023.
- Conley, D. C., A. Trangeled, G. Zappa, L. Gualdesi, P. Guerrini, and R. A. Holman (2008), Rapid environmental assessment in the nearshore, *J. Mar. Syst.*, 69(1-2), 74-85.
- Dalon, M. M., M. Haller, and J. Allan (2007), Morphological characteristics of rip current embayments, in *Proc. Coastal Sediments '07*, ASCE, Reston, Va., 2137-2150, doi:10.1061/40926(239)168
- Dean, R., and P. Work (1993), Interaction of navigational entrances with adjacent shorelines, *J. Coast. Res.*, *Special Issue*, 18, 91-110.
- Dolan, R. (1971), Coastal landforms: crescentic and rhythmic, *Geological Society of America Bulletin*, 82(1), 177.

- Elgar, S., E. L. Gallagher, and R. T. Guza (2001), Nearshore sandbar migration, *J. Geophys. Res.*, 106, 11623-11627.
- Everts, C., J. Battley, and P. Gibson (1983), Shoreline Movements. Report 1. Cape Henry, Virginia, to Cape Hatteras, North Carolina, 1849-1980, CERC Technical Report, Vicksburg, MS.
- Feddersen, F., R. T. Guza, S. Elgar, and T. H. C. Herbers (1998), Alongshore momentum balances in the nearshore, *J. Geophys. Res.*, 103(15), 667-15.
- Fenster, M. S., and R. Dolan (1993), Historical Shoreline Trends along the Outer Banks, North Carolina: Processes and Responses, *J. Coast. Res.*, 9(1), 172-188.
- Fenster, M.S., and R. Dolan (1996), Assessing the impact of tidal inlets on adjacent barrier island shorelines, *J. Coast. Res.*, 12(1), 294-310.
- Galal, E. M., and S. Takewaka (2008), Longshore Migration Of Shoreline Mega-Cusps Observed With X-Band Radar, *Coast. Eng. J.*, 50(3), 247-276 .
- Gallagher, E. L., S. Elgar, and R. T. Guza (1998), Observations of sand bar evolution on a natural beach, *J. Geophys. Res.*, 103(C2), 3203-3215.
- Gravens, M. B. (1999), Periodic shoreline morphology, Fire Island, New York, *Proc. Coastal Sediments '99*, ASCE, 1613-1626.
- Green, M.O., C.E. Vincent, and A.C. Trembanis (2004), Suspension of coarse and fine sand on a wave-dominated shoreface, with implications for the development of rippled scour depressions, *Cont. Shelf Res.*, 24(3), 317-335, doi: 10.1016/j.csr.2003.11.002.
- Guza, R. T., and D. L. Inman (1975), Edge waves and beach cusps, *J. Geophys. Res.*, 80(C21), 2997-3012.
- Haller, M. C., and D. R. Lyzenga (2003), Comparison of radar and video observations of shallow water breaking waves, *IEEE Trans. on Geosci. Remote Sens.*, 41(4), 832-844.
- Hanson, J. L., and E. Devaliere (2009), Interactive Model Evaluation and Diagnostics System User Guide, v2.6.
- Hanson, J. L., H. C. Friebel, and K. K. Hathaway (2009a), Coastal wave energy dissipation: observations and STWAVE-FP performance, *11-th International Workshop on Wave Hindcasting and Forecasting*, Halifax, NS, 18-23 October.
- Hanson, J. L., B. A. Tracy, H. L. Tolman, and R. D. Scott (2009b), Pacific hindcast performance of three numerical wave models, *J. Atmos. Ocean. Technol.*, 26(8), 1614-1633.

- Harris, M. S., P. T. Gayes, J. L. Kindinger, J. G. Flocks, D. E. Krantz, and P. Donovan (2005), Quaternary geomorphology and modern coastal development in response to an inherent geologic framework: an example from Charleston, South Carolina, *J. Coast. Res.*, 21(1), 42-64.
- Hartog, W. M., L. Benedet, D. J. R. Walstra, M. van Koningsveld, M. J. F. Stive, and C. W. Finkl (2008), Mechanisms that Influence the Performance of Beach Nourishment: A Case Study in Delray Beach, Florida, USA, *J. Coast. Res.*, 24(5), 1304-1319.
- Hayes, M. O. (1979), Barrier island morphology as a function of tidal and wave regime, In *Barrier Islands from the Gulf of St. Lawrence to the Gulf of Mexico* (ed. S.P. Leatherman), *Academic Press*, New York, 1-28.
- Hino, M. (1974), Theory on formation of rip-current and cuspidal coast, In: *Proc. 14th Int. Conf. Coastal Eng.*, Copenhagen, pp.901-919.
- Hoefel, F., and S. Elgar (2003), Wave-Induced Sediment Transport and Sandbar Migration, *Science*, 299(5614), 1885-1887.
- Holland, K. T. (2001), Application of the linear dispersion relation with respect to depth inversion and remotely sensed imagery, *IEEE Trans. on Geosci. Remote Sens.*, 39(9), 2060-2072, doi: 10.1109/36.951097.
- Holland, K. T., and R. A. Holman (1996), Field observations of beach cusps and swash motions, *Mar. Geol.*, 134(1-2), 77-93.
- Holman, R., and A. Sallenger (1993), Sand bar generation: A discussion of the Duck experiment series, *J. Coast. Res.*, 15, 76-92.
- Holman, R. A., G. Symonds, E. B. Thornton, and R. Ranasinghe (2006), Rip spacing and persistence on an embayed beach, *J. Geophys. Res.*, 111, C01006, doi:10.1029/2005JC002965.
- Houser, C., C. Hapke, and S. Hamilton (2008), Controls on coastal dune morphology, shoreline erosion and barrier island response to extreme storms, *Geomorphology*, 100(3-4), 223-240.
- Huntley, D. A., and A. D. Short (1992), On the spacing between observed rip currents, *Coast. Eng.*, 17(3-4), 211-225.
- Komar, P. D. (1998), *Beach Processes and Sedimentation*, 2nd ed., Prentice-Hall, Inc, Upper Saddle River, NJ.
- Konicki, K. M., and R. A. Holman (2000), The statistics and kinematics of transverse sand bars on an open coast, *Mar. Geol.*, 169(1), 69-101.

Kraus, N. C., and F. A. Galgano (2001), Beach erosional hot spots: Types, causes, and solutions, *Coastal and Hydraulics Engineering Technical Note ERDC*, Vicksburg, MS.

Lafon, V., H. Dupuis, R. Butel, B. Castelle, D. Michel, H. Howa, and D. De Melo Apoluceno (2005), Morphodynamics of nearshore rhythmic sandbars in a mixed-energy environment (SW France): 2. Physical forcing analysis, *Estuar. Coast. Shelf Sci.*, 65(3), 449-462.

Lazarus, E. D., and A. B. Murray (2007), Process signatures in regional patterns of shoreline change on annual to decadal time scales, *Geophys. Res. Lett.*, 34, doi: 10.1029/2007GL031047.

Lee, G., R. J. Nicholls, W. A. Birkemeier, and S. P. Leatherman (1995), A conceptual fairweather-storm model of beach nearshore profile evolution at Duck, North Carolina, USA, *J. Coast. Res.*, 11(4), 1157-1166.

Lee, G., R. J. Nicholls, and W. A. Birkemeier (1998), Storm-driven variability of the beach-nearshore profile at Duck, North Carolina, USA, 1981–1991, *Mar. Geol.*, 148(3-4), 163-177.

Lippmann, T. C., and R. A. Holman (1990), The spatial and temporal variability of sand bar morphology, *J. Geophys. Res.*, 95(C7), 11575-11590, doi:10.1029/JC095iC07p11575.

List, J. H., A. S. Farris, and C. Sullivan (2006), Reversing storm hotspots on sandy beaches: Spatial and temporal characteristics, *Mar. Geol.*, 226(3-4), 261-279.

Longuet-Higgins, M. S. (1970), Longshore Currents Generated by Obliquely Incident Sea Waves, *J. Geophys. Res.*, 75(33), 6790-6801, doi:10.1029/JC075i033p06790.

Longuet-Higgins, M. S., and R. W. Stewart (1962), Radiation stress and mass transport in gravity waves, with application to surf beats, *J. Fluid Mech.*, 13, 481-504.

Longuet-Higgins, M. S., and R. W. Stewart (1964), Radiation stresses in water waves; a physical discussion, with applications, *Deep Sea Res.*, 11, 529-529-562.

McBride, R. A., and T. F. Moslow (1991), Origin, evolution, and distribution of shoreface sand ridges, Atlantic inner shelf, USA, *Mar. Geol.*, 97(1-2), 57-85.

McNinch, J. E. (2004), Geologic control in the nearshore: shore-oblique sandbars and shoreline erosional hotspots, Mid-Atlantic Bight, USA, *Mar. Geol.*, 211(1-2), 121-141.

McNinch, J. E. (2007), Bar and Swash Imaging Radar (BASIR): A Mobile X-band Radar Designed for Mapping Nearshore Sand Bars and Swash-Defined Shorelines Over Large Distances, *J. Coast. Res.*, 23(1), 59-74.

McNinch, J. E. and J. L. Miselis (2009), Geology metrics for predicting shoreline change using seabed and sub-bottom observations from the surf zone, edited by C. Sherwood and M. Li, *Journal of Sedimentology (Special Publication)*, in press.

Miselis, J. L. (2007), Nearshore morphology and lithology: links to framework geology and shoreline change, Ph.D. Dissertation, School of Marine Science, William and Mary, Williamsburg, VA.

Munk, W. H., and M. A. Traylor (1947), Refraction of ocean waves: a process linking underwater topography to beach erosion, *J. Geol.*, 55(1), 1-26.

Murray, A. B., and E. R. Thieler (2004), A new hypothesis and exploratory model for the formation of large-scale inner-shelf sediment sorting and "rippled scour depressions", *Cont. Shelf Res.*, 24(3), 295-315, doi: 10.1016/j.csr.2003.11.001.

O'Reilly, W. C., and R. T. Guza (1993), Comparison of two spectral wave models in the Southern California Bight. *Coast. Eng.*, 19(3), 263-282.

Plant, N. G., K. T. Holland, and R. A. Holman (2006), A dynamical attractor governs beach response to storms, *Geophys. Res. Lett.*, 33(17), doi:10.1029/2006GL027105.

Plant, N. G., B. G. Ruessink, and K. M. Wijnberg (2001), Morphologic properties derived from a simple cross-shore sediment transport model, *J. Geophys. Res.*, 106(C1), 945-958, doi:10.1029/2000JC900143.

Ranasinghe, R., G. Symonds, K. Black, and R. A. Holman (2004), Morphodynamics of intermediate beaches: a video imaging and numerical modeling study, *Coast. Eng.*, 51(7), 629-655.

Ribas, F., A. Falqués, and A. Montoto (2003), Nearshore oblique sand bars, *J. Geophys. Res.*, 108(C4), doi:10.1029/2001JC000985.

Riggs, S. R., W. J. Cleary, and S. W. Snyder (1995), Influence of inherited geologic framework on barrier shoreface morphology and dynamics, *Mar. Geol.*, 126(1-4), 213-234, doi: 10.1016/0025-3227(95)00079-E.

Roelvink, J. A., and I. Brøker (1993), Cross-shore profile models, *Coast. Eng.*, 21(1-3), 163-191.

Ruessink, B. G., P. S. Bell, I. M. J. van Enckevort, and S. G. J. Aarninkhof (2002), Nearshore bar crest location quantified from time-averaged X-band radar images, *Coast. Eng.*, 45(1), 19-32.

Ruessink, B. G., Y. Kuriyama, A. Reniers, J. A. Roelvink, and D. J. R. Walstra (2007), Modeling cross-shore sandbar behavior on the timescale of weeks, *J. Geophys. Res.*, 112(F3), doi:10.1029/2006JF000730.

- Ruessink, B. G., I. M. J. van Enckevort, K. S. Kingston, and M. A. Davidson (2000), Analysis of observed two- and three-dimensional nearshore bar behavior, *Mar. Geol.*, 169(1), 161-183.
- Sallenger Jr, A. H. (2000), Storm Impact Scale for Barrier Islands, *J. Coast. Res.*, 16(3), 890-895.
- Schupp, C. A., J. E. McNinch, and J. H. List (2006), Nearshore shore-oblique bars, gravel outcrops, and their correlation to shoreline change, *Mar. Geol.*, 233(1-4), 63-79.
- Schwab, W. C., E. R. Thieler, J. R. Allen, D. S. Foster, B. A. Swift, and J. F. Denny (2000), Influence of inner-continental shelf geologic framework on the evolution and behavior of the barrier-island system between Fire Island Inlet and Shinnecock Inlet, Long Island, New York, *J. Coast. Res.*, 16(2), 408-422.
- Sénéchal, N., T. Gouriou, B. Castelle, J. P. Parisot, S. Capo, S. Bujan, and H. Howa (2009), Morphodynamic response of a meso-to macro-tidal intermediate beach based on a long-term data set, *Geomorphology*, 107(3-4), 263-274.
- Short, A. D. (Ed.) (1999), *Handbook of Beach and Shoreface Morphodynamics*, J. Wiley and Sons, Chichester, 379.
- Smit, M. W. J., A. J. H. M. Reniers, and M. J. F. Stive (2005), Nearshore bar response to time varying conditions, *Proc. 5th International Conf. on Coastal Dynamics*, Barcelona.
- Smith, J. M., and A. R. Sherlock (2007), Full-plane STWAVE with bottom friction: II. Model overview, *System-Wide Water Resources Program Technical Note*, US Army Engineer Research and Development Center, Vicksburg, MS.
- Smith, J. M., A. R. Sherlock, and D. T. Resio (2001), STWAVE: STEady-state spectral WAVE model: User's manual for STWAVE Version 3.0, *Supplemental Report ERDC/CHL SR-01-1*, US Army Engineer Research and Development Center, Vicksburg, MS.
- Sonu, C. J. (1968), Collective movement of sediment in littoral environments, *Proc. 11th Conf. Coastal Engineering*, London, pp. 373-399.
- Sonu, C. J. (1973), Three-dimensional beach changes, *J. Geol.*, 81(1), 42-64.
- Stive, M. J. F., S. G. J. Aarninkhof, L. Hamm, H. Hanson, M. Larson, K. M. Wijnberg, R. J. Nicholls, and M. Capobianco (2002), Variability of shore and shoreline evolution, *Coast. Eng.*, 47(2), 211-235.
- Stockdon, H. F., A. H. Sallenger, R. A. Holman, and P. A. Howd (2007), A simple model for the spatially-variable coastal response to hurricanes, *Mar. Geol.*, 238(1-4), 1-20.

- Swift, D. J. P. (1981), Evolution of a classic sand ridge field: Maryland sector, North American inner shelf, *Sedimentology*, 28(4), 461-482.
- Swift, D. J. P., B. Holliday, N. Avignone, and G. Shideler (1972), Anatomy of a shore face ridge system, False Cape, Virginia, *Mar. Geol.*, 12(1), 59-84.
- Symonds, G., D. A. Huntley, and A. J. Bowen (1982), Long Wave Generation by a Time-Varying Breakpoint, *J. Geophys. Res.*, 87(C1), 492-498.
- Thevenot, M. M., and N. C. Kraus (1995), Longshore sand waves at Southampton Beach, New York: observation and numerical simulation of their movement, *Mar. Geol.*, 126(1), 249-269.
- Thornton, E. B., R. T. Humiston, and W. Birkemeier (1996), Bar/trough generation on a natural beach, *J. Geophys. Res.*, 101(C5), 12097-12110.
- Thornton, E. B., J. MacMahan, and A. H. Sallenger (2007), Rip currents, mega-cusps, and eroding dunes, *Mar. Geol.*, 240(1-4), 151-167.
- Van Enckevort, I. M. J., B. G. Ruessink, G. Coco, K. Suzuki, I. L. Turner, N. G. Plant, and R. A. Holman (2004), Observations of nearshore crescentic sandbars, *J. Geophys. Res.*, 109(C6), doi:10.1029/2003JC002214.
- van Rijn, L. C., D. J. R. Walstra, B. Grasmeijer, J. Sutherland, S. Pan, and J. P. Sierra (2003), The predictability of cross-shore bed evolution of sandy beaches at the time scale of storms and seasons using process-based Profile models, *Coast. Eng.*, 47(3), 295-327.
- Verhagen, H. J. (1989), Sand waves along the Dutch coast, *Coast. Eng.*, 13(2), 129-147, doi:10.1016/0378-3839(89)90020-3.
- Wadman, H.M., McNinch, J.E., Hanson, J.L. (2008) A Morphological Model Test Bed for MORPHOS Model Development in the Outer Banks, North Carolina: Survey Report: November 2007 - May 2008, 36.
- Walgreen, M., H. E. De Swart, and D. Calvete (2003), Effect of grain size sorting on the formation of shoreface-connected sand ridges, *J. Geophys. Res.*, 108(C3), doi:10.1029/2002JC001435.
- Walton Jr, T. L. (1999), Shoreline rhythmic pattern analysis, *J. Coast. Res.*, 15(2), 379-387.
- Wright, L. D., and A. D. Short (1984), Morphodynamic variability of beaches and surf zones, a synthesis, *Mar. Geol.*, 56, 92-118.

FIGURE CAPTIONS

Figure 1: Location map of study site in Kitty Hawk, NC showing an aerial photograph of the area with 2006 swath bathymetry (colors) and the reference line (black line) with distances alongshore.

Figure 2: Nor'easter wave conditions and CLARIS survey times. Solid black line depicts significant wave height in 8-m water depth, and the dashed line shows peak period, both recorded by the FRF linear array. Colored vertical lines indicate the times of the semi-daily CLARIS surveys.

Figure 3: Coastal LiDAR and Radar Imaging System (CLARIS). A mobile, remote-sensing vehicle that couples X-band radar and a terrestrial laser scanner.

Figure 4: STWAVE Spectrum Comparison at 5-m AWAC, Duck, NC. An example spectrum during the building portion of the storm illustrates the good agreement between observations (panel A) and model results (panel B). Wave height (panel C) and peak period (panel D) also show good agreement, with the highest residuals in significant wave height occurring during the building and falling portions of the storm (light blue shading, panel C). Panel E shows the wind field for the storm, with the red dashed line indicating time of the spectrum comparison.

Figure 5: Shoreline morphology during the storm. Distance along the reference line is plotted on the x-axis. Sequential CLARIS surveys (colored lines) of the MHW shoreline position during the storm (Panel A) showed persistent megacusps (blue-shaded boxes) and embayments that were defined by negative and positive values of shoreline curvature, respectively (panel B).

Figure 6: Nearshore bathymetry during the storm. Distance along the reference line is plotted on the x-axis, and cross-shore distance from the reference line is plotted on the y-axis for all panels. Shore-oblique bars and troughs were observed in the pre-storm swath bathymetry survey (panel A), and in the during-storm bathymetry inversions on 16 Apr AM (panel B), 16 Apr PM (panel C), and 17 Apr AM (panel D). The 8-m isobath (black line) and the region of depths within plus or minus 10% of 8 m (dotted black line) have been highlighted to illustrate the persistence of the nearshore features.

Figure 7: Spatial alignment of morphological features. The mean nearshore bathymetry during the storm (panel A) mirrored the mean MHW shoreline morphology during the storm (panel B), with nearshore shore-oblique bars/troughs aligning with shoreline megacusps/embayments. This relationship was exemplified by the similarities in curvature (panel C) of the shoreline (solid blue line) with curvature of the 5- (solid black line) and 8-m (dashed black line) isobath. Cross-correlation analyses (panel D) revealed a significant positive relationship between shoreline and isobath curvature with a lag that increased offshore.

Figure 8: Shoreline morphology to beach slope comparison. Mean beach slope (solid line, panel A and B), shoreline morphology (dashed line, panel A), and shoreline curvature (dotted line, panel B) are plotted along the entire study site. In panel C, mean beach slope is statistically related to shoreline curvature ($R^2=0.72$, $p=0.04$) within the most well-defined shore oblique bar/trough field (gray region, panel B) such that convex regions are flatter and concave regions are steeper.

Figure 9: Shore-parallel bar and surf-zone morphology during the storm. Distance along the reference line is plotted on the x-axis for all panels. The radar morphology mosaic is shown in panel A, with warmer colors representing high radar intensity returns, and cooler colors representing low radar intensity storms. The waterline (thick solid line), swash zone (narrow solid black line), inner bar (dashed black line), and 5-m isobath (dotted black line), are denoted for the 16AM survey. Interpretation of the morphology mosaic is shown in panel B. White regions correspond to places of wave breaking, blue regions correspond to places of low wave dissipation, and the yellow region represents the beach. Note the good agreement of the mean 5-m isobath with the offshore edge of the surf-zone. The distance between the mean waterline (solid black line, panel B) and the mean 5-m isobath is shown in panel C, and shows substantial alongshore variability during the storm.

Figure 10: Results of STWAVE-FP in Kitty Hawk at the peak of the storm. Distance along the reference line is on the x-axis and distance cross-shore from the reference line is on the y-axis for all panels. Alongshore variations in wave height (panel A) are

observed during the storm event, with higher waves concentrated on the crests of the shore-oblique bars. Alongshore variations in wave direction are also observed (panel B), with patterns of convergence (yellow-white-blue transitions) and divergence (blue-white-yellow transitions). Wave direction is shown in degrees relative to shore-normal, with positive degrees (warmer colors) indicating a counter-clockwise deflection and negative degrees (cooler colors) indicating a clockwise deflection. Alongshore and cross-shore stress are shown in panels C and D respectively. The thick solid black line (a - a') and the dashed line (b - b') in panel D identify the location of shore-parallel strike lines used in subsequent analysis.

Figure 11: Analysis of alongshore variations in the modeled wave field. Timestacks of wave height (panel A) and wave direction (panel B) along profile a - a' (Figure 10) demonstrate the temporal evolution of the complex wave field. Development of wave direction convergence (yellow-white-blue transition) and divergence (blue-white-yellow transition) is indicated by the green line (in panels B-D). Timing of the development of the wave field is analyzed with respect to wave parameters at the seaward boundary of the model in 17-m water depth, with height and period shown in panel C, and direction shown in panel D. Convergence and divergence in wave direction begins just before the peak of the storm as the wave field transitions to long-period (intersection of green line and dash-dot line in panel C) and low angle swell (indicated by the green line and near shore-normal arrows in panel D). Alongshore variations in wave height, defined by the alongshore standard deviation (solid line, panel E) and range (dashed line, panel E) in

wave height, are significant when wave height exceeds 1m (between the pink lines in Panels A, C, and E).

Figure 12: Relationship between isobath and shoreline curvature. Curvature of the MHW shoreline (y-axis) is an order of magnitude smaller than the curvature of the 5-m isobath (x-axis). The reduced number of data points represent spatially independent data.

Figure 13: Alongshore variations in wave parameters and shoreline morphology. A relationship was observed between alongshore variations in wave height (panel A) and wave direction (panel B) with shoreline morphology (panels C and D): higher (gray boxes), diverging waves (indicated by red opposing arrows) aligned with shoreline embayments and lower, converging waves (indicated by green arrows) aligned with shoreline megacusps (panel C). Panel D shows the persistence of shoreline morphology in this region since April 2008.

Figure 14: Alongshore variations in hydrodynamic forces. Alongshore variations in t_y , shown here along profile a - a' (panel A), may drive convergent and divergent flow in the nearshore. Alongshore variations in t_x (panel B) are significantly greater along profile b-b', just inside the fully-dissipated region (dashed line), than along profile a-a' (solid line), and are similar to alongshore variations in radar intensity (panel C) at the same location. The shaded gray box indicates the region discussed in depth within the text.

Figure 1

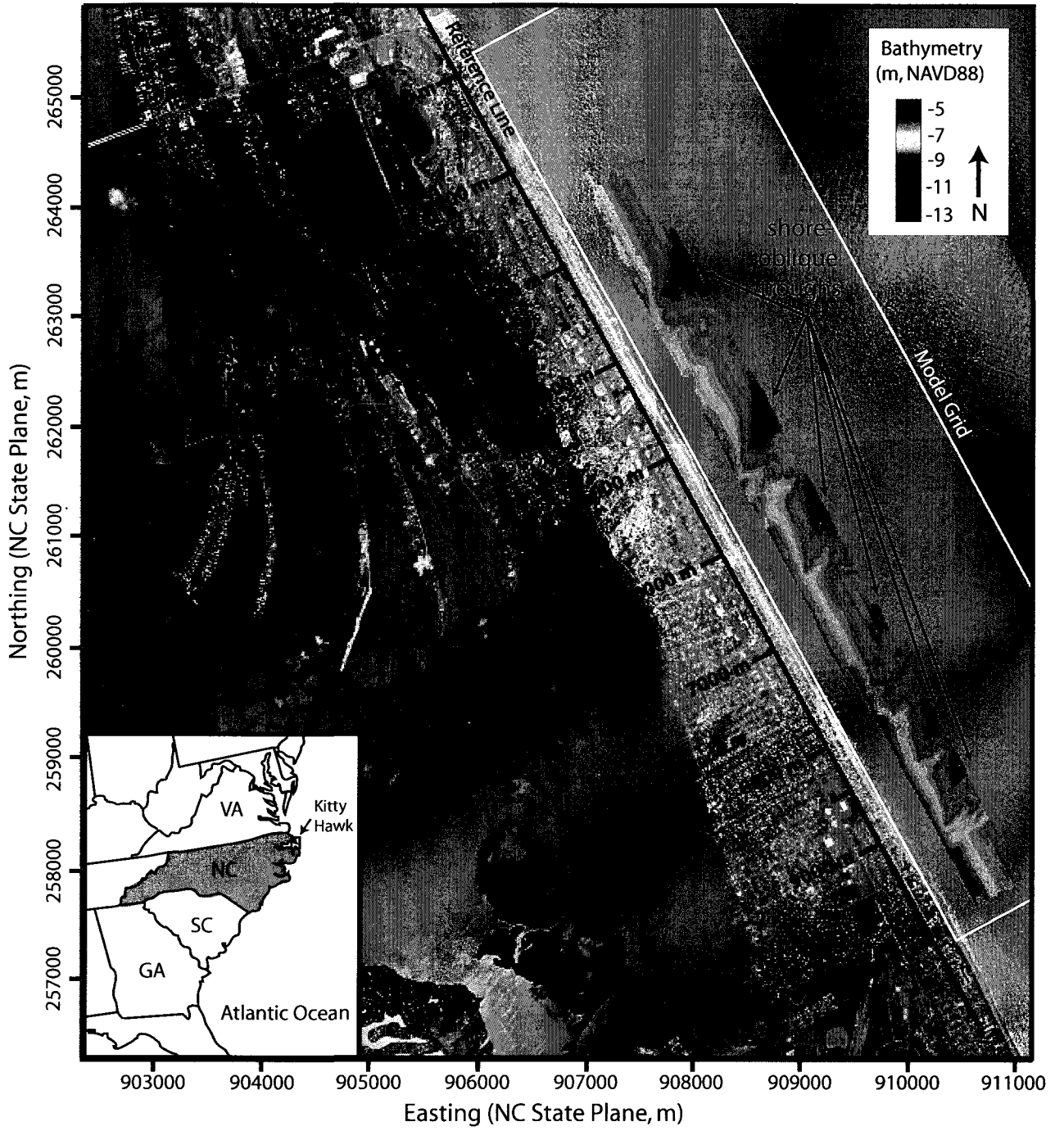


Figure 2

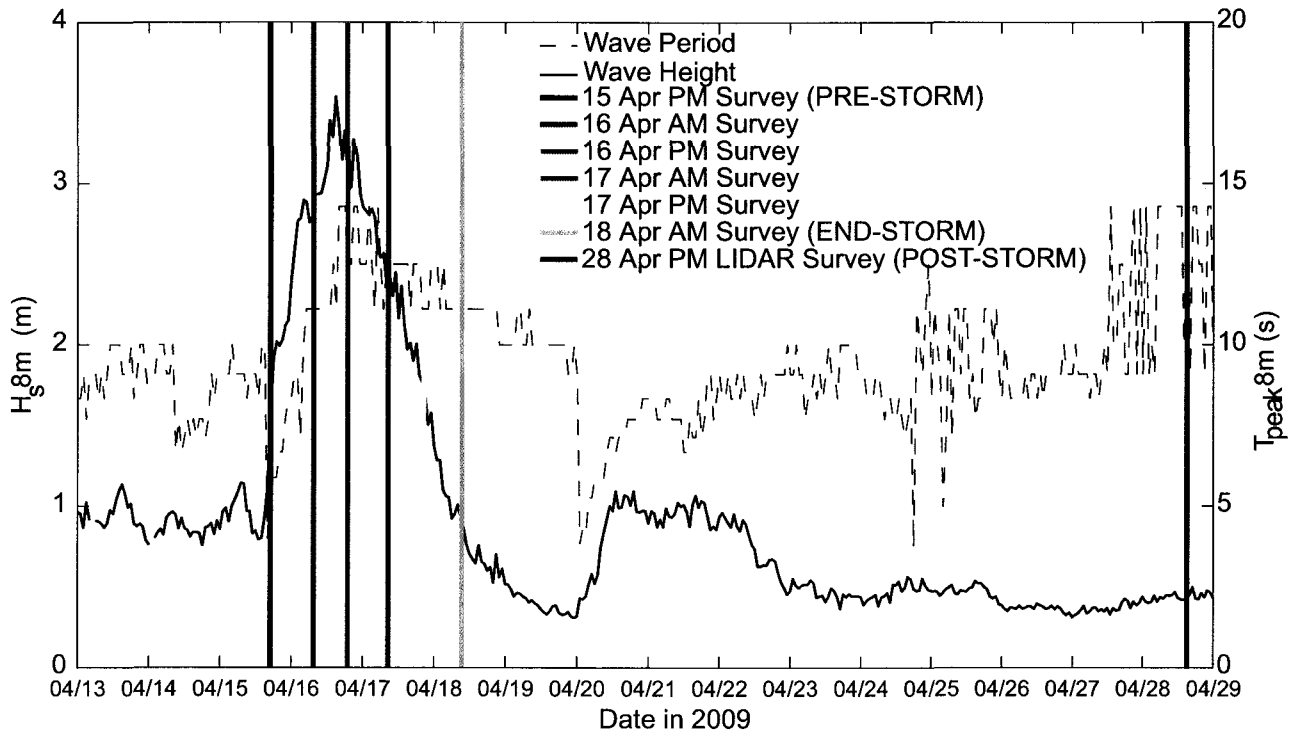


Figure 3



Figure 4

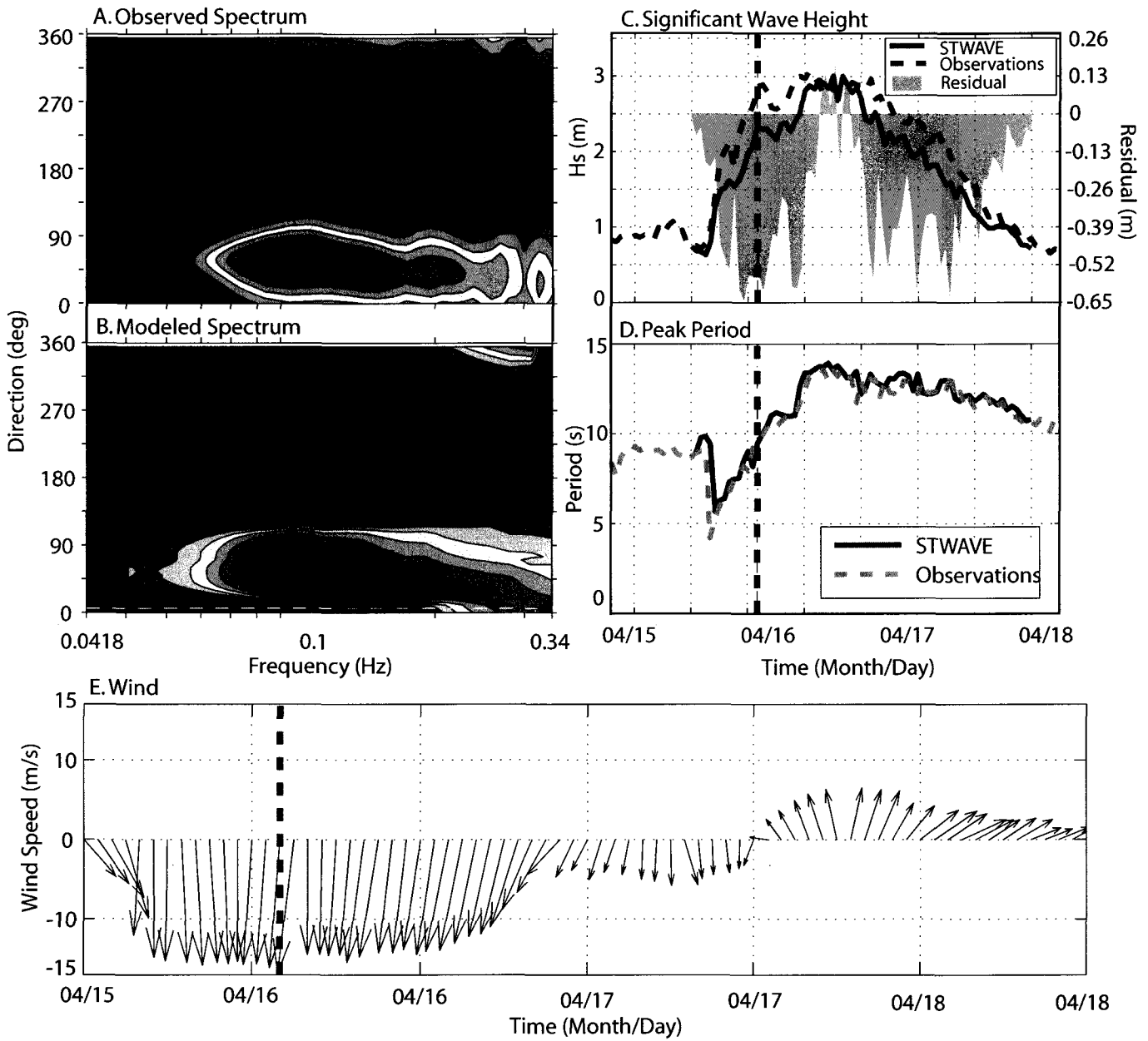


Figure 5

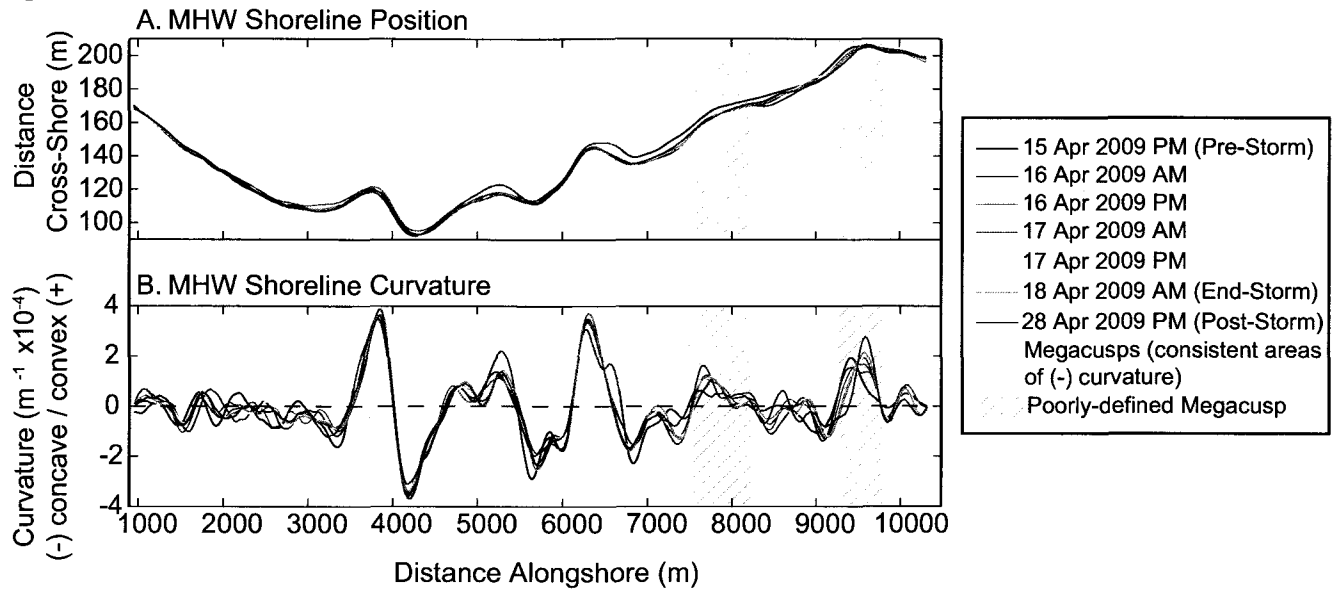


Figure 6

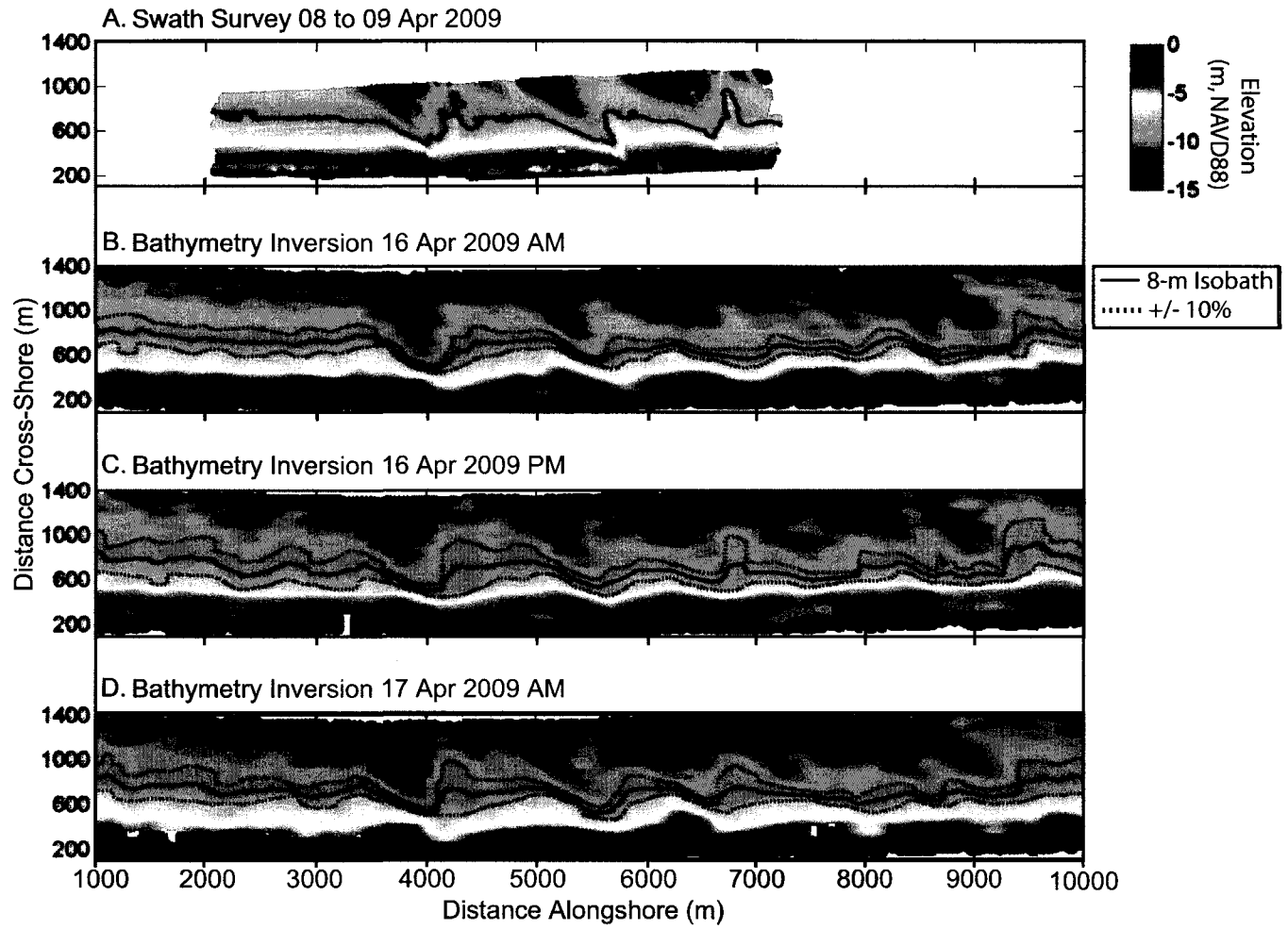


Figure 7

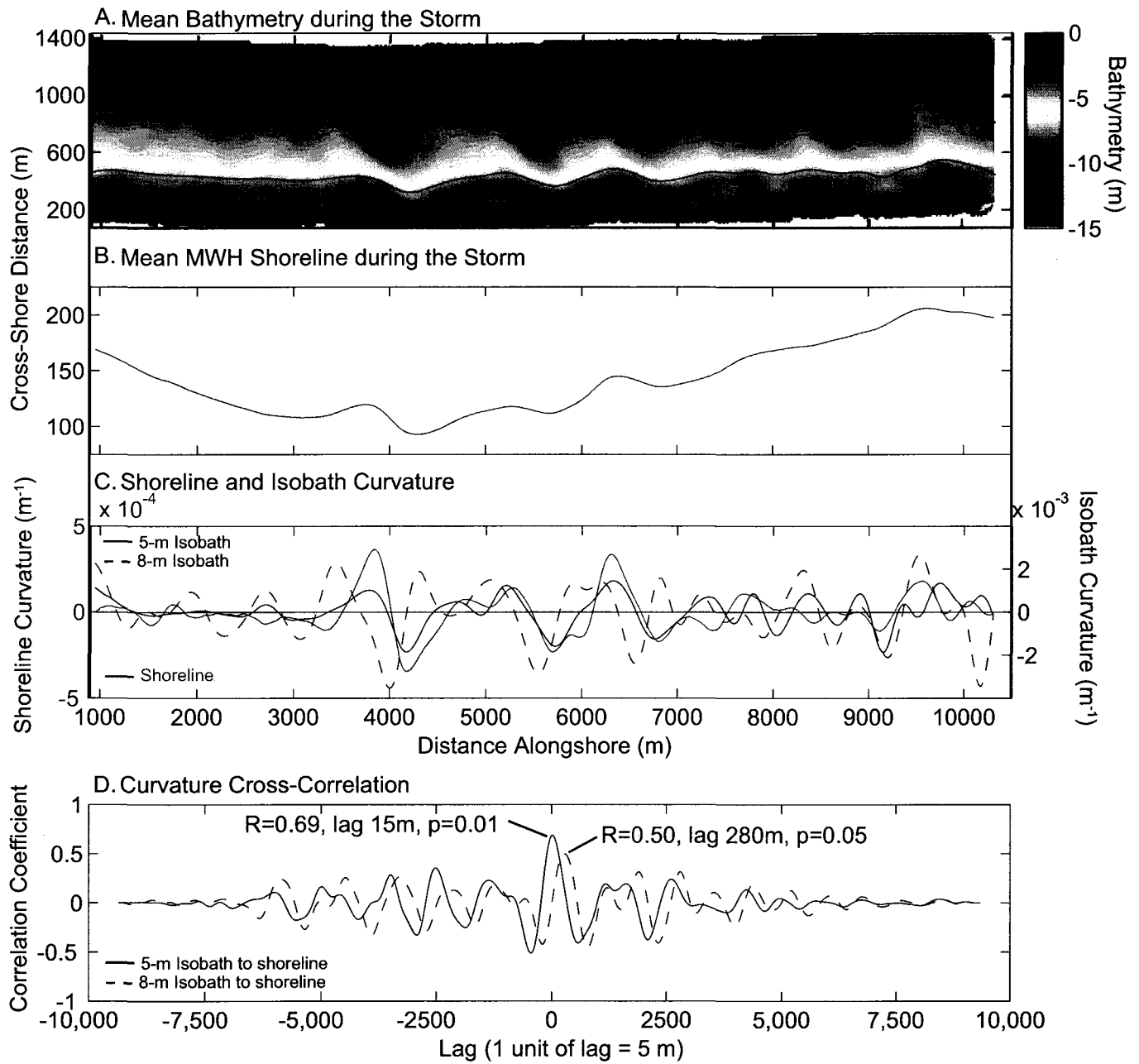


Figure 8

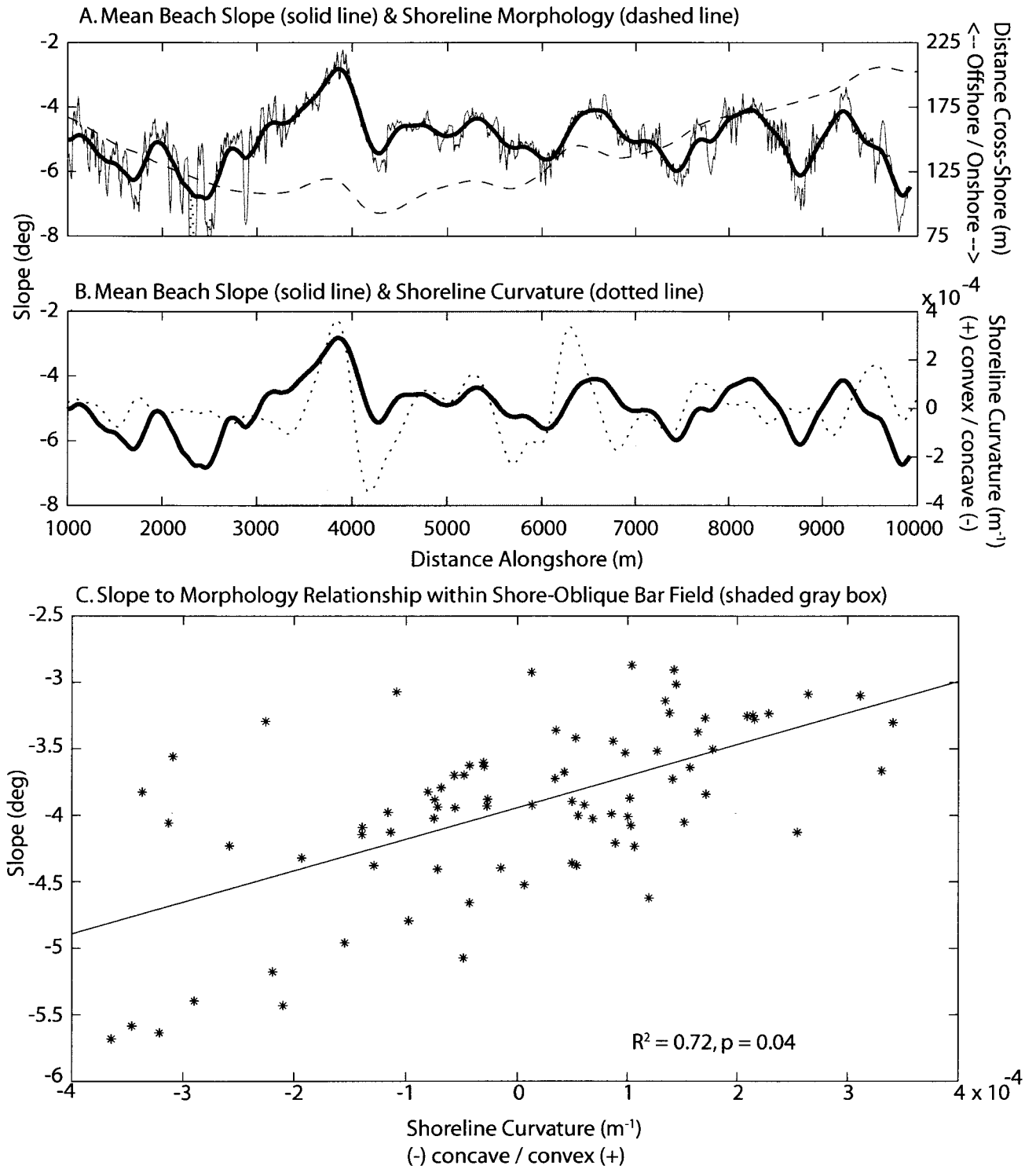
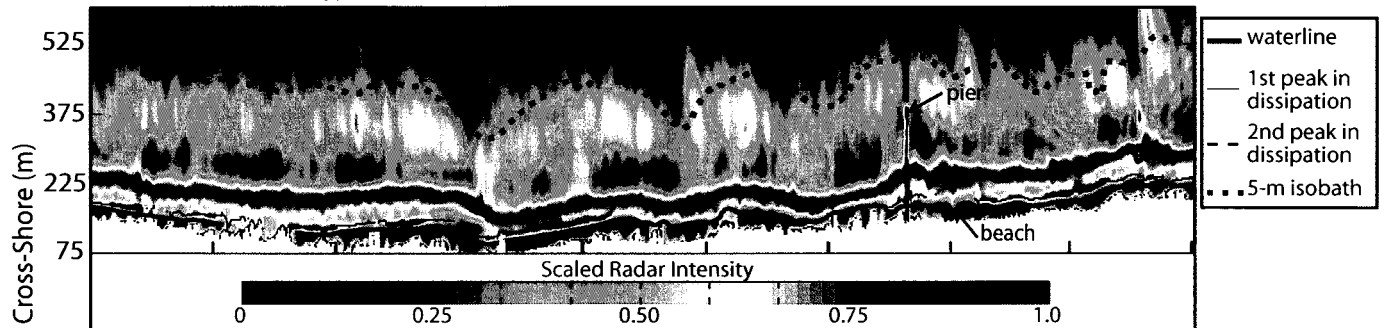
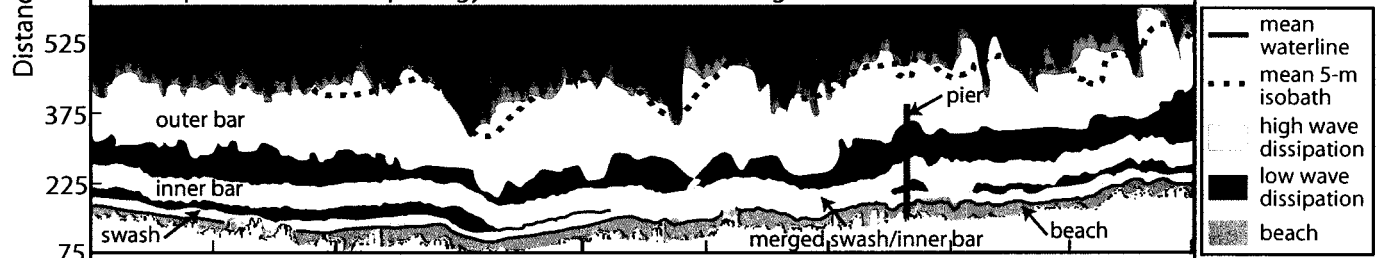


Figure 9

A. Radar Morphology Mosaic with Identified Morphological Features and 5-m Isobath (16 AM Survey)



B. Interpreted Radar Morphology Mosaic with Mean During-Storm 5-m Isobath and Waterline



C. Mean Distance between the 5-m Isobath and Waterline during the Storm

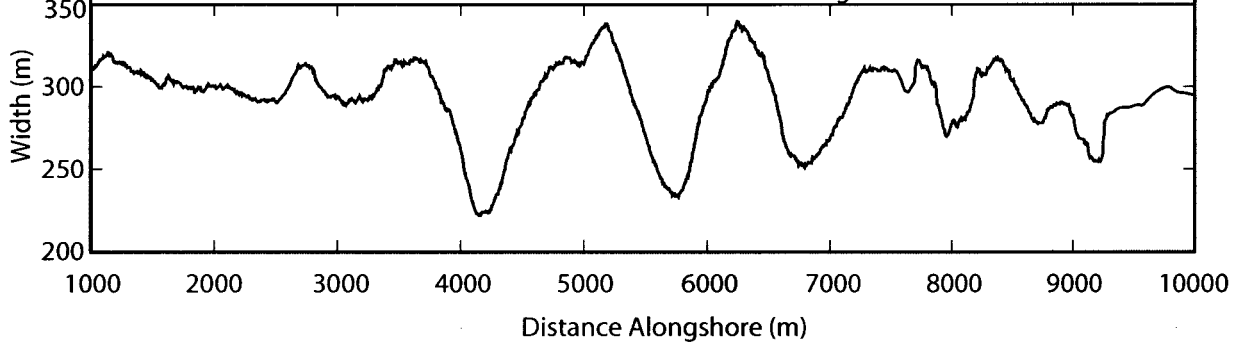


Figure 10

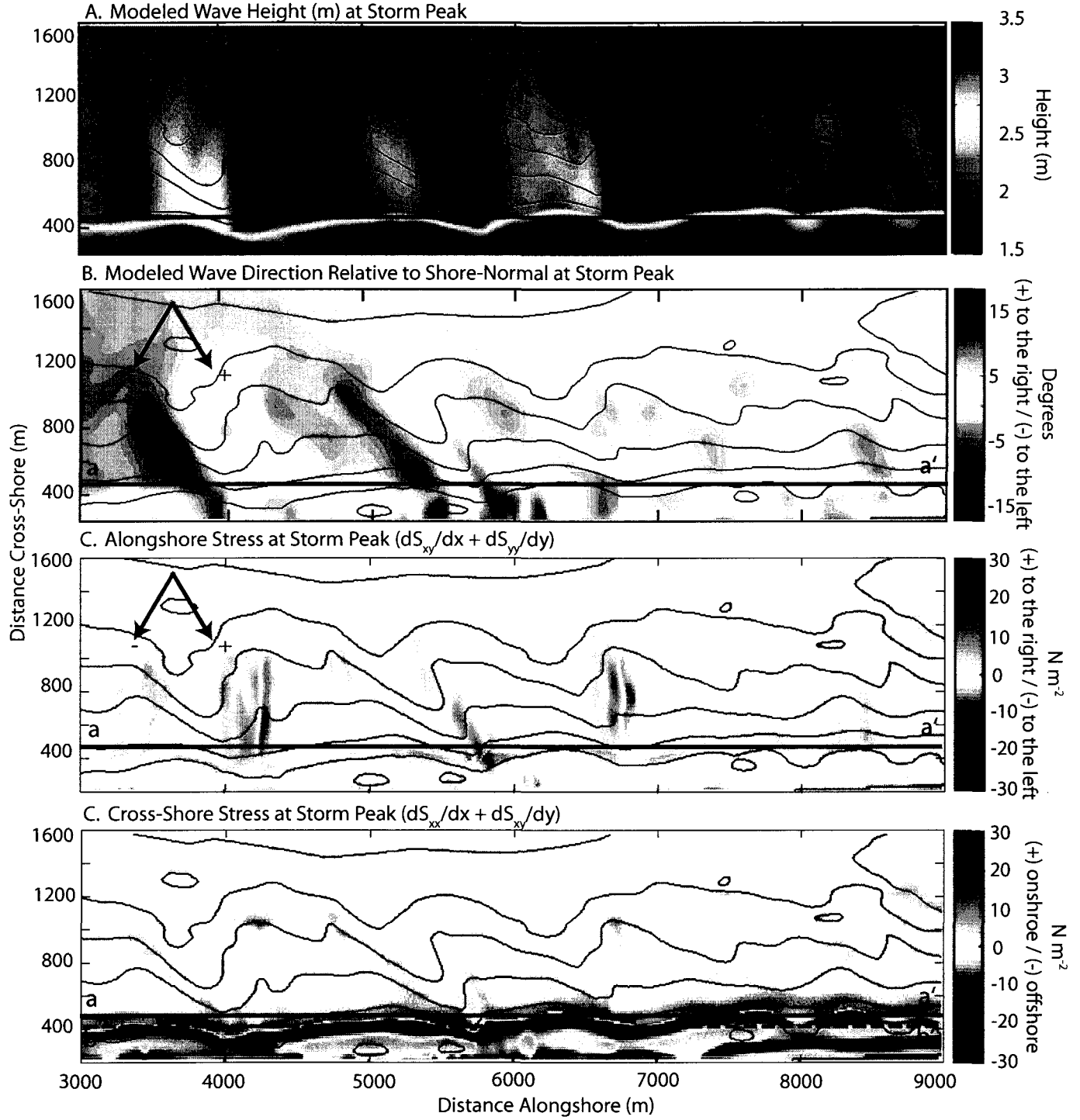


Figure 11

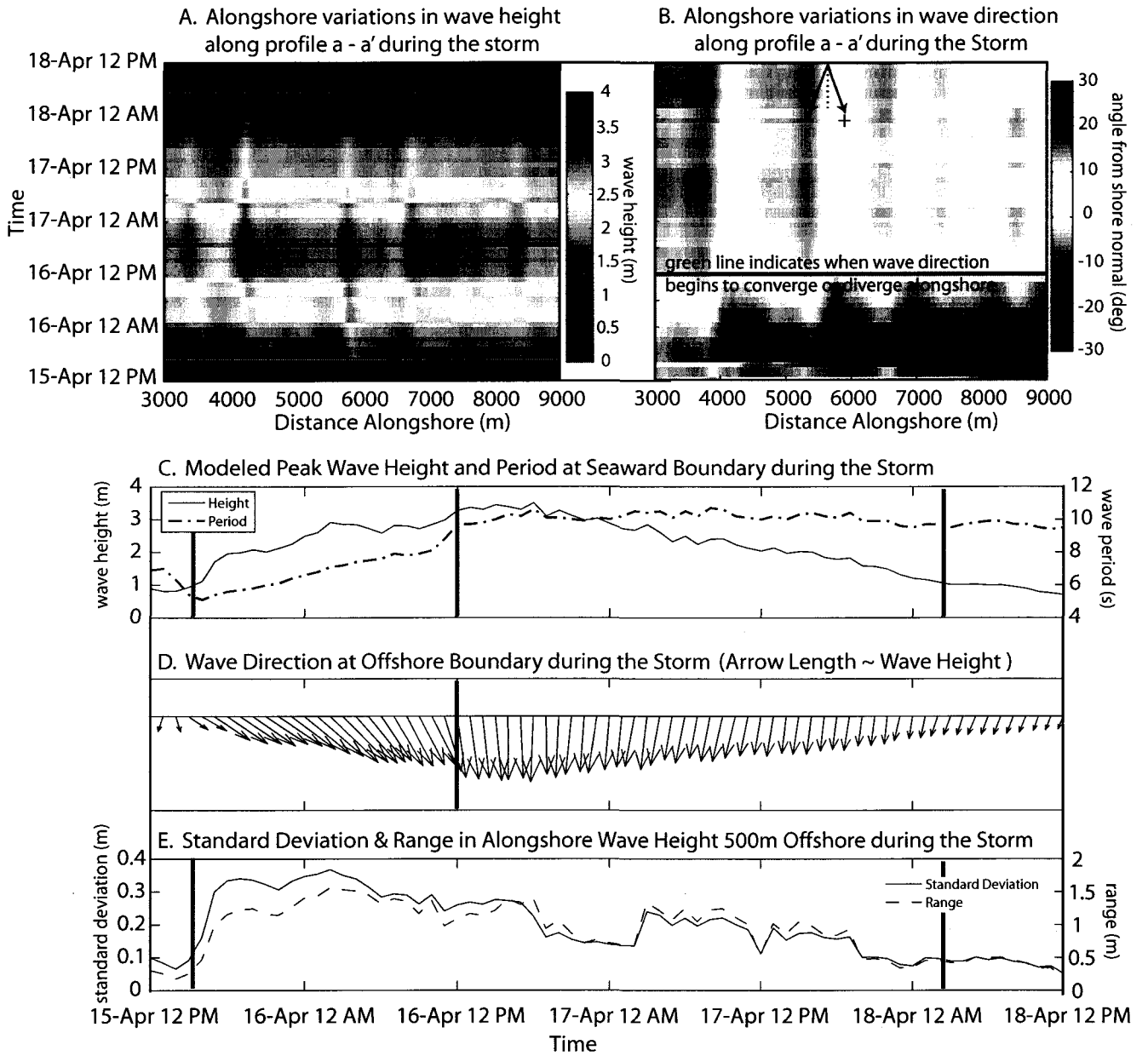


Figure 12

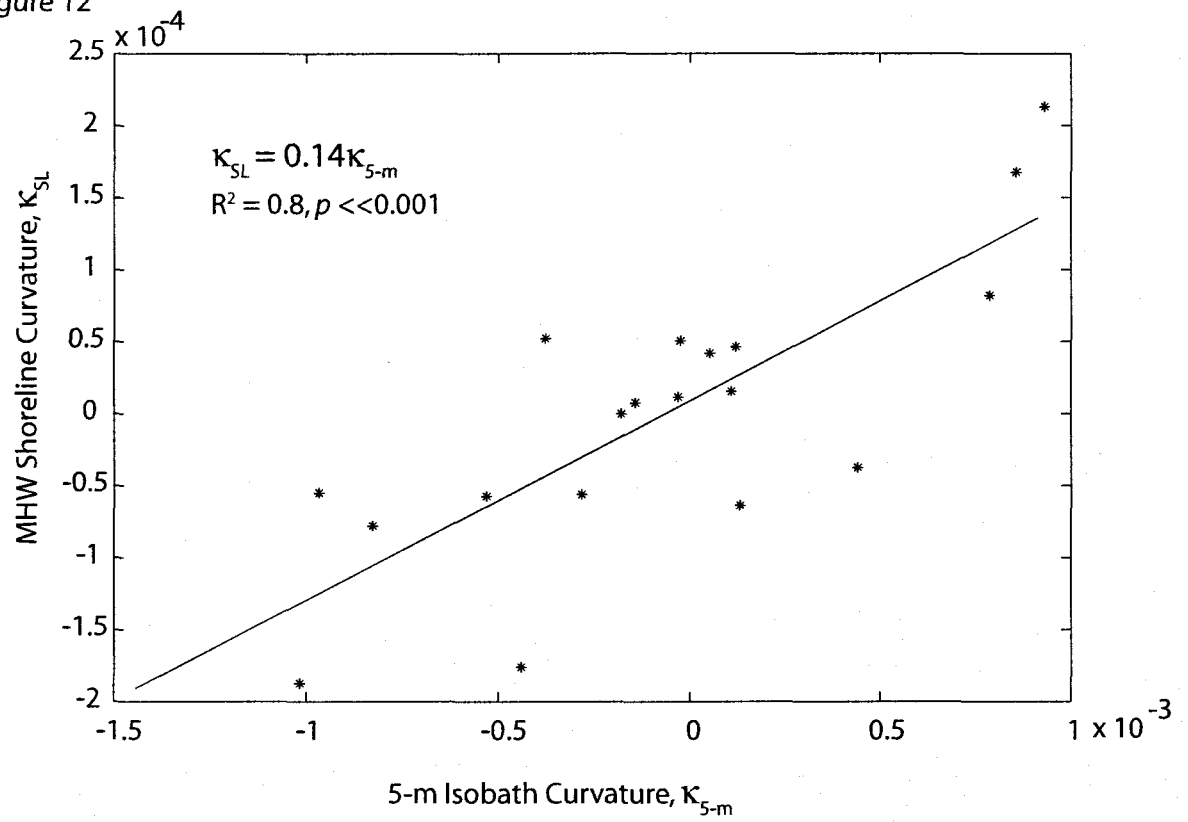


Figure 13

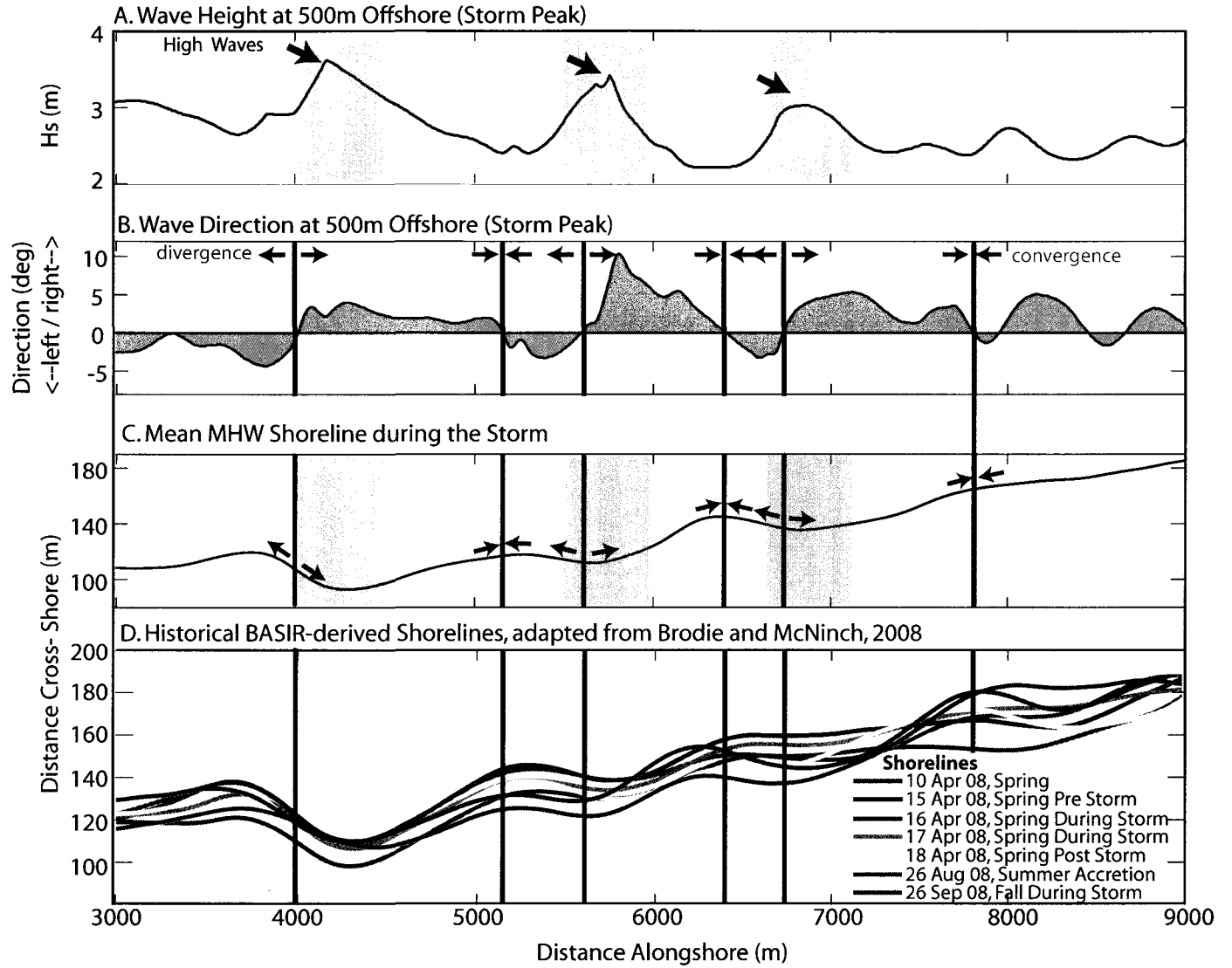
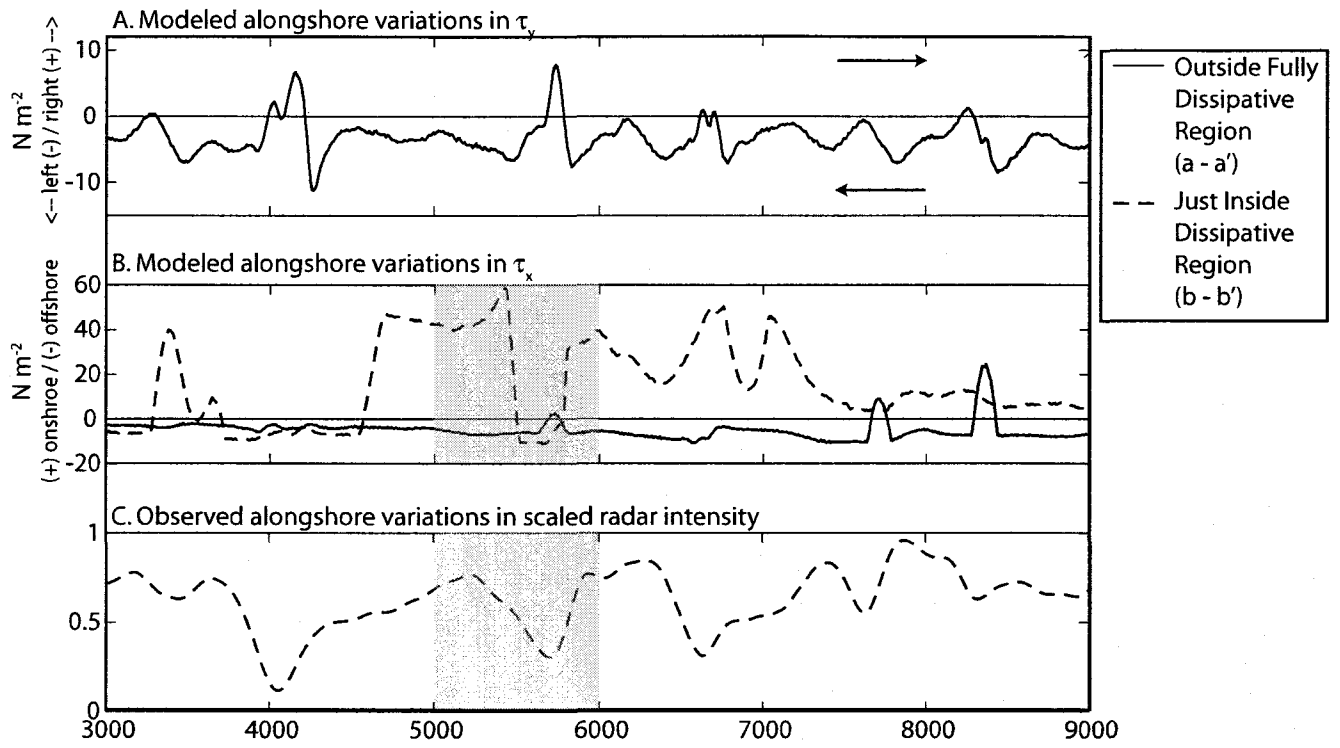


Figure 14



CHAPTER 3

Spatial and temporal patterns of beach change during storms:
relationships to runup maxima, mean water levels, inner surf-zone dissipation,
and breaking wave parameters.

Partial Manuscript Citation: Brodie, KL and McNinch, JE (*Submitted*). Beach change during a nor'easter: relationships to wave steepness and inner surf zone dissipation. *Coastal Sediments '11*.

ABSTRACT

Observations of spatial variations in beach response to storms are ubiquitous along the world's coastlines. Recent hypotheses that explain alongshore variations in beach change during storms include: variations in wave height alongshore, higher relative runup elevations compared to antecedent beach morphology, and decreased numbers of offshore sandbars. Unfortunately the difficulties associated with collecting littoral data during storms have prevented adequate tests of these hypotheses. In addition, anecdotal evidence suggests significant amounts of recovery may occur along beaches when waves are still large, suggesting that traditional methods of "pre-" and "post"-storm surveys may underestimate the total impact of storms on beaches. We observed 10 km of beach on the Outer Banks of North Carolina semi-daily during a Nor'Easter using CLARIS, and analyzed spatial and temporal patterns in both shoreline and beach-volume erosion and accretion with respect to modeled wave parameters and radar observed surf-zone morphology. In addition, we measured alongshore variations in observed wave runup maxima and compared them to predicted $R_{2\%}$ statistics using the Stockdon et al. [2006] equation. Data indicate that the timing of erosion and accretion during storms may be strongly influenced by wave steepness. More than half of the original shoreline erosion recovered along 50% of the study site within 24 hours of the storm peak as waves remained large (>2.5 m), but transitioned to long period swell. Spatial variations in beach volume change during the building portion of the storm were not explained by either alongshore variations in wave height or predicted relative runup. Instead, the configuration of the inner surf zone seemed to control spatial variability in beach volume change, with double-barred regions experiencing less erosion than single barred regions. Specifically, the amount of wave dissipation in the inner surf-zone, as measured using time-averages of X-band radar returns, explained 50% of the variability in beach volume change during the building portion of the storm. In addition, spatial and temporal patterns in the Iribarren number showed promise at predicting both alongshore and temporal variations in the direction and magnitude of cross-shore transport during the storm

1.0 INTRODUCTION:

Correct predictions of how beaches respond to storm events and evolve at seasonal to decadal time-scales are critical for the effective management of coastal resources, especially along heavily populated and dynamic barrier islands. Specifically, predictions of alongshore variations in both sediment loss from the beach and inundation during storms are crucial for increasing storm preparedness and for effectively managing development. Recent field studies have correlated regions that experience exacerbated or alongshore-variable shoreline change at both storm and decadal time scales with various geomorphic features, including: irregular nearshore sandbar configuration [Kannan et al., 2003a; McNinch, 2004], antecedent geology [Riggs et al., 1995; Thieler et al., 1995; Miselis and McNinch, 2006], rip-current related embayments [Thornton et al., 2007], or low dune or berm heights relative to extreme-storm water levels [Stockdon et al., 2007; Sallenger Jr, 2000]. Despite these observations, a physics-based explanation for alongshore-variable shoreline change is lacking. Attempts at numerically modeling the behavior of shoreline hotspots during storms are rare, and the quantitative data needed to ground-truth the predictions are even more rare. Here, we provide observations of beach volume and shoreline change from terrestrial lidar data collected semi-daily during a Nor'Easter on the Outer Banks of North Carolina. We then compare these changes with simultaneous observations of surf- and swash-zone morphology from X-band radar as well as modeled wave transformation during the storm to analyze patterns of erosion and accretion. The data suggest that spatial and temporal variations in beach-volume change during moderate storms are not well predicted using traditional erosion-based metrics such as wave height and relative runup. Instead, large-scale spatial variations in shoreline and beach-volume change seem to be dependent on wave dissipation and breaking type which reflects variations in inner surf zone morphology and wave steepness.

Visual observations of the beach during high-energy conditions and post-storm rack-lines have long suggested that maximum water levels during storms are often much higher than measured water levels in the surf-zone and can vary significantly alongshore. A growing body of literature suggests that comparing maximum and mean water levels reached during storms with variations in beach and dune morphology will therefore be a good predictor of areas of the coast that are particularly susceptible to coastal erosion and damage during extreme storms [Sallenger, 2000; Stockdon et al., 2007; Plant et al., 2010]. Specifically, these state of the art predictive models estimate maximum runup, defined as the highest elevation reached by oscillating swash over a given time-period, along a stretch of beach for a given storm condition and then classify the impact regime (swash, dune collision, overwash, inundation [see Sallenger, 2000]) based on the antecedent morphology [Stockdon et al., 2007]. While the storm-impact models perform better than random models (54% accuracy compared to 33%), there is clearly room for improvement [Stockdon et al., 2007]. Unfortunately, due to the difficulty of quantitatively measuring maximum runup over large spatial scales (10s of km), it is unclear whether the high error stems from poor predictions of maximum runup, out-dated antecedent beach morphology, or an overly simplified modeling approach—neither variations in longshore transport, the effects of irregular surf-zone morphology, nor the dynamic evolution of the beach morphology during the storm are included. Though these simplifying assumptions are certainly advantageous from a predictive standpoint, and perhaps less important during the most extreme events when complete inundation is likely, their effects on predictions still need to be quantified.

Efforts to numerically model erosional hotspots have been mostly confined to explaining decadal hotspots, and focus on the contribution of persistent convergence and

divergence patterns in longshore transport to shoreline change. The approaches have varied, ranging from one-line models (e.g. the CERC equation) that compare deep-water wave angle to shoreline morphology [e.g. Ashton et al., 2003] to Benedet and List [2007], who use Delft3D, a complex process-based model, to solve the full momentum equations and simulate wave transformation, nearshore currents, sediment transport, and ultimately morphology change onshore of a borrow pit. Explanations for hotspots at the storm-scale are lacking; but speculations abound. One thought is that storm-driven transport is dominated by cross-shore sediment exchange between the beach and inner-surf and swash-zones with alongshore-variable sandbar configurations modulating this response [Kannan et al., 2003; Lippmann et al., 2004]; however, previous attempts at testing this hypothesis were hindered by the difficulties of observing beaches and surf-zones during storms. Another thought is that irregular offshore bathymetry may focus wave energy during storms along different areas of the beach, leading to intensified erosion onshore of those regions [Schupp et al., 2006].

The objectives of this paper are to observe the evolution of the beach semi-daily during a storm, and analyze spatial and temporal patterns of erosion and accretion with respect to wave climate (e.g. breaking wave height and wave length), surf-zone morphology (e.g. # of offshore bars and dissipation patterns), and runup elevations. We test three hypotheses from the literature that attempt to explain alongshore patterns in erosion during storms: (1) that regions of elevated wave height caused by refraction over irregular nearshore bathymetry align with areas of increased erosion [e.g. Schupp et al., 2006]; (2) that regions with comparably higher storm runup elevations relative to beach morphological features experience heightened erosion [e.g. Sallenger et al., 2000]; and (3) that regions with single to no offshore sandbars experience more erosion during storms than regions with multiple offshore sandbars [Kannan et al., 2003]. We use

Coastal Lidar and Radar Imaging System (CLARIS) to record high-resolution beach topography from a terrestrial lidar scanner, and swash and surf-zone morphologies from X-band radar. CLARIS also provides elevations of runup alongshore during the storm, through the intersection of the most landward-observed swash excursion from the radar data with simultaneously collected beach topography data. In the following section we present background on runup, wave-breaking type, and cross-shore sediment transport, and then provide details of the observed storm and some brief background on the study site. We then discuss the methodology and present results of the shoreline and volume change analysis, runup observations and predictions, and surf-zone morphology. We conclude with a discussion of (1) the discrepancies between the observed and predicted runup elevations, and (2) the spatial and temporal patterns in beach volume change during the storm with respect to the three stated hypotheses, as well as wave steepness and the Iribarren number.

2.0 BACKGROUND

2.1 Maximum Runup

Maximum runup is the sum of astronomical tide, surge, wave-driven setup, and wave runup, and is thus an indicator of the elevation up to which swash zone processes, the principle mechanism for sediment transport between the beach and surf-zone [Masselink and Hughes, 1998], are active. Alongshore variations in maximum runup can be attributed to two of its main forcing components: wave-driven setup and runup. Wave-driven setup is the super-elevation of the mean water level due to cross-shore gradients in radiation stress induced by wave breaking [Longuet-Higgins and Stewart,

1964], and is often measured at the shoreline by meaning the elevation of the swash over a given time-period [e.g. Stockdon et al., 2006]. Wave runup is the time-varying elevation of the most shoreward swash excursion on the foreshore, with maximum runup often defined as the 2% exceedence elevation of runup over a given time period [e.g. Holman, 1986; Stockdon et al., 2006]. Alongshore variations in runup and setup may be forced by alongshore variations in foreshore slope, surf-zone morphology, wave parameters (e.g. height or wavelength), foreshore grain-size, and infragravity energy.

Relationships between runup or setup and these variables have been the focus of many studies, and the relationships found often varied depending on the type of beach studied [e.g. Guza and Thornton, 1981; Holman and Sallenger, 1985; Nielsen and Hanslow, 1991; Hanslow and Nielsen, 1993; Raubenheimer and Guza, 1996; Ruessink et al., 1998; Ruggiero and Holman, 2004]. Stockdon et al. [2006] provide a good review of the aforementioned relationships and propose a new empirical relationship between the 2% exceedence elevation of runup (R_2) and foreshore beach slope (β_f), local wave height (e.g. 10-m water depth) reverse-shoaled to its deepwater equivalent (H_0), and deep-water wavelength (L_0):

$$R_2 = 1.1 \left\{ 0.35 \beta_f (H_0 L_0)^{\frac{1}{2}} + \frac{[H_0 L_0 (0.563 \beta_f^2 + 0.004)]^{\frac{1}{2}}}{2} \right\} \quad (1)$$

The above relationship had a root-mean-squared-error of 32 cm and is suggested for use on all beaches, except under extremely dissipative conditions when frictional dissipation of waves may be an important term in the momentum equation. While the

parameterization (Eq. 1) is based on three main variables, Stockdon et al. [2006, 2007] found that the majority of variability in maximum runup is often attributable to foreshore slope. Although only a few spatial data sets were available to test the above equation, preliminary findings suggest that significant variation in runup existed that was not well predicted by the above model when beach morphology was highly alongshore variable, [Stockdon et al., 2006]. Stockdon et al.'s preliminary results, in combination with the weak performance of the storm impact models during lower impact regimes (e.g. swash and dune-collision), demonstrate the need for spatially extensive observations of runup.

Large-scale spatial observations of runup are difficult to ascertain using traditional methods of measuring water level at the shoreline, such as resistance wires or pressure sensors [e.g. Guza and Thornton, 1982]. Consequentially, studies have been limited to collecting data in time at a single location. Newer, video-based estimations of runup [Holman and Sallenger, 1985; Guza and Thornton, 1982; Holman and Guza, 1984; Aagaard and Holm, 1989; Holland et al., 1995] allow for an expansion of observations into the spatial domain [Ruggiero et al., 2004, Ruessink 1998, Stockdon et al., 2006]. The video-estimates of runup compare well with very near-bed wire or sensor measurements, but are more sensitive to thin tongues of foamy runup and therefore often have higher means, variance, and maxima than the wire measurements [Holland et al., 1995]. While video observations from fixed towers increase spatial observations up to the kilometer scale, measurements on the order of tens of kilometers are still difficult due to the limited view-field of fixed cameras. McNinch [2007] showed that X-band radar-derived swash measurements compare well with video-derived swash, suggesting that mobile radar could be used to map swash excursions over large distances alongshore.

2.2 Wave Breaking in the Surf-Zone

Wave breaking is the dominant energy input to the coastal system and a driving force in suspension of sediment and its subsequent transport. After traversing the open ocean and transforming over nearshore bathymetry, waves break in the surf zone when the velocity of the water particles in the wave crest exceeds the velocity of the wave itself [Iversen, 1952]. The form of wave breaking—spilling, plunging, or surging—is thought to depend on both the slope (β) of the beach (or surf-zone) and the steepness of incoming waves [Galvin, 1968], often parameterized by the non-dimensional Iribarren number [Battjes, 1974]:

$$\xi_{\infty} = \frac{\beta}{\sqrt{\frac{H_{\infty}}{L_{\infty}}}} \quad (2)$$

where H is wave height, L is wavelength, and ∞ indicates their deepwater values. Spilling breakers are more likely to occur at low Iribarren numbers when wave steepness is high (large, short-period waves) and beach slope is flatter, whereas plunging breakers are more likely to occur at higher Iribarren numbers when wave steepness is low (long-period waves) and beach slope is steeper. Though threshold values have been defined in the laboratory (spilling occurs when $\xi_{\infty} < 0.5$; plunging occurs when $0.5 < \xi_{\infty} < 3.3$) by Galvin [1968] and Battjes [1974], field measurements are rare and reveal more scattered results [Weishar and Byrne, 1978]. Field observations are often complicated by the fact that the wave field is not monochromatic and that beach slope can vary alongshore, allowing multiple forms of wave breaking to occur along the same stretch of beach at the same time.

Depending upon the type of breakers, wave energy is dissipated differently in the surf zone, and turbulence transferred to the bed at different rates. Beach and Sternberg [1996]

note that plunging breakers have a higher breaking wave height (H_b) to water depth (h) ratio across the surf-zone than spilling breakers or bores, and Wang et al., [2002] measure a greater rate of wave-height decay following plunging breaking vs. spilling breaking. In addition, large variations in the amount and vertical distribution of suspended sediment under spilling and plunging waves has been observed [Beach and Sternberg, 1994; Kana, 1979; Nielsen, 1984]; with jets of turbulence during plunging breakers reaching all the way through the bottom boundary layer and suspending large amounts of sediment near the bed [Voulgaris and Collins, 2000]. In addition, Wang et al. [2002] find that longshore transport rates are significantly higher under plunging breakers than spilling breakers for a similar wave height, particularly in the inner-surf and swash zone.

2.3 Cross-Shore Sediment Transport

There is some speculation that the rapid erosion and accretion characteristic of storm-scale shoreline hotspots can be explained by cross-shore sediment exchange between the beach and inner surf zone [see List et al., 2003; List et al., 2006], and thus an understanding of the processes controlling sediment transport in the swash and inner surf zone is key. Many studies have focused on predicting the direction of cross-shore sediment transport in the outer surf-zone [e.g. Birkemeier, 1984; Sallenger et al., 1985; Roelvink and Brøker, 1993; Thornton et al., 1996; Gallagher et al., 1998; Elgar et al., 2001; Plant et al., 2001; Ruessink et al., 2007], and on- and offshore sandbar migration is explained by variations in the importance of unsteady wave forcing (e.g. velocity skewness and wave asymmetry [Thornton et al., 1996; Elgar et al., 2001; Ruessink et al., 2007; Roelvink and Stive, 1989; Hoefel and Elgar, 2003]) and mean flows (e.g. offshore directed undertow [Thornton et al., 1996; Gallagher et al., 1998]), respectively. More

poorly understood is the direction of net sediment transport in response to changing wave conditions in the inner-surf and swash zones, where breaking-wave and bore-induced turbulence may penetrate down to the bed [see extensive review by Masselink and Puleo, 2006].

Sediment transport is usually predicted using shear stresses induced by turbulence created in the bottom boundary layer [Nielsen, 1992]. In the inner-surf zone, however, where water depth is shallow compared to the height of waves or bores, turbulence may be introduced by the breaking part of a bore, particularly during bore collapse and the initiation of swash uprush [Voulgaris and Collins, 2000; Jackson et al., 2004; Hsu and Raubenheimer, 2006]. The slope of the beachface at the bottom of the foreshore controls the type of breaker or bore, and thus the amount of turbulence advected into the swash zone, and resulting suspended sediment profile [Masselink and Puleo, 2006]. The slope of the beachface also influences the speed of swash downrush, and thus can effect interactions between the down-rushing swash and incoming bores, and ultimately sediment transport patterns [Holland and Puleo; Butt and Russell, 2005; Masselink et al., 2009]. Extreme swash downrushes at infragravity frequencies can collide with incoming bores, causing the bores to become almost stationary and create a hydraulic jump [Butt and Russel, 2005] that enhances offshore transport, particularly if no collision occurs with the next uprush. During storms, as infragravity energy becomes dominant in swash zones, increased occurrences of hydraulic jumps and increasing wave period relative to swash duration, both may contribute to heightened offshore transport [Holland and Puleo, 2001; Butt and Russel, 2005]. Thus, modeling or predicting the direction of transport at the shoreline may require resolving individual swash “events” [e.g. Masselink et al.,

2009; Holland and Puleo, 2001], or knowing characteristics of the waves and beach slope at the shoreline (as opposed to offshore or at the edge of the surf-zone).

3.0 STUDY AREA

3.1 Field Site

Despite the linear morphology of the northern Outer Banks of North Carolina and the relatively featureless, planar continental shelf, significant alongshore variation in beach response to Nor'easters and Hurricanes is often observed. Along a 40 km section of coastline from Nags Head north to Duck, for example, there are regions that can be classified as decadal accretional and erosional hotspots, reversing-storm hotspots, or merely as static over both long and short time scales [List et al., 2006; McNinch, 2004; Fenster and Dolan, 1993]. The section of coastline studied here spans ~10 km in Kitty Hawk and Kill Devil Hills and has been previously observed to experience both heightened and alongshore-variable erosion at the short-term storm scale [Miselis, 2007; Schupp et al., 2006; McNinch, 2004; List et al., 2006].

A portion of the 10-km study site is known as the Kitty Hawk erosional hotspot, due to its high decadal shoreline change rate of -2 m yr^{-1} [Benton et al., 1997], and has been extensively surveyed over the past decade with a suite of geophysical tools including: interferometric swath bathymetry surveys, Chirp sub-bottom seismic surveys, side-scan sonar surveys, vibracores, RTK GPS beach topography surveys, and mobile X-band radar (see McNinch and Miselis [2009] for a good review). These field efforts have revealed that offshore of the erosional hotspot, a series of geologically controlled shore-oblique trending sand bars and troughs exist that are underlain by the paleo-Roanoke River channel [Miselis 2007; Browder and McNinch, 2006; McNinch, 2004]. The beach and nearshore sediment is

both horizontally and vertically heterogeneous [Miselis, 2007], with coarse gravel, presumably derived from old fluvial infill, exposed in the bottom of the nearshore troughs [Schupp et al., 2006] as well as exposed in patches on the beach [Miselis, 2007]. The shore-oblique bars and troughs have been observed to persist during Nor'easters [Brodie and McNinch, *In Review*; Chapter 2, this Dissertation] and are also present in pre- and post-Hurricane Isabel (storm of record for this region) swath bathymetry surveys [Miselis, 2007]. In addition to persistent three-dimensional nearshore bathymetry, the study site is also characterized by three-dimensional shoreline morphology: a series of kilometer-scale megacusps and embayments mimic the nearshore bathymetry in the region and also persist during storms [Brodie and McNinch, *In Review*; Chapter 2 this Dissertation]. The persistent shoreline morphology is likely the result of self organizing behavior forced by wave transformation over the persistent nearshore bathymetry [Brodie and McNinch, *In Review*; Chapter 2, this Dissertation].

In contrast, the northern 3-km of the study site has a more classic, convex shoreface with straight, shore-parallel depth contours, and a relatively steeper, narrower, beach [Brodie and McNinch, *In Review*; Chapter 2, this Dissertation]. Visual observations of the beach suggest that runup during storms frequently inundates houses along these 3 km of coastline, as no protective dune remains in front of the houses.

3.2 Storm Event

Extratropical storms in the fall and winter, colloquially known as Nor'easters, are the most common storm along the Outer Banks of North Carolina. While hurricanes can hit the area in the summer months, studies suggest that the majority of morphological change occurs in response to successive groups of Nor'easters [Lee et al., 1998;

Birkemeier et al., 1999]. Though the effects of a Nor'easter aren't usually as catastrophic as extreme hurricanes, the storms often cause overwash and frequent dune erosion and damage to houses that are nearest the ocean. They are significant events as far as homeowners and coastal managers are concerned, and have been observed to cause up to 30 m of shoreline change during a single storm [List et al., 2006]. In this study, we document the response of the beach to a Nor'easter in April 2009 every 12 hours (Figure 1A) using CLARIS.

The surveyed Nor'easter occurred from 15 April 2009 to 18 April 2009 and resulted in waves in 8 m water depth that were > 2 m for ~ 37 hours, as recorded by the 8 m Array at the U.S. Army Corps of Engineer's Field Research Facility (FRF) in Duck, NC, located approximately 10 km north of the study site. Waves peaked on 16 April 2009 with 3.4 m high waves in 8 m of water depth, with breaking observed out to at least 6 m of water depth (unpublished data, Hanson 2009). Wave steepness was high during the building period of the storm, and decreased systematically throughout the storm (Figure 1A-B). Waves were high angle at the beginning of the storm, becoming more shore-normal just before the peak of the storm at noon on the 16th (Figure 1C). Surge peaked before the wave height on the morning of the 16th (Figure 1D). Winds were strong and onshore throughout the building part of the storm, decreasing dramatically after the peak of the storm, and switching to light offshore winds by midday on the 17th. Peak surge coincided with peak wind speed (Figure 1E).

This storm exemplifies a typical Nor'easter on the Outer Banks, with most of the erosion confined to the beach and base of the dune. While overwash deposits were noted in some locations along the northern portion of the study site, our runup elevations do not reflect this as surveys were conducted in the two hour window centered at low tide to

maximize beach width for driving and ensure relatively constant water level during the survey.

3.3 Reference Line

All data were transformed to a local alongshore/cross-shore reference coordinate system based on a reference line that begins at (905,296.743 m NC State Plane Easting, 266,063.982 m NC State Plane Northing) and trends ~150 degrees true north along the general angle of the coastline (Figure 1.0). Alongshore coordinates increase to the southeast, and cross-shore coordinates increase in the offshore direction. The reference coordinate system allows for easy analysis of alongshore and cross-shore trends, alignments, and distances between features, and aids in bringing out any three-dimensional features that often have small cross-shore amplitude to alongshore wavelength ratios. Please note that herein, “*distance alongshore*” refers to distance along the reference line, and “*distance cross-shore*” refers to distance along perpendicular lines to the reference line, not along perpendicular lines to the local shoreline orientation.

4.0 METHODS

4.1 CLARIS: Coastal Lidar and Radar Imaging System

CLARIS is a new, mobile, coastal surveying tool that enables simultaneous collection of radar data of the nearshore and topography data of the beach and dune from a terrestrial laser scanner (see Chapter 1). The methodology and applications of radar to coastal surveying are similar to that of video [Lippmann and Holman, 1989], as the foamy rough surface of breaking waves and swash cause high-intensity radar returns [Bell, 1999; Ruessink et al., 2002; Haller and Lyzenga, 2003; McNinch, 2007]. As such,

radar data can be used to infer bathymetry (Bell, 1999; Brodie and McNinch, *In Review*) as well as map swash and sandbar morphology (Ruessink et al., 2002; McNinch, 2007). In this paper, the radar data is used to record time-series of swash excursions along the beach in order to extract the position of the maximum-observed swash excursion during each survey. In addition, radar morphology mosaics and inferred bathymetry are used to extract important environmental parameters on inner and outer surf-zone morphology. Topography data is collected with a Riegl 3D Terrestrial Laser Scanner (Riegl VZ-390i) which scans to starboard of the vehicle during transit between radar stops. Terrestrial laser scanner data will be referred to as “lidar data” throughout the remainder of this paper. Survey precision is 1.3 cm and accuracy is +/- 10 cm. Point-cloud density is ~30 to 40 points per m², with higher density in the cross-shore direction. Unfortunately, the lidar survey from the evening of 16 April 2009 (Figure 1A) has been discarded in this analysis due to poor RTK-GPS quality. Topography data is used in this paper to extract the elevation associated with the maximum swash excursion, as well as to measure foreshore slope, shoreline change, and volume change during the storm.

4.1.1 Maximum Swash Excursion Observations

The position of maximum swash excursion is objectively picked based on cross-shore profiles of averaged radar intensity, as described in Brodie and McNinch, *In Review* (Chapter 1, this Dissertation). This position is then intersected with the lidar topography data and elevations extracted every 3 m alongshore. It is important to note that because the surveys are collected at low-tide and not high-tide, the elevation associated with the maximum swash excursion presented here merely represents maximum excursions during the time of the survey, and not the absolute maximum water level reached during the tidal

cycle. In addition, observed runup maxima ($R_{max-obs}$) only represent 12-minutes of data, as opposed to the 17 to 120 minutes used in Stockdon et al. [2006] to calculate $R_{2\%}$, a statistical representation of maximum runup, and thus have the potential to be somewhat lower than predicted runup maxima.

4.1.2 Foreshore Slope, Shoreline, and Volume Extraction

Foreshore slope is estimated from the lidar data every meter alongshore by fitting a linear regression line to data between a meter above the observed maximum swash elevation and the offshore edge of the observed lidar profile. In circumstances where the number of data points in this segment is less than 4 (only 12% of the time), the linear regression line is fit to the bottom half of the observed lidar profile.

Upper beach volume is calculated every 1m alongshore by extracting the area under the lidar profile between the base of the dune and the mean high water (MHW) contour. Though the surveys are conducted at low tide and mean water level is less than MHW for all of the surveys (Figure 1D), occasionally the lidar profile does not extend down to the MHW contour due to wave runup and setup processes. During these times (the 15PM and 16AM surveys), the end of lidar profile is extrapolated down to the MHW contour using the best-fit foreshore slope extracted by the above method. In addition, we chose to only calculate change in upper-beach volume (i.e. not including the dune), as sand-fences and house porches often prevented accurate determination of the face and crest of the dune along the study site. The MHW contour is then used to compute shoreline change during the storm. Though portions of the MHW contour represent extrapolated data, the trends are similar to that of the 1.5 m contour (the lowest contour observed in all surveys), and the extrapolation method is similar to the widely cited List

et al. [2006] study of shoreline change. The ability to calculate volume change at 1-m intervals along beaches during storms is a marked improvement over volume change calculations from interpolated profiles, and more rigorously assess the storm's impact on the beach when compared with traditional shoreline change methods.

4.1.3 Radar Morphology Mosaics

Averaging radar returns through time produces images that show persistent patterns of wave breaking in the nearshore, similar to time-lapsed video images [e.g. Lippmann and Holman, 1989; Ruessink et al., 2002; McNinch, 2007]. Intensity of the time-averaged radar returns (in this case normalized on a scale from 0 to 1) can then be used as a proxy for dissipation. From these dissipation patterns, morphology of the surf and swash-zone can be inferred [McNinch, 2007; Brodie and McNinch, *In Review*; Chapter 1, this Dissertation]. Information from multiple locations alongshore can be mosaicked together to create a "morphology mosaic", from which important morphology metrics are extracted. Specifically, we are concerned with the number of peaks in dissipation seaward of the valley of the beach, as this is a proxy for the number of offshore sandbars, as well as the width of the inner and outer surf-zones. The width of the inner surf zone is defined here as the distance between the maximum observed swash excursion and the offshore edge of the inner bar or swash zone (in the case of a welded inner bar), whichever is farthest seaward. Namely, the inner surf zone here describes the morphology of the surf and swash zones inside of the outermost shore parallel bar. The width of the outer surf-zone is defined here as the distance between the 5-m isobath, used as a proxy for the offshore base of the outer bar (see Chapter 2, this Dissertation for an in

depth discussion of this metric), and the offshore edge of the inner surf zone as defined above. These parameters are then used in the analysis of alongshore variations in shoreline change.

4.2 STWAVE-FP Modeled Wave Parameters

In chapter 2, the steady-state spectral wave model full-plane version (STWAVE-FP) is first assessed at the FRF in Duck, NC for the studied storm and then used to model wave transformation during the storm at the field site. In this paper, significant wave height and peak period is extracted along the 5 and 10-m contours (approximate edge of the surf zone) hourly, every 10-m alongshore. In order to calculate appropriate values of the Iribarren number (Eq. 2), wave height is linearly reverse shoaled to its deepwater equivalent assuming no wave refraction, similar to Stockdon et al. [2006]. Peak wave period (T_p) is converted to deepwater wavelength (L_∞) using the deep water approximation of the linear dispersion equation. Wave parameters are available at every 10-m alongshore throughout the study site and every hour during the storm.

4.3 Stockdon et al. [2006] Runup Model

STWAVE-FP modeled wave parameters and observed foreshore slope are used to force Eq. 1 during the storm. Specifically, the modeled wave parameters are converted to their deepwater equivalents, per Stockdon et al. [2006], by linearly reverse-shoaling them, assuming no wave refraction. In order to obtain estimates of foreshore slope hourly during the storm, foreshore slope is linearly interpolated between survey times at each location alongshore (Figure X). The wave-driven component of $R_{2\%}$ is then

computed from these variables every hour during the storm according to Eq. 1. The model is run a total of three times, once using wave parameters extracted at the 5-m contour and reverse shoaled (model run 1), once using wave parameters extracted at the 10-m contour and reverse shoaled (model run 2), and a final time using the 10-m reverse-shoaled wave parameters and only the initial foreshore slope (model run 3). The different model runs were chosen to test the errors introduced by using static slope conditions, as well as to test whether accounting for wave refraction over the highly complex bathymetry at this location improved predictions.

The Iribarren number is used to identify locations and times when the wave conditions and foreshore slope are such that the dissipative form of Eq. 1 should be used (i.e. when $\xi_{\infty} < 0.3$, according to Stockdon et al. [2006]). To add in background water levels, thereby converting the $R_{2\%}$ predictions to a datum, the water level data recorded at the FRF pier (Figure 1D) are added to the predictions. To find the equivalent cross-shore position of this predicted runup, the predicted elevation is intersected with the lidar data from the 5 surveys. Predicted elevations and waterline positions at the time of the CLARIS surveys are then compared with observations.

5.0 RESULTS

5.1 Shoreline and Volume Change during the Storm

Despite the persistence of shoreline megacusp and embayment morphology during the storm (Figure 2A), significant spatial and temporal variability in shoreline change is observed (Figure 2B). Shoreline change is calculated between each survey time pair (Figure 2B), termed “inter-survey change”, and also between the pre-storm

15PM survey and end-storm 18AM survey, termed “net change” (Figure 2C, red line). In addition, shoreline change is calculated for the recovery period in the 10-days after the storm, termed “recovery”. During the first 12 hours of the storm, as waves increase in height and period, 78% of the study site experiences erosion (magenta line, Figure 2B). Erosion is greatest between ~5000 and 8000 m alongshore, with a smaller area of erosion in the northern portion of the study site at ~2000 m alongshore. No clear relationship is observed between shoreline erosion and shoreline morphology (e.g. megacusps, denoted by the blue shaded regions in Figure 2). During the next 24 hours (16AM to 17AM Survey) as waves peak and begin to fall and wave period levels off at around 12 s, 72% of the region experiences accretion (yellow line, Figure 2B), with 50% or higher of the shoreline erosion recovered along more than half the study site. Recovery continues in smaller amounts along 70% of the study site during the remaining portion of the storm (cyan and purple lines, Figure 2B).

Overall net shoreline change (red line, Figure 2C) suggests the Nor’Easter is an erosive event, as 63% of the region is erosive, 28% accretive, and the remaining 9% shows no significant change. Note that while 78% of the region experienced erosion during the first 12 hours of the storm only 63% of the region experienced net erosion over the entire storm due to the significant accretion in the 12 hours following the storm peak (see discrepancy between magenta line in figure 2B and red line in 2C at around 7000 m alongshore, for example). Ten days after the storm, shoreline recovery appears to mirror the storm-driven erosion (green line, Figure 2C), similar to the observations of List et al. [2006].

In Figure 2D and E, upper beach volume changes are plotted in a similar manner to shoreline change, with inter-survey changes plotted in Figure 2D, and net and recovery volume changes plotted in Figure 2E. Upper beach volume change during the storm shows similar patterns to shoreline change, with almost all of the volume loss occurring during the first 12 hours of the storm (magenta line, Figure 2D), when mean water levels reached their peak (Figure 1D). Fifty percent of the region experiences significant volume loss during this time (magenta line, Figure 2D); however, only 16% of the region (mostly confined to the two southern most embayments at 7000 and 8500 m alongshore) experiences volume gain on the upper beach during the following 24 hours (yellow line, Figure 2D). No significant volume change on the upper beach is observed during the waning portion of the storm (cyan and purple lines, Figure 2D). Net volume change during the storm indicates a loss along 31% of the study site (red line, Figure 2E), with 16% of the study site still experiencing net volume loss 10 days later (Figure 2F). Thus, while volume gains in the 10 days post-storm mirror the patterns of volume loss during the storm (Figure 2E), the magnitude of recovery is less along some portions of the study site (Figure 2F).

5.2 Foreshore Slope Change during the Storm

Timestacks of alongshore variations in foreshore slope (magnitude denoted by the colors) during the storm are shown in Figure 3. During the first 12 hours of the storm, foreshore slope steepens (cool colors changing to warm colors) by more than a half degree along 56% of the study site, flattens along 12% of the study site, and remains within a half degree of its initial slope along 32% of the study site. During the next 24

hours (16AM to 17AM survey) 40% of the study site flattens, 16% steepens, and 44% remains within a half degree of its slope just before the peak of the storm (16AM survey). Between the 17AM and 17PM survey, slopes in 50% of the region remain the same, 29% flatten, and 19% steepen. Percentages are similar between the 17PM and 18AM survey. Slope varies by as much as 6 degrees in the embayment centered at 7000 m alongshore, and up to 5 degrees in both the embayment at 5800 m alongshore and the megacusp at 3800 m alongshore. A net flattening during the storm is only observed in the embayment at 7000 m, with steepening or no significant change observed elsewhere.

5.3 Runup Observations and Predictions

Observed maximum runup ($R_{max-obs}$) is plotted for each survey in Figure 4, with our overall observed maximum elevations during the storm connected by the black line. $R_{max-obs}$ varies by as much as 3-m over the course of the storm, ranging alongshore by as much as 2 m during a given survey (Figure 4). Maximum observed runup for the entire storm is highest between 1000 and 4000m and 8000 to 9000 m alongshore, and occurs during the 17AM survey along most of the study site. Observed runup appears to be consistently lower between ~5000m and 8000m alongshore for all surveys.

A comparison between $R_{max-obs}$ and predicted $R_{2\%}$ by the Stockdon et al. [2006] model (Eq. 1) for each survey is shown in Figure 5. While both $R_{2\%}$ and $R_{max-obs}$ vary significantly alongshore, predicted $R_{2\%}$ shows considerably less variance during the 15PM and 18AM surveys when compared with the observed elevations, and is significantly underestimated during the 15PM survey (Figure 5A). In addition, though coherent spatial patterns are apparent in the predicted runup elevations, they appear to be

out of phase with the spatial patterns in the observed data (see, for example, comparisons with the 16AM survey in Figure 5B). Predicted $R_{2\%}$ shows better agreement in the steep northern section of the study site (between 1000 and 3000 m alongshore), but is consistently too low in the southern 1000 m of the study site. Predicted and observed magnitudes are similar between 5000 and 8000 m alongshore; however, spatial undulations are not correlated. For all surveys, model run 1 (5-m wave parameters, evolving slope) shows better qualitative agreement with observations.

Root-mean-squared error (RMSE) and bias for the three different model predictions are shown in Table 1. Scatter plots of each model run versus observed data can be found in Appendix A. No significant relationships between predicted and observed data for the individual surveys are observed. With the exception of model run 1 (5-m wave parameters, evolving slope) during the 17PM survey, all three model predictions have significant negative biases for all of the surveys, with the extreme occurring during the pre-storm 15PM survey. RMSE is highest for model run 3 (10-m wave parameters, static slope), the most commonly used form of the Stockdon et al [2006] equation, and lowest for model run 1 (5-m wave parameters, evolving slope), though all are higher than Stockdon et al [2006]'s overall RMSE of 0.38 m. The overall mean bias of -0.24 m of model run 1 is similar in magnitude to Stockdon et al. [2006]'s mean bias of -0.17 m. A point-by-point comparison of model run 1 predicted $R_{2\%}$ elevations with observed data for all the surveys is shown in Figure 6. The squared correlation indicates a positive relationship between predictions and observations, but that predictions explain only 16% of the variability of the data.

Since maximum inundation position is usually of more importance to homeowners along the coastline than elevation, the predicted maximum runup elevations from model run 1 (the closest to observed) are converted to swash excursion distances and compared with the radar-observed position of the maximum swash inundation for each survey in Figure 7A-E. The predicted maximum runup elevation during the 15PM survey is so low that swash excursion position could not be calculated along 80% of the field site, as the lidar data did not extend low enough (the seaward edge of the lidar data is equivalent to the instantaneous most landward edge of the swash at the time of each lidar shot, and thus should be significantly less than maximum runup the majority of the time). The highest swash excursion differences occur in the southern most portion of the study site where a storm-persistent, pronounced cusp field extends across the beach from the 3 m contour down to the waterline (visible as high frequency undulations in the colors between 8000 m and 9000 m alongshore in Figure 7A-E). A second, storm-persistent beach cusp field is also present from 2500 to ~4000 m alongshore, but it is confined more to the upper beach, and swash excursion errors are not as high.

Timestacks of predicted runup elevations from model run 1 at every location alongshore for the entire storm, are plotted in Figure 8, with colors indicating elevations. Black horizontal lines indicate survey times. Low frequency, tidal-forced water level fluctuations are visible as the alongshore-persistent bands of alternating cooler and warmer colors (note bands of cooler colors are centered near the solid black lines, indicating the survey took place at low tide). Maximum predicted runup elevations over the course of the storm (stars) occur near the storm peak, which happens to coincide with high tide (but not the highest high tide, see Figure 1D). To classify the storm impact

regime based on the Sallenger [2000] scale, maximum predicted runup elevations are compared with the elevation at the base of the dune from the 15PM (pre-storm) survey. If runup elevation < dune base elevation (magenta stars, Figure 8), the impact regime is classified as swash, whereas if the runup elevation is > dune base elevation (white stars, Figure 8), the impact regime is classified as collision. The runup model predicted the storm impact to be mostly in the swash regime (runup confined to the upper beach), with a few occurrences of collision (runup colliding with the base of the dune) in the northern portion of the study site and in the embayments centered at 5500 and 7000 m alongshore. Field observations of storm damage to houses and “overwash” deposits in the northern end of the study site support the model predictions. It is important to note that there is no dune in the northern portion of the study-site, and the extracted dune base elevation actually corresponds to the elevation at the base of houses along the shoreline. Thus, when the model predicts “collision” in the northern portion of the study site, the runup is most likely colliding with house pilings or “under-washing” beneath the houses, and depositing the observed “overwash” onto NC Route 12. Unfortunately, elevations behind the first line of houses are not scanned in this study, and therefore we cannot quantitatively confirm the presence of overwash, though qualitative observations support the prediction. In contrast, the collision regime predicted in the embayments at 5500 and 7000 m alongshore is not supported by either data (the lidar data shows no significant change in the position of the dune base) or qualitative field observations during the storm. Interestingly, the embayment at 7000 m alongshore did experience significant damage during Nor’Ida in November of 2009 (see <http://frf.usace.army.mil/vets/veterans.shtml>, for more information) with two houses collapsing.

5.4 Surf-Zone Morphology

The morphology of the surf-zone is characterized in Figure 9A and B through analysis of the radar morphology mosaic. The morphology is described in detail in Chapter 2, and thus is only briefly addressed here. An outer shore-parallel bar is present along the length of the study site that has persistent undulations where it is intersected by shore-oblique troughs, creating an alongshore variable outer surf-zone width (red line, Figure 9C). An inner bar is also present along the study site that welds to the shoreline between 5500 and 7500 m alongshore. This creates a variable number of peaks in dissipation seaward of the beach along the study site (green stars, Figure 9C), and thus variations in the width and characteristics of the inner surf-zone (blue line, Figure 9C). The variations between the two regions are exemplified in the field photos and example radar time series stacks and averages shown in Figure 10. In the northern end of the study site, three distinct zones in dissipation exist—the swash, inner bar, and outer bar (Figure 10A-C) where as in the welded inner bar region, only two peaks in dissipation are apparent (Figure 10D-F). The welded inner bar region is characterized by a wide, dissipative sub-aqueous foreshore traversed by dissipating bores (Figure 10D). In contrast, the double-barred region in the north is characterized by a narrower swash and steeper foreshore dominated by swash uprush and downrush as opposed to bore collapse (Figure 10A).

5.5 Hypothesis Tests of Alongshore Variable Change Metrics

To test the three hypotheses for alongshore variable erosion during the storm, we defined three metrics: wave height, relative runup, and the number of offshore peaks in

dissipation, and compared them to the volume change observed during the building portion of the storm, when the most erosion occurred. We did not use net volume change or during-storm inter-survey volume change, as all of the metrics are increased or decreased erosion metrics, and do not address the possibility of accretion. For hypotheses 1 and 2 we use cross-correlation analysis and linear regression analysis, reporting the correlation coefficient (R) and the squared correlation (r^2) respectively, whereas a student's t-test is used to test hypothesis 3. Significance levels are determined using p-values calculated with 15 degrees of freedom (d.F.). Effective degrees of freedom are determined by dividing the total number of samples (600) by the lag associated with initial autocorrelation decay of the beach volume change data (40).

To test hypothesis 1, that alongshore variations in wave height lead to alongshore variations in erosion, mean wave height at the 5-m contour during the building portion of the storm is compared with volume change (Figure 11A). Cross-correlation analysis yields an insignificant negative correlation coefficient ($R=-0.16$, $p=0.53$), and regression analysis indicates that wave height explains close to 0% ($r^2=0.02$) of the variability in the observed beach volume change (Figure 11B). Interestingly, though the overall correlation coefficient indicates an inverse relationship (regions of higher wave height correlate with regions of negative shoreline change), the two variables appear positively correlated between 5500 m and 7000 m alongshore.

To test the second hypothesis, that elevated maximum runup relative to beach morphology is a good predictor of alongshore variations in storm-induced erosion, relative runup, the ratio between predicted maximum $R_{2\%}$ (from model run 1) during the building portion of the storm and the elevation of the dune toe from the 15PM survey,

D_{10e} , is plotted with volume change in Figure 11C. We chose to use predicted $R_{2\%}$ as opposed to our observations of runup, in order to (1) reflect the true state-of-the-art application of the models, and (2) to prevent any biases from our sampling during low-tide. Though the dune crest is often used in this type of prediction for extreme storm events, we chose to use D_{10e} as our reference indicator, as the storm impact fell mostly in the swash or dune collision regimes. Higher ratios of $R_{2\%} / D_{10e}$ indicate that runup advances closer to the base of the dune than locations with lower ratios. That is, runup covers a significant portion of the upper beach when $R_{2\%} / D_{10e}$ is high. Hypothesis 2 proposes a negative correlation between $R_{2\%} / D_{10e}$ and volume change since high values of $R_{2\%} / D_{10e}$ are thought to indicate net erosion (large negative values of volume change). Cross-correlation analysis indicates a statistically insignificant negative correlation between $R_{2\%} / D_{10e}$ and beach volume change ($R=-0.29$, $p=0.26$). Squared correlation indicates that $R_{2\%} / D_{10e}$ explains only 8% of the variance in volume change during the building portion of the storm.

To test the third hypothesis, that regions with fewer offshore sandbars may experience heightened erosion, the number of offshore peaks in dissipation from the radar morphology mosaic is compared to volume change during the building portion of the storm (Figure 11E). Since the number of offshore bars is effectively a binary response, cross correlation analysis is not preformed. While chi-squared tests are often used to test significance of a categorical outcome, it is difficult to categorized storm response. An obvious category is erosion or accretion, however, hypotheses 3 merely associates the number of offshore bars with “more” or “less” erosion [Kannan et al., 2003], not erosion vs. accretion. Therefore, the volume change is split according to number of offshore

peaks in dissipation, and a student's t-test is performed to identify whether the two populations had significantly different mean volume changes. The t-test produced significant results ($p=0.01$, Figure 11F), indicating that the mean volume change for locations with only 2 offshore peaks in dissipation is significantly less than the mean volume change for locations with 3 offshore peaks in dissipation. While the number of offshore bars appears to be a good predictor of the general trend in beach erosion along the study site (e.g. heightened erosion between 5500 and 7500 m alongshore), it cannot describe the smaller-scale fluctuations or differentiate between "less erosion" and accretion.

5.6 Wave Steepness and Iribarren Number during the storm

Spatial and temporal patterns of breaking wave steepness are also investigated in relation to beach volume change between the surveys. Modeled 5-m wave parameters are used to calculate mean wave steepness for every location alongshore between each survey pair, and are plotted against inter-survey beach volume change in Figure 12. A general pattern is observed between wave steepness and volume change such that erosion occurs at high wave steepness values, accretion at moderate wave steepness, and no significant change when waves have moderate to low steepness (Figure 12A). Specifically, wave steepness is greater than 0.038 for 95% of the erosive data (Figure 12B). During times of no significant change, 93% of the data is < 0.038 , with a 5% exceedence value of 0.039 (Figure 12C). The accretive data also has a similar 95% exceedence value of 0.038, and is skewed towards higher values of wave steepness than the no change data, with a slightly higher median.

Since breaker type (spilling vs. plunging) appears to be important in defining the characteristics of sediment transport at the shoreline, evolving wave steepness and foreshore slope during the storm are compared through the calculation of the Iribarren number (Eq. 2). Figure 13A is a timestack of values of Iribarren numbers (shown by color variations) every hour alongshore. The Iribarren number is lowest during the building portion (between the 15PM and 16AM surveys) of the storm as steep waves attack the beach face, and is less than 0.5 (the threshold for laboratory spilling breakers, Battjes [1974]) along the majority of the study site south of 3000 m alongshore (Figure 13A). In fact, the threshold for dissipative conditions, $\xi_{\infty} < 0.3$, (as opposed to intermediate or reflective, see Wright and Short [1984]) occur at around 4000, 5500, 6500, and 7500-8500m alongshore. After the peak of the storm, ξ_{∞} increases along the majority of the study site, particularly between 1000 and 4000 m and 7000 and 9000 m alongshore, where ξ_{∞} increases to > 1.25 , the threshold for reflective beaches [Wright and Short, 1984; Stockdon et al., 2006]. Exceptions to this occur at the megacusp located at 4000m alongshore, and to a lesser extent at 8000 m alongshore (Figure 13A), where ξ_{∞} remains < 0.5 or less at some locations, until the 17AM survey (Figure 13A). The region between 4000 and 7000 m alongshore remains classified as an intermediate beach between the 16AM and 18AM surveys (Figure 13A).

6.0 DISCUSSION

6.1 Comparisons between Predicted and Observed Runup

The Stockdon et al. [2006] runup model is widely used to predict runup during extreme storm events and, ultimately, variations in shoreline change [e.g. Stockdon et al.,

2007]. The model is based on the Holman et al. [1986] observations that maximum runup scales with the Iribarren number, and relates wave parameters observed in 10-m of water depth and foreshore slope to the 2% exceedence value of runup, based on an empirical fit over data from a wide range of beach types and wave conditions. Though our observed position of maximum runup during the storm is not statistically identical to the 2% exceedence runup calculated by Stockdon et al. [2006], we feel that the two quantities are still comparable, but one should not be used to “prove” or “disprove” the validity of the other. We expect our runup elevations to be somewhat lower than the $R_{2\%}$ predictions, as our observations are over a shorter time period and thus may not include all of the infragravity fluctuations. In contrast, we observe a negative bias between the predicted and observed data, suggesting that the model under-predicts maximum runup at this field site for this storm (consistent with the slight negative bias indicated by Stockdon et al., [2006]).

Three model runs are run with the goal of identifying the scale of the errors introduced by the static slope assumption and the use of 10-m wave parameters as opposed to an evolving slope and wave parameters more specific to the surf zone. The use of a static slope changes predictions by as much as 1 m in some locations (Figure 5), though the total RMSE when compared to observed data is only slightly improved by including an evolving foreshore slope (from 0.76 to 0.74). Interestingly, including an evolving slope did significantly improve the total overall bias by 11 cm (from -0.6 to -0.49). The largest improvement to the model came from including 5-m reverse-shoaled wave parameters, as opposed to 10-m reverse-shoaled wave parameters, which decreased the RMSE to 0.61 and the bias to -0.24, closer to the mean bias of -0.17 reported by

Stockdon et al. [2006]. This is likely because this field site is characterized by highly irregular surf-zone and nearshore bathymetry, and so including the effects of wave refraction from 10-m to 5-m of water depth improves model predictions. While 10-m wave parameters may be adequate on beaches with shore-parallel depth contours, we suggest that wave parameters at the edge of the surf-zone may more adequately reflect external wave forcing on runup at more complex field sites.

Predicted $R_{2\%}$ explains only 16% of the overall variability in observed runup. Runup predictions are excessively poor during the 15PM survey, and are so low that they often don't intersect the seaward edge of the lidar profile (Figure 7A). Recall that surge is included in the predicted $R_{2\%}$ elevations, and thus the considerably lower predicted values reflect poor modeling of the wave-driven component of $R_{2\%}$. Waves during the 15PM survey are steep, short-period, building wind waves, which produce low Iribarren numbers, the basis of the Stockdon et al. [2006] relationship, and thus lead to rather low maximum runup calculations. Our considerably higher observations of runup maxima during this survey may indicate the presence of larger infragravity fluctuations that are not well-predicted by the infragravity portion of the Stockdon et al. [2006] model. Runup predictions are consistently better during the 17AM through 18AM surveys, when longer period swell dominates. Note surge is relatively similar during the 15PM through 17AM surveys (Figure 1D), and thus the better predictions during the 17AM survey, reflects better parameterization of wave-driven runup. In addition, there appears to be a consistently large discrepancy between the predicted and observed elevations at the southern end of the study site in the pronounced cusp field between 8000 and 9000 m alongshore. This may be due to two factors: (1) errors in observations due to the

potential for radar shadowing by the high cusp horns, or (2) incorrect parameterization of runup in a cusp field due to infragravity induced circulation (as suggested by Stockdon et al. [2006] to occur when beach morphology is alongshore-variable). The cusp field between 8000 and 9000 m alongshore is unique in that the cusps are high amplitude and extend across the upper beach almost from the dune toe all the way down to the waterline creating high relief on the beach (in contrast to the cusp field present between 3000 and 4000 m alongshore which appears to be confined, surprisingly, to the upper beach, with a more uniform foreshore). In region between 8000 and 9000 m alongshore, the high cusp horns may shield the radar from observing the correct position of runup behind it, particularly during the down-rush, biasing the radar observations high. More research is needed to appropriately ground-truth the radar measurements, particularly in regions with high relief.

6.2 Temporal Patterns of Beach Evolution during the Storm

Anecdotal evidence of surprising amounts of beach recovery when waves are still energetic has long suggested that traditional methods of “pre”- and “post”-storm surveys, which often wait for the return to calm conditions, may underestimate the full impact of the storm on the beach [Birkemeier, 1979]. For example, in this study, the apparent discrepancy between the magenta and red lines in Figure 2B & C and Figure 2D & E, respectively, highlight the difference between the “net” change over the course of the storm (red lines), and the change that occurs during the building portion of the storm (magenta lines). The data presented here represent, to the best of our knowledge, one of the first highly resolved spatial and temporal high-resolution data sets of beach

topography evolution *during* a storm, and thus allow for the analyses of the timing of (1) maximum erosion during the storm and (2) the switch in the dominant direction of cross-shore sediment transport during the storm.

6.2.1 Importance of Wave Steepness

Data in Figure 2 show a remarkably high percentage of the overall net erosion occurs during the first 12 hours of the storm when steep, short period waves dominate. In contrast, even though waves still exceed 2.5 m during the next 24 hours (including the peak of the storm), the storm's impact switches to more accretive conditions, as the waves transition to long period swell. Variations in modeled breaking wave steepness seem to predict these changes well (Figure 12)—mean wave steepness is high during the first 12 hours of the storm when erosion is observed, moderate during the following 24 hours when the majority of accretion takes place, and low during the last two surveys when little significant change occurs. Iribarren numbers during the building phase of the storm are also low ($\xi_{\infty} < 0.5$) along the majority of the study site (Figure 13) indicating that breakers with more spilling characteristics may dominate the surf-zone. Spilling characteristics are promoted by both the steep, shorter period growing sea, as well as by the strong onshore winds [Galloway, 1989] which are typical characteristics of Nor'Easters. While surf-zone wave parameters and foreshore slope exhibit first order control on wave breaking type, wind conditions can also have a significant effect on wave breaking characteristics. Strong onshore winds promote both early breaking and more spilling characteristics, thereby widening the surf-zone, where as offshore winds delay breaking and promote more plunging characteristics, narrowing the surf-zone,

changing relationships between breaking wave height and depth [e.g. Galloway et al., 1989; King and Baker, 1996]. Net erosion and offshore transport during spilling, dissipative breaker conditions is also consistent with previous field and laboratory observations [e.g. Sallenger et al., 1985; Kubo and Sunamura, 2001; Wang et al., 2003]. Though breakers with plunging characteristics suspend and transport more sediment than spilling breakers [Kana 1977, 1978; Beach and Sternberg, 1996; Voulgaris and Collins, 2000], undertow is thought to be more important during dissipative storm conditions [Thornton et al., 1996; Gallagher et al., 1998; Ruessink et al., 2007], and thus the net direction of transport is offshore. In contrast, since plunging breakers tend to occur for waves of lower steepness (on steeper beaches), when wave heights are smaller and wavelengths longer (e.g. swell conditions), wave asymmetry is higher during the shoaling phase, and thus net transport is onshore [Elgar et al., 2001; Hoefel and Elgar, 2003; Wang et al., 2003].

One of the drawbacks of using the Iribarren number to determine wave breaking type is that it compares deepwater or breaking wave characteristics to the slope of the foreshore, quantities that only interact with each other during quiescent periods when no bar is present and waves are only breaking at the shoreline (e.g. shore break). In order to more accurately predict the direction of sediment transport by the Iribarren number, breaking wave parameters should be compared to the slope immediately under the actual location of wave breaking—i.e. outer surf-zone wave steepness should be compared to the offshore slope of the shore-parallel bar, while shore-break wave steepness should be compared to the slope of the foreshore. These parameters are difficult to measure simultaneously in the field, and thus deepwater or breaking wave characteristics are used

more often. We believe that lidar time-series data of wave parameters in the inner surf zone from CLARIS may be helpful in the future at quantifying the error introduced by using deepwater or outer surf-zone parameters in predicting wave breaking type at the shoreline [see Chapter 1, this dissertation]. Despite the potential for errors, outer surf-zone wave steepness and the Iribarren number seem to be good overall indicators of temporal trends in the direction of net transport during the storm at this field site.

6.2.2 Importance of Mean Water Levels

Peak erosion of the upper beach also coincides with the peak in mean water level during the first 12 hours, as opposed to the peak in wave runup maxima. Surge peaks just before the 16AM survey (light blue line, Figure 2D), consistent with the observed wind speed maxima, suggesting most of the surge is caused by wind-driven setup across the region. In contrast, predicted runup maxima for the whole storm (stars, Figure 8) and observed runup maxima over the whole storm (black line, Figure 4), peak at the storm peak and 17AM surveys, respectively. The time of these peaks are considerably after the surge peak, when wave period and height are higher. Note the discrepancy between predicted and observed runup maxima over the whole storm is due to the low-tide timing of the CLARIS surveys. This suggests that both shoreline erosion and upper-beach volume change during moderate storms may be more sensitive to mean water levels as opposed to runup water levels. In addition, although the position of the shoreline recovers fully in the 10 days following the storm, the magnitude of upper-beach accretion is less than the magnitude of upper beach erosion during the storm (Figure 2F), indicating that no mechanism is available to rapidly transport sediment back to the upper beach after

mean water levels subside. Thus the overall net effect of the storm on the beach may also be due to the length of elevated mean water levels: if surge remains high as waves transition to long period swell, the storm may induce a net volume gain to the upper beach, whereas if surge subsides before waves transition to long period swell, net volume change may be a loss over the storm.

6.3 Spatial Patterns of Beach Evolution during the Storm

Superimposed upon general temporal trends in beach erosion during storms is significant spatial variability in the amount of erosion (or accretion) that occurs [e.g. List et al., 2006; Stockdon et al., 2003]. Predicting these variations is important both to coastal planners managing development and homeowners preparing for approaching storms. Spatial variability is observed in response to extreme events, such as hurricanes [e.g. Stockdon et al., 2003], as well as to smaller, more frequent events, such as Nor'Easters [List et al., 2006]. We test three hypotheses for alongshore-variable beach erosion during a Nor'Easter on the Outer Banks [Figure 11]. Hypothesis 1 extends the effects of alongshore variable wave height in the nearshore and surf-zone onto the shoreline. It proposes that wave focusing over irregular bathymetry creates regions with elevated wave height at the shoreline that could potentially lead to increased erosion. This is hypothesized by Schupp et al. [2006] to occur at this field site in Kitty Hawk, NC. Hypothesis 2 is the recent storm-impact-scaling approach [Sallenger 2000], that compares maximum and mean water levels to various beach morphological features, such as the dune crest or base. Hypothesis 3 is a fairly simple model that merely predicts a relationship between decreased numbers of offshore sandbars and increased erosion at the shoreline [Kannan et al., 2003].

Comparisons between the three different predictors and beach volume change during the building portion of the storm suggest that the simple bar model (hypothesis 3) produces the best results. Neither wave height nor relative runup, $R_{2\%} / D_{10e}$, produced significant correlations with beach volume change. The number of offshore bars does, however, predict the overall regional trend of increased erosion between 4500 and 7500 m alongshore during the building phase of the storm (Figure 11E and F). More erosion is observed onshore of where the inner bar has welded to the shoreline, creating only two offshore peaks in dissipation (a wide swash zone and offshore shore-parallel bar; Figure 10C-F). In contrast, less erosion is observed onshore of the double-barred regions, characterized by three peaks in dissipation (a narrow swash zone and inner and outer bar; Figure 10A-C). Since the morphological expression of the swash zones is very different between the two regions, we hypothesize that the driving hydrodynamic processes are as well. In the erosive region, where waves have only dissipated over the outer shore-parallel bar before reaching the shoreline, bore height may be higher at the base of the swash (supported by in-field visual observations, see Figure 10C vs. A), and has more energy available to transfer to the sediment at its collapse. In addition, the flatter slope of the sub-aqueous foreshore due to the welded inner bar may promote an early transition to spilling characteristics at the start of the storm in this region, prolonging erosive conditions. The constant presence of incoming bores may also increase the likelihood of hydraulic jumps, which promote offshore sediment transport [Butt and Russell, 2005]. In addition, our observations of maximum runup (Figure 3) are consistently lower in this region, suggesting that the highly dissipative foreshore is limiting runup inundation [e.g. Stockdon et al., 2006], and preventing a return mechanism for sediment to the beach.

In contrast, the narrow swash observed onshore of the double-barred, less-erosive regions, suggests less energy is reaching the beach and therefore sediment transport is reduced. Since waves are dissipated over two bars before reaching the shoreline, the initial bore height may be lower and energy at incident frequencies most likely depressed, exposing the beachface to less energetic swash dynamics [e.g. Masselink and Puleo, 2006]. The combination of dominant infragravity motions and steeper foreshore slopes may be responsible for the comparatively higher runup maxima [Stockdon et al., 2006] observed in the single-barred regions. While runup maxima may be higher, swash interactions with incoming waves may be less energetic, preventing significant profile adjustment and subsequent shoreline change.

Since the intensity of radar returns in the nearshore can be used as a proxy for wave dissipation [see Chapter 1], we sum the total dissipation over the inner surf zone, and compare it to beach volume change during the building portion of the storm (Figure 14). Correlation analysis indicates dissipation in the inner surf-zone and volume change are significantly positively correlated such that areas with less energy dissipation in the inner surf zone experience more volume loss ($R=0.71$, $p=0.001$). Linear regression analysis indicates that alongshore variations in inner surf zone dissipation explained 50% of the variability in volume change during the building portion of the storm, confirming the simple bar hypothesis that increased dissipation over multiple offshore sandbars leads to decreased erosion onshore.

6.4 Other Metrics for Predicting the Relative Magnitude and Direction of Cross-Shore Sediment Transport during Storms

All of the metrics tested in this study are “erosion metrics”, that is, they are all designed to predict alongshore variations in erosion during storms and disregard the possibility of accretion. Storms can often have a net accretional effect, however, with significant percentages of the eroded beach volume returning in less than 24 hours following the peak of the storm [Birkemeier, 1979]. For example, in this study the greatest inter-survey loss in beach volume occurs at 7000 m alongshore during the building portion of the storm. In the 24 hours following this erosion, including the peak of the storm, almost equal accretion occurs on the upper beach (Figure 2D), leaving a net change over the course of the storm of close to 0 (Figure 2E). At the shoreline, accretion during the falling portion of the storm exceeds erosion during the building portion of the storm in this same region, creating a net accretional effect on the shoreline (Figure 2B). This is similar to the results of Houser and Greenwood [2007] who observe initial offshore movement of a swash bar (resulting in shoreline erosion), followed by rapid onshore movement of the same swash bar during the peak of a storm, resulting in rapid shoreline accretion. In that case, the direction of movement of the swash bar is dependent on mean water levels altering the position of wave breaking over the bar—during the initial high water levels, waves broke landward of the swash bar crest, causing offshore movement, but as water levels receded (and wave height changed negligibly), wave breaking occurred on the seaward slope of the swash bar driving it onshore at a rate of 1 m hr^{-1} . Due to the almost continual dissipation of waves across the sub-aqueous foreshore in the welded-inner bar region in our study area, it is difficult to distinguish the movement of the welded inner bar in the radar intensity images. Nevertheless, the

observed pattern of erosion and accretion is consistent with that described above by Houser and Greenwood [2007] for the rapid on and offshore movement of a swash bar. Metrics need to be created that are capable of predicting not only erosion during storms, but also accretion, and the relative importance (and perhaps reversal) of on-and offshore transport, particularly within the inner surf zone, during a storm event.

To this end, we investigate the relationship of inter-survey volume change with median wave steepness along the study site during the storm, as changes in the direction of sediment transport in the surf-zone can be related to wave type (large storm waves favor offshore transport, whereas smaller swell waves favor onshore transport). A threshold value of wave steepness (~ 0.038) differentiates well between erosive and accretive or no change conditions; however, the difference between accretion and no change is less clear (Figure 12). Data suggest intermediate values of wave steepness will result in accretive conditions, but the results are far from conclusive. Given that the Iribarren number, ξ_{∞} , varies both spatially and temporally during the storm (Figure 13), describing characteristics of wave breaking and thus variations in the driving forces of sediment suspension and transport under breaking waves, ξ_{∞} is compared with net volume change during the storm. Specifically, the percentage of time that $\xi_{\infty} < 0.5$ during the storm is plotted with net volume change in Figure 15. A relationship is apparent in which areas that experienced net erosion experienced low ξ_{∞} for a longer period of time. That is, regions with high erosion rates are subjected to breakers with more spilling characteristics for a longer period of time. Areas that rarely experienced $\xi_{\infty} < 0.5$ (e.g. the region between 1000 and 3000 m alongshore), also experienced little significant change during the storm. The two exceptions to this pattern are on the

megacusps at 4000 and 8000 m alongshore, where extensive periods of low ξ_{∞} resulted in little significant shoreline change during the storm. Here, spilling conditions prevailed over longer periods of time and the width of the inner surf-zone was highest (Figure 9C). These data suggest that extremely dissipative conditions may have dominated, increasing the importance of frictional losses and reducing the amount of energy that reached the shoreline.

Median ξ_{∞} is also calculated between each survey time-pair and compared to inter survey volume change in Figure 16A, similar to our comparison with wave steepness in Figure 12A. A positive relationship between ξ_{∞} and volume change is observed; however, threshold values are more difficult to determine. For the erosive data, ξ_{∞} is < 0.6 eighty-four percent of the time and < 0.5 sixty-six percent of the time (Figure 16B), where as for the accretive data, ξ_{∞} is > 0.6 eighty-four percent of the time and > 0.5 eighty-six percent of the time (Figure 16D). In addition, ξ_{∞} is < 0.6 and 0.5 only nineteen and eight percent of the time for the no change data (Figure 16C), suggesting that a transition between erosive conditions and accretive/no change conditions occurs at around $\xi_{\infty} = 0.5$ to 0.6 , comparable to the transition between spilling and plunging breakers observed in the laboratory by Battjes [1974]. Similar to wave steepness, however, the Iribarren number has difficulty distinguishing between no significant change and accretion.

Our data suggest that wave steepness and its relative value in comparison to foreshore slope (the Iribarren number), in addition to the configuration of the surf-zone (one vs. two bars) and subsequent dissipation within the inner surf zone, are important in predicting the erosion/accretion response of the beach to moderate Nor'Easters. Along

this field site, wave steepness is modulated by irregular offshore bathymetry, which induces wave refraction and causes wave height to vary alongshore (see Chapter 2). The lack of a direct relationship between wave height and beach erosion, however, suggests other factors modulate the response of the beach. Specifically, variations in the amount of dissipation within the surf-zone due to irregular bar configurations appear to also be important. In addition, variations in both foreshore slope and surf-zone slope may induce alongshore variations in wave breaking type that alter the direction or amount of cross-shore sediment transport between the beach and inner surf-zone in different regions alongshore. Finally, while three dimensional circulation patterns within the surf-zone, induced by the shore-oblique features may also be important, observed erosion patterns during this storm did not align with expected erosional currents in the embayments (see Chapter 2). This may be due to the fact that most of the erosion during this storm occurs during the high-angle waves characteristic of the building portion of the storm, when wave convergence and divergence patterns are not as complex (see Chapter 2). More work is needed to address how all of these factors interact with each other to produce the observed erosion and accretion patterns throughout the course of the storm.

7.0 CONCLUSION

We observed 10 km of beach on the Outer Banks of North Carolina semi-daily during a Nor'Easter using CLARIS, and analyzed spatial and temporal patterns in both shoreline and beach-volume erosion and accretion with respect to modeled wave parameters. In addition, we measured alongshore variations in observed wave runup maxima and compared them to predicted $R_{2\%}$ statistics using the Stockdon et al. [2006]

equation. We then tested three previously proposed hypotheses for predicting alongshore-variable response to storm events, and evaluated their success during the storm. Our data suggest:

- The majority of both shoreline and upper beach-volume erosion occurred during the building portion of the storm when wave steepness and surge were highest, and Iribarren numbers low.
- Recovery of > 50% of the original shoreline erosion occurred along more than half the study site during the next 24 hours, as waves peaked and subsequently transitioned to less-steep, long-period swell.
- In contrast to the shoreline, only 16% of the study-site experienced accretion on the upper beach during the falling portion of the storm, perhaps due to low mean water levels preventing transport to the higher elevations.
- Runup elevations during the storm are better predicted using an evolving foreshore slope and breaking-wave characteristics (as opposed to wave parameters from 10 m water depth) in the Stockdon et al. [2006] model, however, they still only explain 16% of the variability in the observed runup elevations.
- Alongshore-variable breaking wave height and relative runup elevation are not good predictors of alongshore variations in beach volume change at this site during a moderate Nor'Easter. In contrast, the number of offshore bars appears to exert first order control on regional patterns of erosion, such that double-barred regions experience less erosion than single barred regions, supporting the work of Kannan et al. [2003].

- Inner surf zone dissipation, quantified using summed radar return intensities, explained 50% of the variability in volume change during the building portion of the storm, confirming that alongshore variations in surf-zone morphology and its effect on wave dissipation near the shoreline is important for predicting beach erosion during storms.
- Spatial and temporal patterns in the Iribarren number show promise at predicting both alongshore and temporal variations in the direction and magnitude of cross-shore transport during the storm, however, more work is needed to further incorporate interactions between alongshore-variable surf-zone configuration, mean water levels, and swash-zone processes into a predictive metric.

REFERENCES

- Aagaard, T., and J. Holm (1989), Digitization of Wave Run-up Using Video Records, *J. Coast. Res.*, 5(3), 547-551.
- Ashton, A., J. H. List, A. B. Murray, and A. S. Farris (2003), Links between erosional hotspots and alongshore sediment transport, *Proceedings of the International Conference on Coastal Sediments '03*, ASCE, 981-238.
- Battjes, J. A. (1974), Surf similarity, *Proceedings of the 14th Coastal Engineering Conference*, ASCE, 466-479 .
- Beach, R. A., and R. W. Sternberg (1996), Suspended-sediment transport in the surf zone: response to breaking waves, *Cont. Shelf Res.*, 16(15), 1989-2003.
- Bell, P. S. (1999), Shallow water bathymetry derived from an analysis of X-band marine radar images of waves, *Coast. Eng.*, 37(3-4), 513-527.
- Benedet, L., C. W. Finkl, and W. M. Hartog (2007), Processes Controlling Development of Erosional Hot Spots on a Beach Nourishment Project, *J. Coast. Res.*, 23(1), 33-48.
- Benton, S. B., C. J. Bellis, M. F. Overton, J. S. Fisher, J. L. Hench, and R. D. Dolan (1997), North Carolina long-term average annual rates of shoreline change. Prepared for Division of Coastal Management, North Carolina Department of Environment, Health, and Natural Resources. , Raleigh, NC.
- Birkemeier, W. (1984), Timescales of Nearshore Profile Change, *Proceedings of the 19th Coastal Engineering Conference*, ASCE, 1507.
- Birkemeier, W. A., R. J. Nicholls, and G. Lee (1999) Storms, storm groups and nearshore morphologic change, *Proceedings of the International Conference on Coastal Sediments '99*, ASCE 1109-1123.
- Browder, A. G., and J. E. McNinch (2006), Linking framework geology and nearshore morphology: Correlation of paleo-channels with shore-oblique sandbars and gravel outcrops, *Mar. Geol.*, 231(1-4), 141-162.
- Butt, T., and P. Russell (2005), Observations of hydraulic jumps in high-energy swash, *J. Coast. Res.*, 21(6), 1219-1227.
- Elgar, S., E. L. Gallagher, and R. T. Guza (2001), Nearshore sandbar migration, *J. Geophys. Res.*, 106, 11623-11627.
- Fenster, M. S., and R. Dolan (1993), Historical Shoreline Trends along the Outer Banks, North Carolina: Processes and Responses, *J. Coast. Res.*, 9(1), 172-188.

- Gallagher, E. L., S. Elgar, and R. T. Guza (1998), Observations of sand bar evolution on a natural beach, *J. of Geophys. Res.*, 103(C2), 3203-3215.
- Galvin, C. J. (1968), Breaker Type Classification on Three Laboratory Beaches, *J. Geophys. Res.*, 73, 3651-3659.
- Guza, R. T., and E. B. Thornton (1981), Wave set-up on a natural beach, *J. Geophys. Res.*, 86(C5), 4133-4137.
- Guza, R. T., and E. B. Thornton (1982), Swash oscillations on a natural beach, *J. Geophys. Res.*, 87(C1), 483-492, doi: 10.1029/JC087iC01p00483.
- Haller, M. C., and D. R. Lyzenga (2003), Comparison of radar and video observations of shallow water breaking waves, *IEEE Trans. Geosci. Remote Sens.*, 41(4), 832-844.
- Hanslow, D., and P. Nielsen (1993), Shoreline set-up on natural beaches, *J. Coast. Res.*, 15, 1-10.
- Hoefel, F., and S. Elgar (2003), Wave-Induced Sediment Transport and Sandbar Migration, *Science*, 299(5614), 1885-1887.
- Holland, K. T., B. Raubenheimer, R. T. Guza, and R. A. Holman (1995), Runup kinematics on a natural beach, *J. Geophys. Res.*, 100(C3), 4985-4993.
- Holland, K. T., and J. A. Puleo Variable swash motions associated with foreshore profile change, *J. Geophys. Res.*, 106, doi: 10.1029/1999JC000172.
- Holman, R. A. (1986), Extreme value statistics for wave run-up on a natural beach, *Coast. Eng.*, 9(6), 527-544.
- Holman, R. A., and R. T. Guza (1984), Measuring run-up on a natural beach, *Coast. Eng.*, 8(2), 129-140.
- Holman, R. A., and A. H. Sallenger (1985), Setup and swash on a natural beach, *J. Geophys. Res.*, 90(C1), 945-953.
- Houser, C., and B. Greenwood (2007), Onshore migration of a swash bar during a storm, *J. Coast. Res.*, 23(1), 1-14.
- Hsu, T. J., and B. Raubenheimer (2006), A numerical and field study on inner-surf and swash sediment transport, *Cont. Shelf Res.*, 26(5), 589-598.
- Iversen, H. W. (1952), Studies of Wave Transformation in Shoaling Water, Including Breaking. In *Gravity Waves*. National Bureau of Standards Circular No. 52, 9-32.

- Jackson, N. L., G. Masselink, and K. F. Nordstrom (2004), The role of bore collapse and local shear stresses on the spatial distribution of sediment load in the uprush of an intermediate-state beach, *Mar. Geol.*, 203(1-2), 109-118.
- Kannan, S., T. C. Lippmann, and J. H. List (2003), The relationship of nearshore sandbar configuration to shoreline change, *Proceedings of the International Conference on Coastal Sediments '03*, ASCE.
- Lee, G., R. J. Nicholls, and W. A. Birkemeier (1998), Storm-driven variability of the beach-nearshore profile at Duck, North Carolina, USA, 1981–1991, *Mar. Geol.*, 148(3-4), 163-177.
- Lippmann, T. C., and R. A. Holman (1989), Quantification of sand bar morphology: A video technique based on wave dissipation, *J. of Geophys. Res.*, 94(C1), 995-1011.
- Lippmann, T. C., S. Kannan, and J. List (2004), The Relationship Of Nearshore Sandbar Configuration to Shoreline Change, Ocean Sci. Meet. Suppl., Abstract OS32F-06.
- List, J. H., A. S. Farris, and C. Sullivan (2006), Reversing storm hotspots on sandy beaches: Spatial and temporal characteristics, *Mar. Geol.*, 226(3-4), 261-279.
- Longuet-Higgins, M. S., and R. W. Stewart (1964), Radiation stresses in water waves; a physical discussion, with applications, *Deep Sea Res.*, 11, 529-529-562.
- Masselink, G., and M. Hughes (1998), Field investigation of sediment transport in the swash zone, *Cont. Shelf Res.*, 18(10), 1179-1199.
- Masselink, G., P. Russell, I. Turner, and C. Blenkinsopp (2009), Net sediment transport and morphological change in the swash zone of a high-energy sandy beach from swash event to tidal cycle time scales, *Mar. Geol.*, 267(1-2), 18-35.
- Masselink, G., and J. A. Puleo (2006), Swash-zone morphodynamics, *Cont. Shelf Res.*, 26(5), 661-680.
- McNinch, J. E. (2007), Bar and Swash Imaging Radar (BASIR): A Mobile X-band Radar Designed for Mapping Nearshore Sand Bars and Swash-Defined Shorelines Over Large Distances, *J. Coast. Res.*, 23(1), 59-74.
- McNinch, J. E. (2004), Geologic control in the nearshore: shore-oblique sandbars and shoreline erosional hotspots, Mid-Atlantic Bight, USA, *Mar. Geol.*, 211(1-2), 121-141.
- McNinch, J. E. and J. L. Miselis (2009), Geology metrics for predicting shoreline change using seabed and sub-bottom observations from the surf zone, edited by C. Sherwood and M. Li, *Journal of Sedimentology (Special Publication)*, in press.

Miselis, J. L. (2007), Nearshore morphology and lithology: links to framework geology and shoreline change, Ph.D. Dissertation, School of Marine Science, William and Mary, Williamsburg, VA.

Miselis, J. L., and J. E. McNinch (2006), Calculating shoreline erosion potential using nearshore stratigraphy and sediment volume: Outer Banks, North Carolina, *J. Geophys. Res.*, 111.

Nielsen, P. (1992), *Coastal bottom boundary layers and sediment transport*, Advanced Series on Ocean Engineering, Vol. 4, World Scientific.

Nielsen, P., and D. J. Hanslow (1991), Wave runup distributions on natural beaches, *J. Coast. Res.*, 7(4), 1139-1152.

Plant, N. G., H. F. Stockdon, A. H. Sallenger Jr., M. J. Turco, J. W. East, A. A. Taylor, and W. A. Shaffer (2010), Forecasting Hurricane Impact on Coastal Topography, *Eos Trans. AGU*, 91(7), doi:10.1029/2010EO070001.

Plant, N. G., B. G. Ruessink, and K. M. Wijnberg (2001), Morphologic properties derived from a simple cross-shore sediment transport model, *J. Geophys. Res.*, 106(C1), 945-958.

Raubenheimer, B., and R. T. Guza (1996), Observations and predictions of run-up, *J. Geophys. Res.*, 101(25), 575-25.

Riggs, S. R., W. J. Cleary, and S. W. Snyder (1995), Influence of inherited geologic framework on barrier shoreface morphology and dynamics, *Mar. Geol.*, 126(1-4), 213-234, doi: 10.1016/0025-3227(95)00079-E.

Roelvink, J. A., and I. Brøker (1993), Cross-shore profile models, *Coast. Eng.*, 21(1-3), 163-191.

Roelvink, J. A., and M. J. F. Stive (1989), Bar-Generating Cross-Shore Flow Mechanisms on a Beach, *J. Geophys. Res.*, 94, 4785-4800, doi: 10.1029/JC094iC04p04785.

Ruessink, B. G., P. S. Bell, I. M. J. van Enckevort, and S. G. J. Aarninkhof (2002), Nearshore bar crest location quantified from time-averaged X-band radar images, *Coast. Eng.*, 45(1), 19-32.

Ruessink, B. G., M. G. Kleinhans, and P. G. L. Van den Beukel (1998), Observations of swash under highly dissipative conditions, *J. Geophys. Res.*, 103(C2), 3111-3118.

Ruessink, B. G., Y. Kuriyama, A. Reniers, J. A. Roelvink, and D. J. R. Walstra (2007), Modeling cross-shore sandbar behavior on the timescale of weeks, *J. Geophys. Res.*, 112.

Ruggiero, P., and R. A. Holman (2004), Wave run-up on a high-energy dissipative beach, *J. Geophys. Res.*, 109, 1-12.

Sallenger Jr, A. H. (2000), Storm Impact Scale for Barrier Islands, *J. Coast. Res.*, 16(3), 890-895.

Sallenger, A. H., R. A. Holman, and W. A. Birkemeier (1985), Storm-induced response of a nearshore-bar system, *Mar. Geol.*, 64(3-4), 237-257.

Schupp, C. A., J. E. McNinch, and J. H. List (2006), Nearshore shore-oblique bars, gravel outcrops, and their correlation to shoreline change, *Mar. Geol.*, 233(1-4), 63-79.

Stockdon, H. F., A. H. Sallenger, R. A. Holman, and P. A. Howd (2007), A simple model for the spatially-variable coastal response to hurricanes, *Mar. Geol.*, 238(1-4), 1-20.

Stockdon, H. F., A. H. Sallenger, P. A. Howd, and R. A. Holman (2003), Longshore variability of the coastal response to Hurricanes Bonnie and Floyd, *Proceedings, International Conference on Coastal Sediments '03*, ASCE.

Thieler, E. R., A. L. Brill, W. J. Cleary, C. H. Hobbs, and R. A. Gammisch (1995), Geology of the Wrightsville Beach, North Carolina shoreface: Implications for the concept of shoreface profile of equilibrium, *Mar. Geol.*, 129(3), 365-365.

Thornton, E. B., R. T. Humiston, and W. Birkemeier (1996), Bar/trough generation on a natural beach, *J. Geophys. Res.*, 101(C5), 12097-12110.

Thornton, E. B., J. MacMahan, and A. H. Sallenger (2007), Rip currents, mega-cusps, and eroding dunes, *Mar. Geol.*, 240(1-4), 151-167.

Voulgaris, G., and M. B. Collins (2000), Sediment resuspension on beaches: response to breaking waves, *Mar. Geol.*, 167(1-2), 167-187, doi: DOI: 10.1016/S0025-3227(00)00025-6.

Weishar, L. L., and R. J. Byrne (1978), Field study of breaking wave characteristics, *Proceedings of the 16th Coastal Engineering Conference*, ASCE.

FIGURE CAPTIONS

Figure 1. Physical characteristics of the Nor'Easter. Wave parameters, including significant wave height and peak period, wave steepness, and wave direction (relative to shore normal) as recorded by the 17-m waverider at the USACE-FRF pier are shown in panels A-C, respectively. Water level recorded by the NOAA tide gauge at the end of the pier is shown in panel D, whereas wind speed and direction (relative to true north) are plotted in panel E. Vertical colored lines represent timings of surveys: 15PM survey (purple), 16AM survey (cyan), 16PM survey (green), 17AM survey (yellow), 17PM survey (orange), 18AM survey (magenta).

Figure 2. Shoreline and volume change during and post-storm. In panel A, the MHW shoreline is shown for all surveys, with locations of megacusps shaded in blue. In panel B, inter-survey shoreline change is shown whereas in panel C, net shoreline change over the whole storm and shoreline change during the recovery period is shown. Panels D and E are similar to B and C, except for volume change. Panel F shows the overall volume change from the pre-storm 15PM survey to the recovery 28PM survey. Dotted lines in all show plus or minus 10 cm significance thresholds.

Figure 3. Foreshore slope during the storm. In panel A, spatial-time stacks of linearly interpolated foreshore slope during the storm are plotted. Warmer colors are steeper slopes, cooler colors are flatter slopes. Solid black lines represent times of CLARIS surveys. Panel B shows wave height in 17-m water depth for reference.

Figure 4. Observed runup during the storm. CLARIS observations of runup maxima are shown for each survey (colored dots). Runup maxima over all the surveys during the storm are connected by the black line, with the majority of runup maxima occurring during the 17AM survey (yellow dots).

Figure 5. Spatial predicted and observed runup comparison. Panels A-E show observed (blue) and predicted runup maxima from each model runs 1-3 (red, green, black, respectively) for each CLARIS survey.

Figure 6. Relationship between observed and predicted runup. Predicted runup maxima from model run 1 are compared with observed runup maxima during each survey. Linear regression analysis (blue line) indicates predicted runup explains only 16% of the variability of observed runup. A 1:1 relationship is described by the black line.

Figure 7. Comparison of observed swash inundation and predicted swash inundation. Runup maxima predictions are converted to maximum swash inundation position (magenta line) and compared to observed maximum swash inundation (black line) for each survey. Colors indicate lidar derived beach topography. Largest differences between observed and predicted swash inundation consistently occur between 8000 and 9000 m alongshore in the high-relief cusp field.

Figure 8. Predicted runup maxima during the storm. Spatial time-stacks of predicted runup maxima from model run 1 are shown. Time is on the y-axis, and distance

alongshore is on the x -axis. Runup maxima are represented by colors, with warmer colors indicating higher elevations and cooler colors indicating lower elevations. Black lines denote CLARIS survey times, and start denote total predicted runup maxima for the whole storm. Storm impact is identified by comparing runup maxima to the elevation of the dune base, with magenta stars indicating the “swash” regime, and white stars indicating collision with the base of the dune.

Figure 9. Surf-zone morphology from radar morphology mosaic. Panels A shows an example radar morphology mosaic during the storm, with warmer colors representing high radar intensity returns, and cooler colors representing low radar intensity returns. The waterline (thick solid line), swash zone (narrow solid black line), inner bar (dashed black line), and 5-m isobath (dotted black line), are denoted for the 16AM survey. Interpretation of the morphology mosaic is shown in panel B. White regions correspond to places of wave breaking, blue regions correspond to places of low wave dissipation, and the yellow region represents the beach. In panel C, outer surf-zone width (red line), inner surf-zone width (blue line), and the number of peaks in dissipation offshore of the beach (green stars) are shown. Outer and inner surf-zone width both vary significantly alongshore with variations in outer surf-zone width controlled by the shore-oblique bars and troughs and variations in inner surf-zone width controlled by the position of the inner bar.

Figure 10. Photo and radar characterization of single vs. double barred regions. In panels A-C respectively, an example photo, radar intensity timestack, and time-averaged radar

intensity profile are used to characterize the double-barred region between 1000 and 4000 m alongshore. In panels D-F the same data is used to characterize the single-barred region between 5500 and 7500 m alongshore. In panels B and E, light colors represent high-intensity radar returns off of breaking waves. Horizontal lines correspond to the morphological features (colored dots) identified objectively using the time-average radar intensity profiles in figure C and F. The double-barred region is characterized by a narrow swash zone, whereas the single-barred region is characterized by a wide, dissipative swash.

Figure 11. Hypothesis tests of alongshore variable beach change metrics. Panels A-B, C-D, and E-F, show the hypothesis tests of the erosion metrics: wave height, relative runup, and # of offshore bars, respectively. In panels A and C the spatial cross-correlation between volume change (red line, right axis) and wave height and relative runup (blue lines, left axis), respectively are shown, whereas linear regression of the variables are plotted in B and D. The black line represents the linear best fit. In panel E, number of offshore peaks in dissipation (blue stars, left axis) and volume change (red line, right axis) are shown. Results of the student's t-test are shown in panel F.

Figure 12. Comparison of inter-survey beach volume change and mean wave steepness. Panel A compares inter-survey volume change with mean wave steepness between the each survey time-pair. Erosive locations are shaded in blue, no change in green, and accretive locations in blue. Histograms of wave steepness values based on the volume change type classification are shown in panels B through D, respectively. The black line

on panel A represents a wave steepness threshold of 0.0385 that separates erosive conditions from no-change or accretive conditions based on statistics calculated for each volume change type.

Figure 13. Iribarren number during the storm. Spatial time-stack of Iribarren numbers during the storm, with time on the y-axis and distance alongshore on the x-axis. Colors represent values of Iribarren numbers, with warmer colors indicating higher values (regions that are intermediate to reflective with more plunging breakers) and cooler colors indicating lower values (regions that are more dissipative with spilling breakers).

Figure 14. Relationship between inner surf-zone dissipation and beach volume change. A significant, positive correlation between the sum of radar return values across the inner surf zone, used as a proxy for dissipation (blue line) and beach volume change during the building portion of the storm (green line), is shown in panel A. Linear regression analysis (black line, panel B) suggests inner surf-zone dissipation explains 50% of the variability in beach volume change during the building portion of the storm.

Figure 15. Comparison of percentage of time $\xi_{\infty} < 0.5$ (spilling breakers) to volume change. Net volume change during the storm (15PM to 18AM survey), is shown in dark blue, with the percentage of time Iribarren numbers indicate spilling breakers shown in cyan. The two variables agree well, with the exception of at 4000 and 8300 m alongshore.

Figure 16. Comparison of inter-survey beach volume change and median Iribarren number. Similar to Figure 12, panel A compares inter-survey volume change with median Iribarren number between the each survey time-pair at each location alongshore. Erosive locations are shaded in blue, no change in green, and accretive locations in blue. Histograms of Iribarren numbers based on the volume change type classification are shown in panels B through D, respectively. The two black horizontal lines on panel A represents an Iribarren number threshold of 0.5 to 0.6, which somewhat separates erosive conditions from no-change or accretive conditions. The threshold value is based on statistics calculated for each volume change type.

Table 1

MODEL	RMSE (m)					
	15PM	16AM	17AM	17PM	18AM	ALL
5-m waves, dynamic slope	0.79	0.69	0.55	0.48	0.51	0.61
10-m waves, dynamic slope	0.84	0.67	0.68	0.65	0.81	0.74
10-m waves, static slope	0.84	0.71	0.71	0.69	0.83	0.76
	BIAS (m)					
5-m waves, dynamic slope	-0.62	-0.33	-0.1	-0.02	-0.13	-0.24
10-m waves, dynamic slope	-0.69	-0.29	-0.41	-0.41	-0.64	-0.49
10-m waves, static slope	-0.69	-0.39	-0.46	-0.43	-0.64	-0.6

Figure 1.

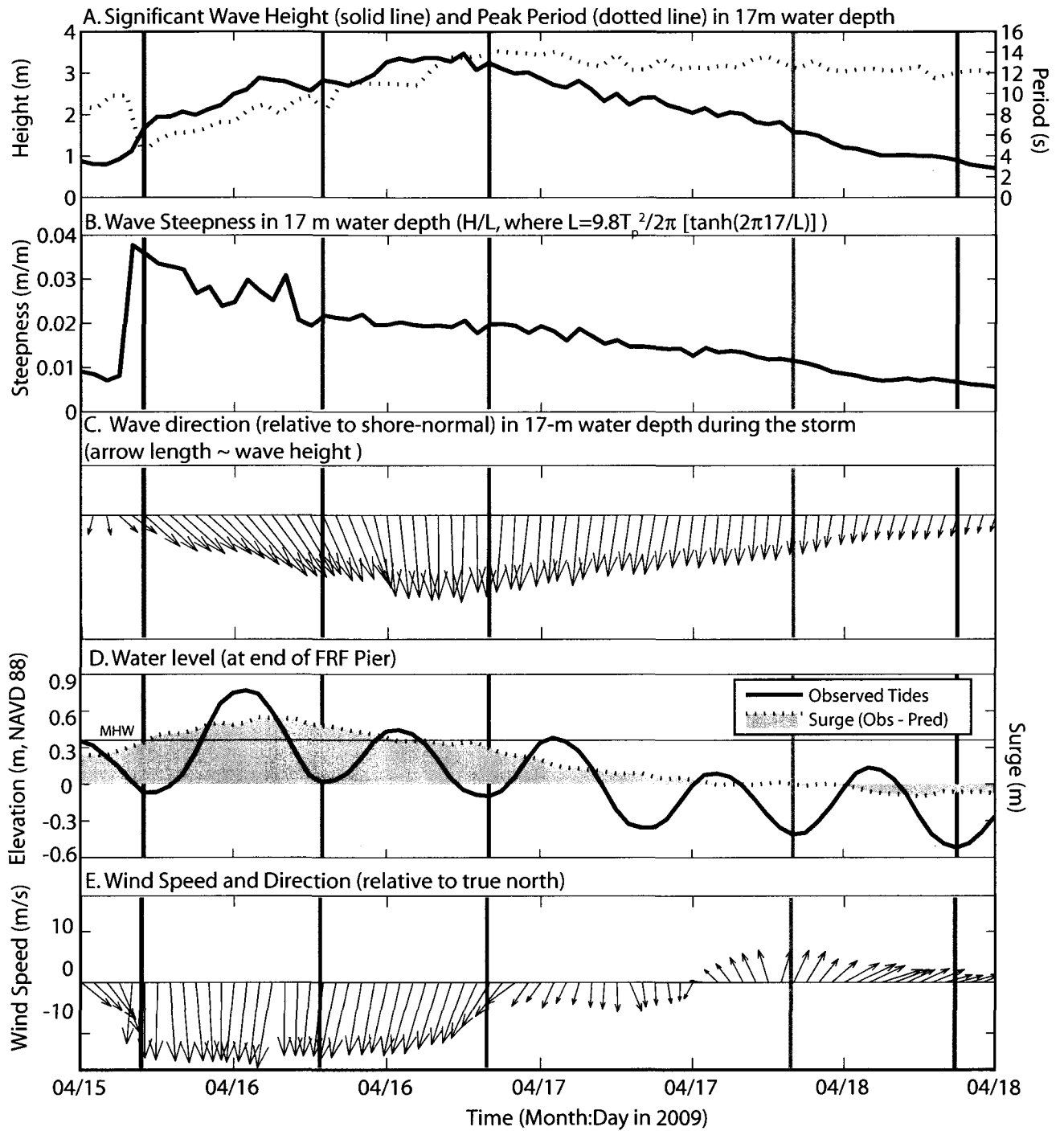


Figure 2.

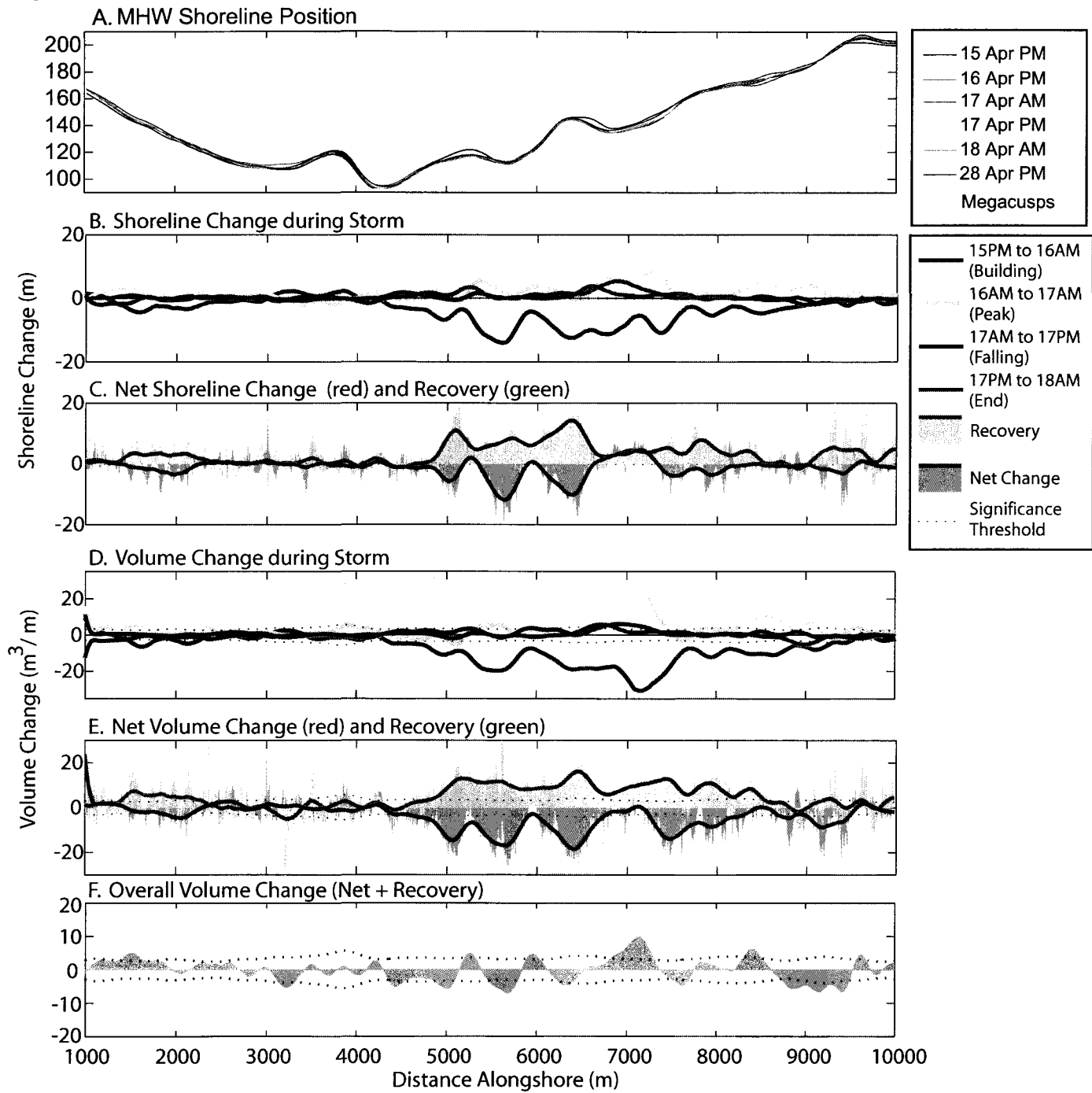


Figure 3.

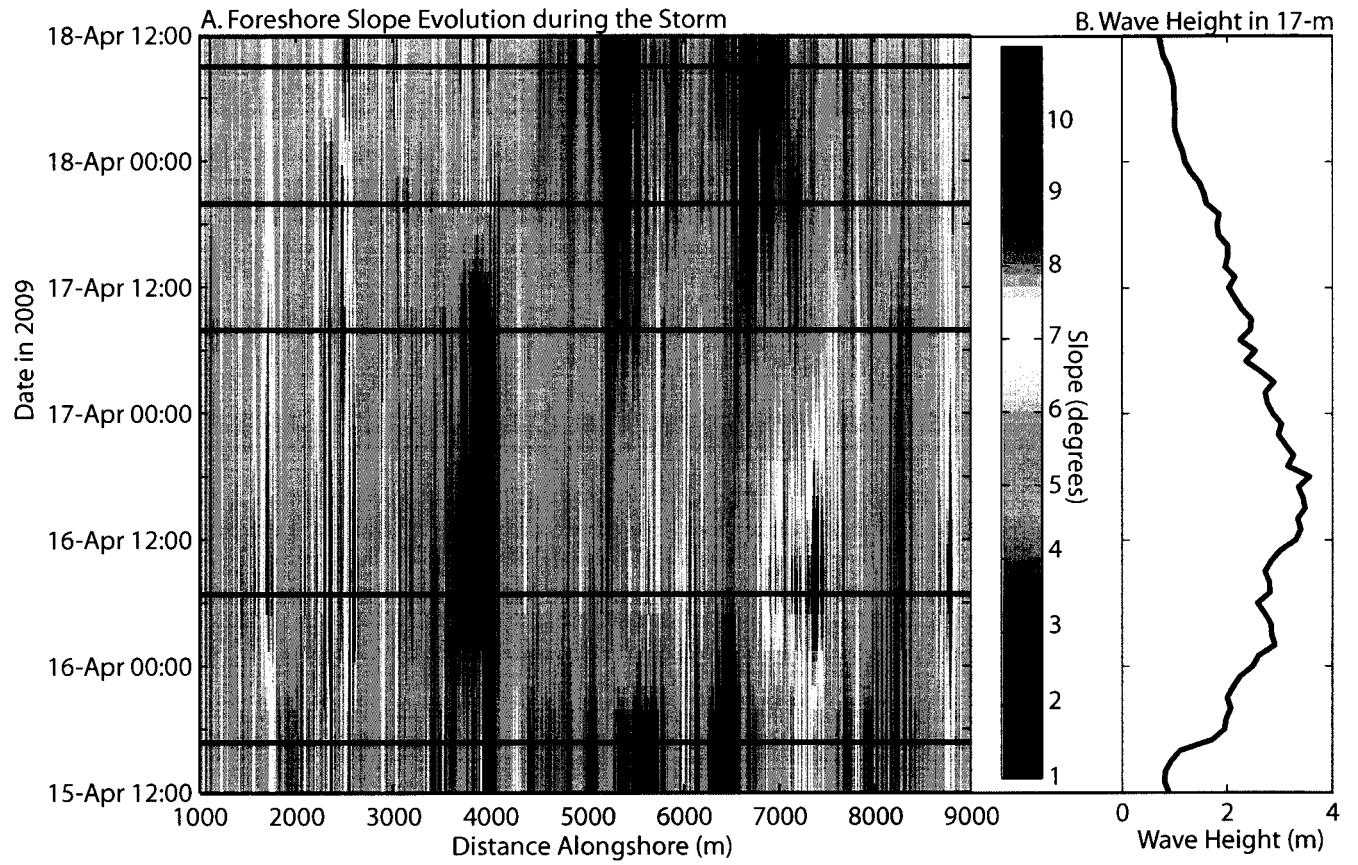


Figure 4.

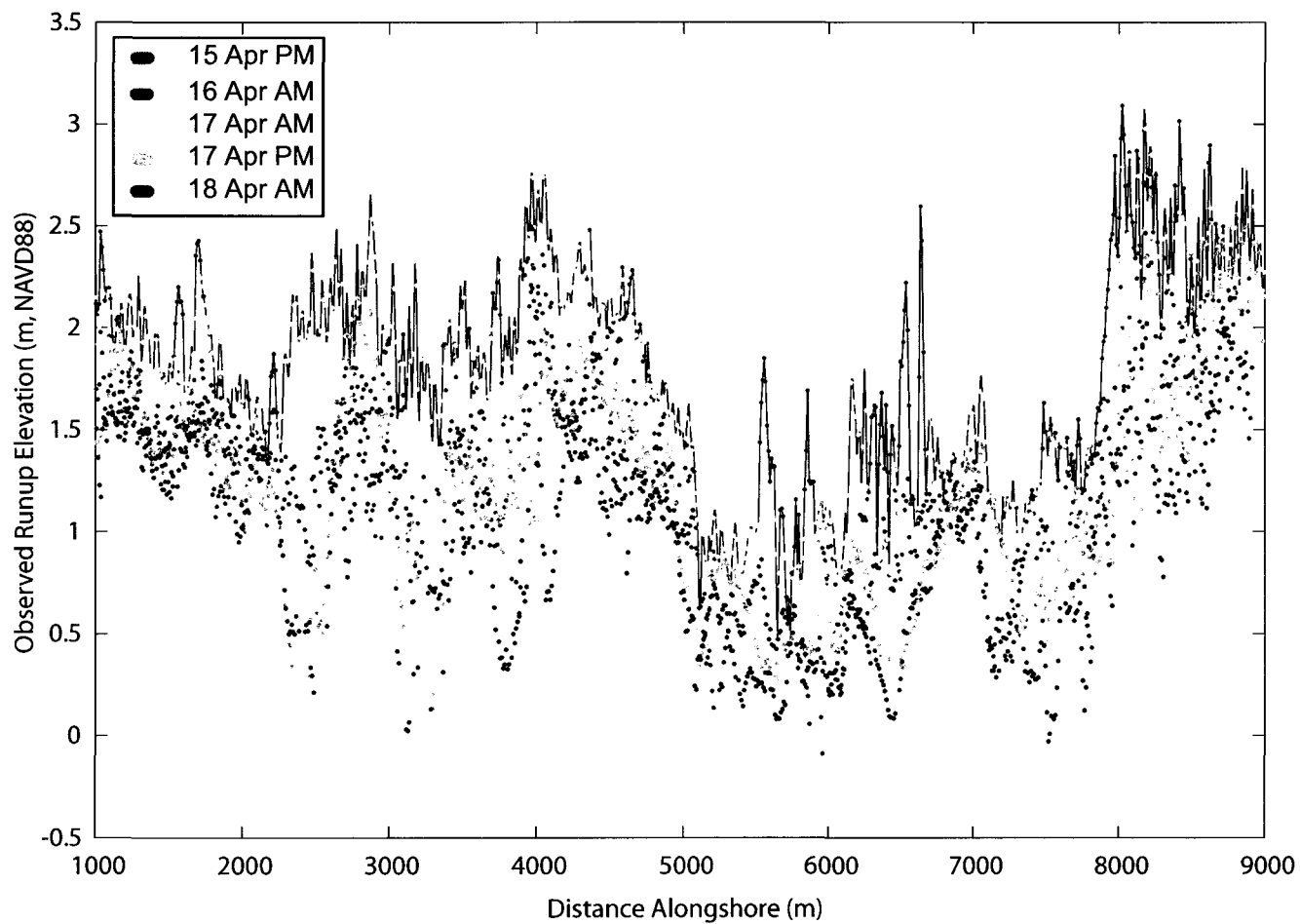


Figure 5.

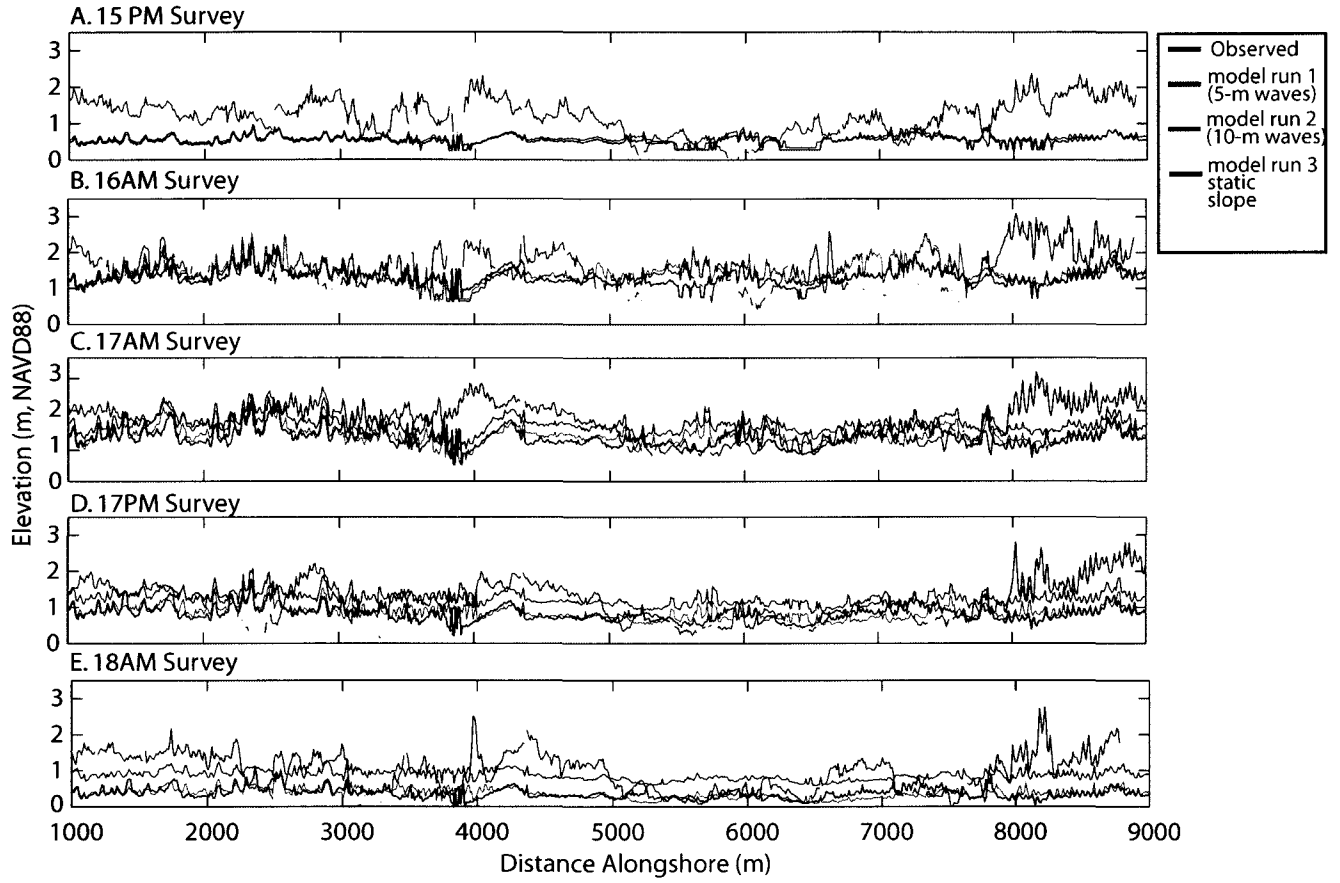


Figure 6

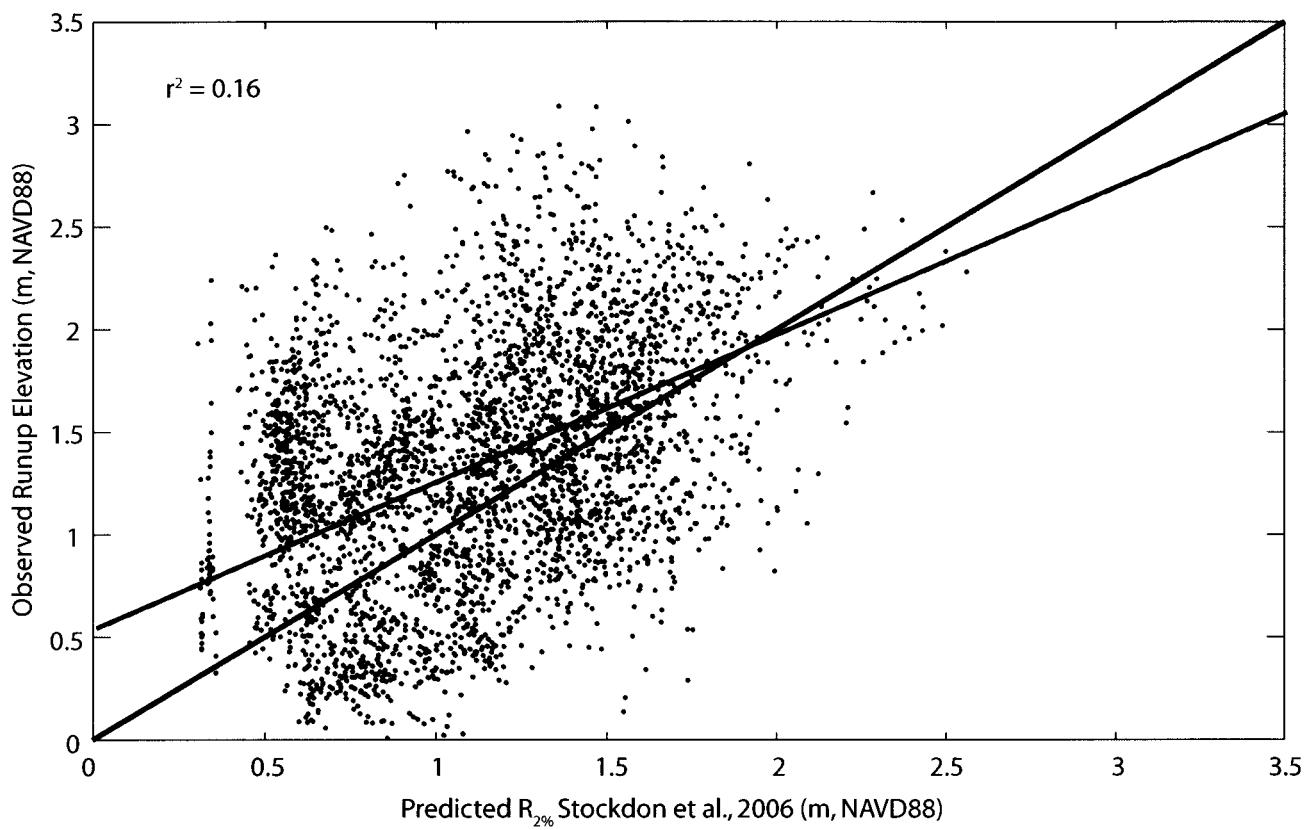


Figure 7.

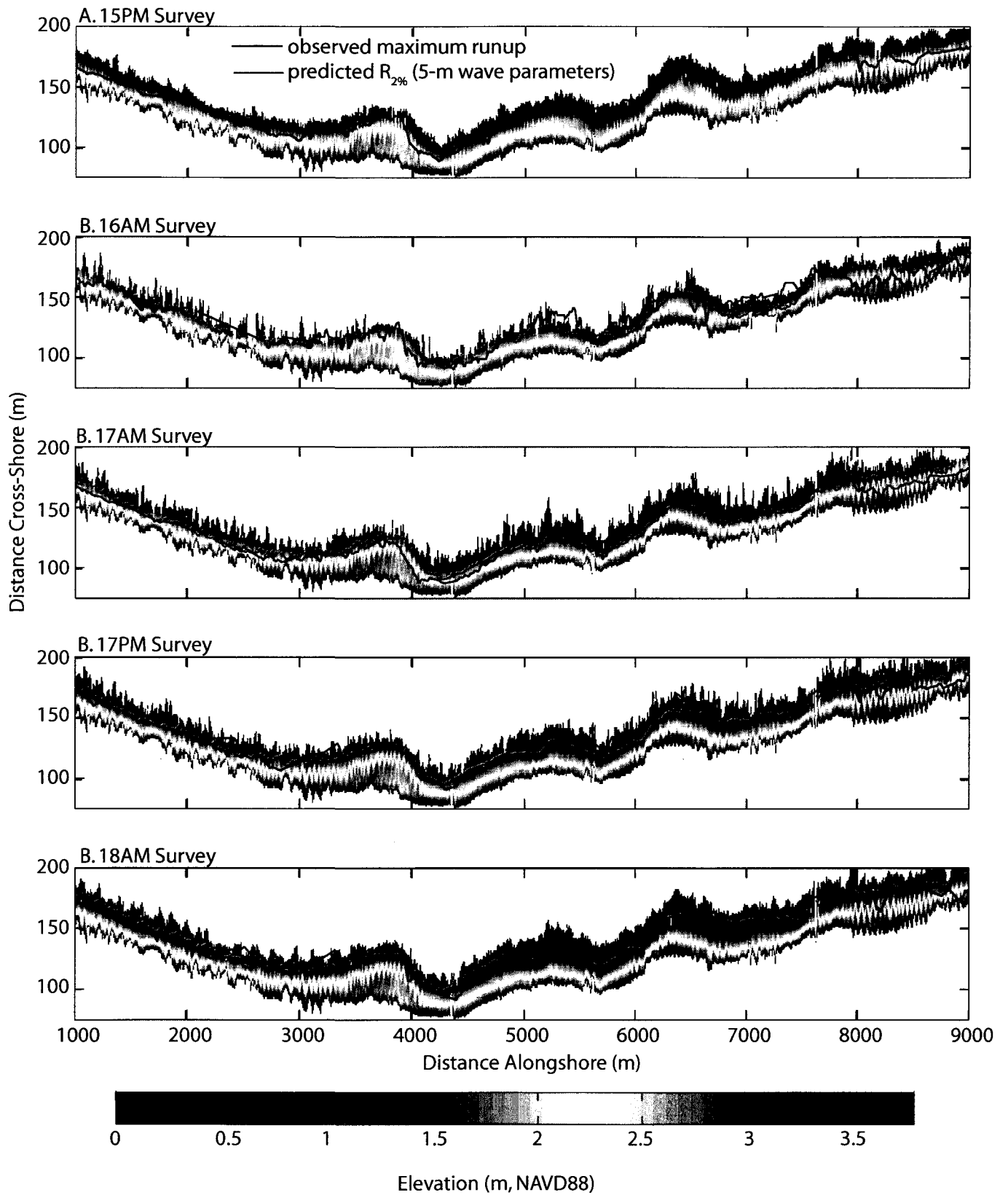


Figure 8.

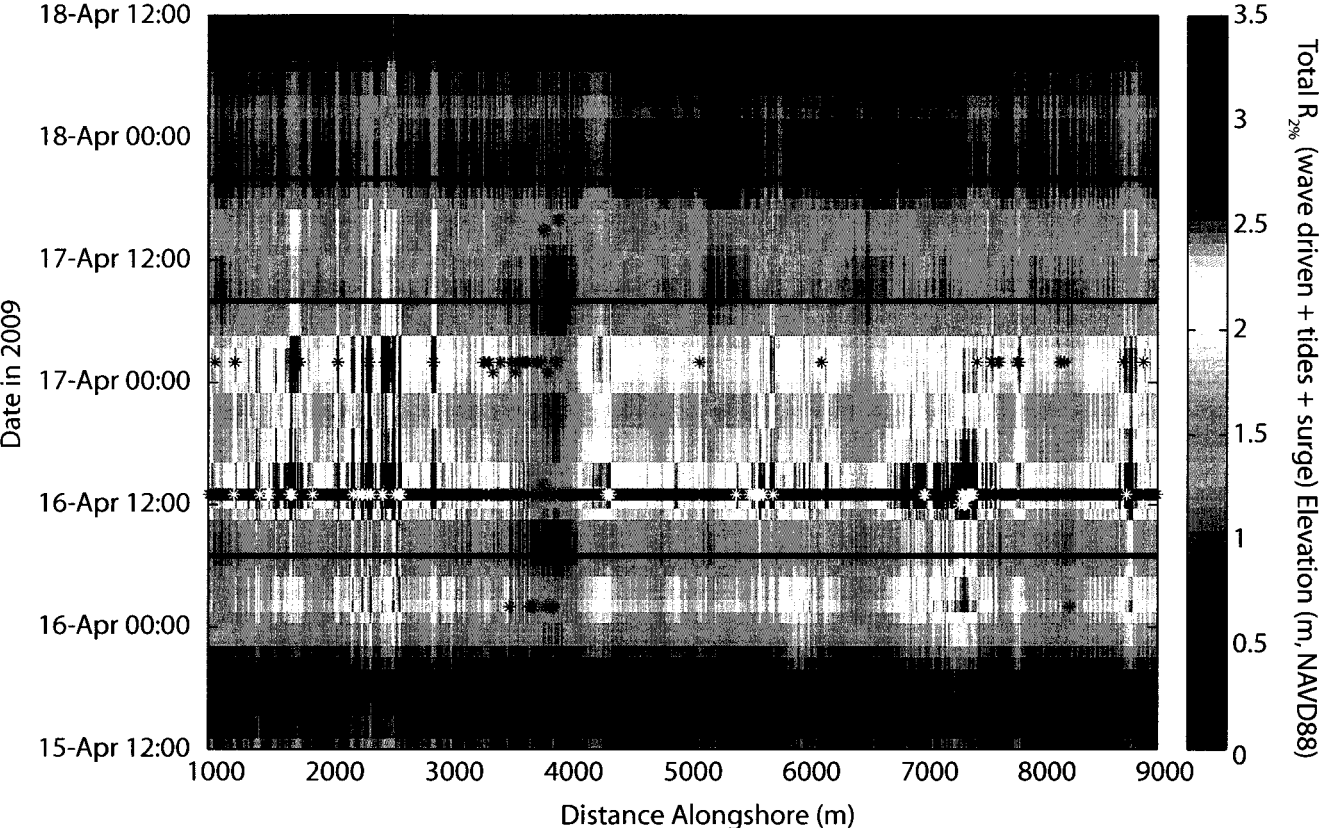


Figure 9.

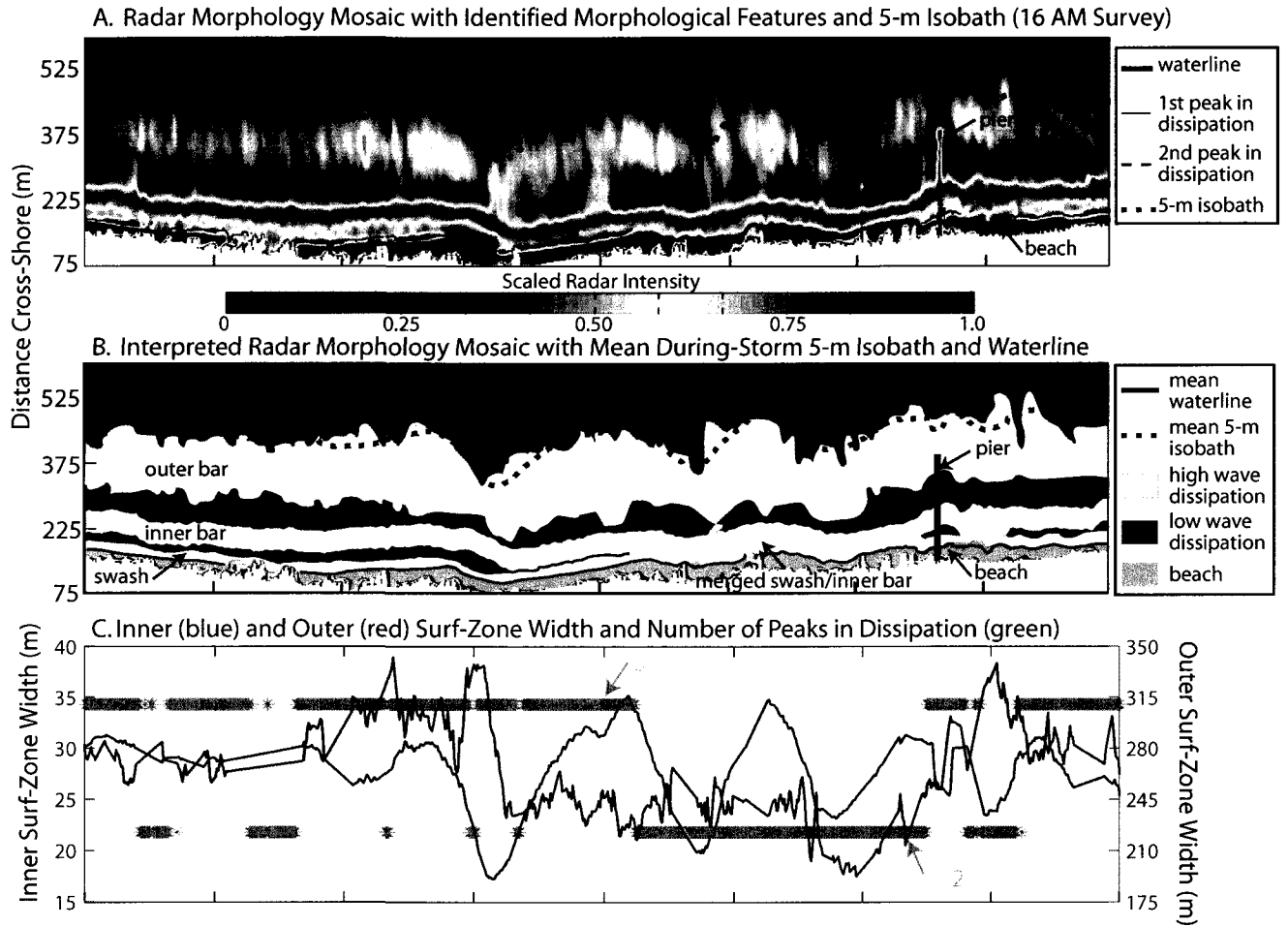
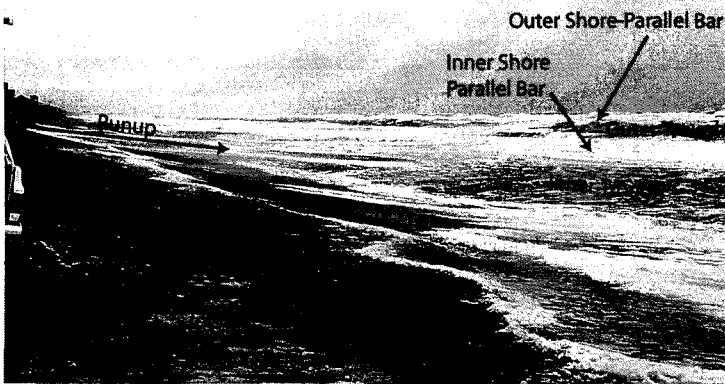
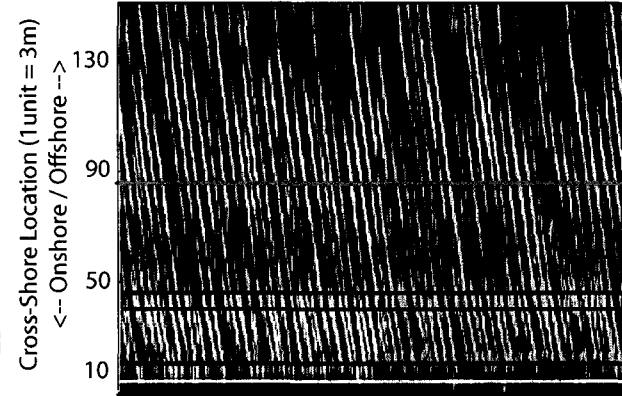


Figure 10.

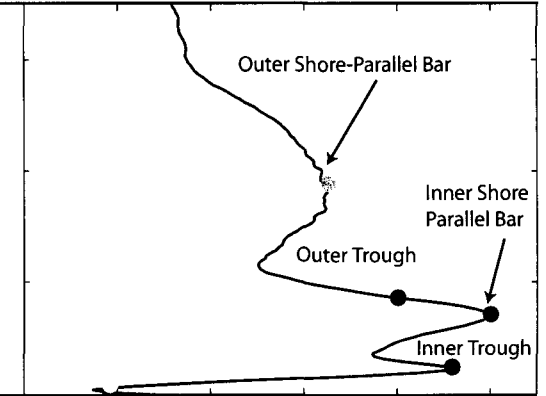
A. Photograph of Double-Barred Regeion



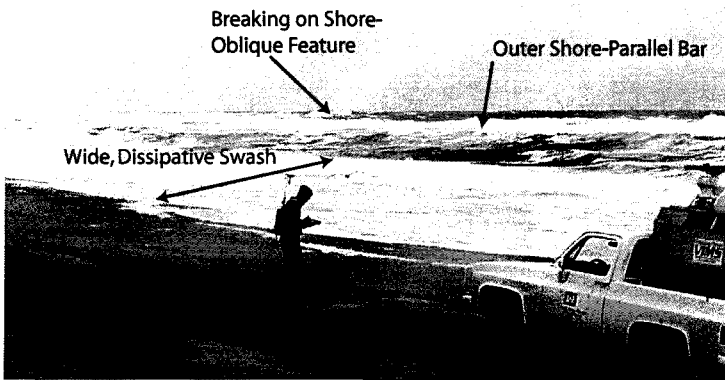
B. Time Stack of Radar Intensities - 2740m Alongshore



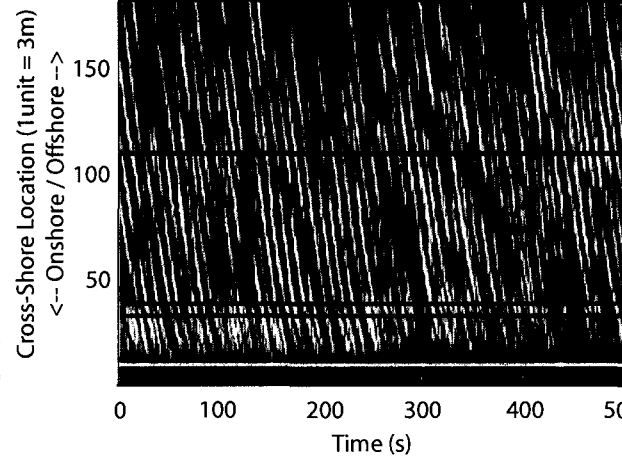
C. Time-averaged Radar Intensity Profile



D. Photograph of Single-Barred Regeion



E. Time Stack of Radar Intensities - 5863m Alongshore



F. Time-averaged Radar Intensity Profile

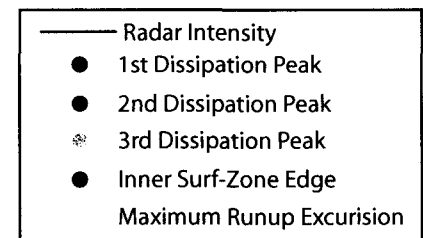
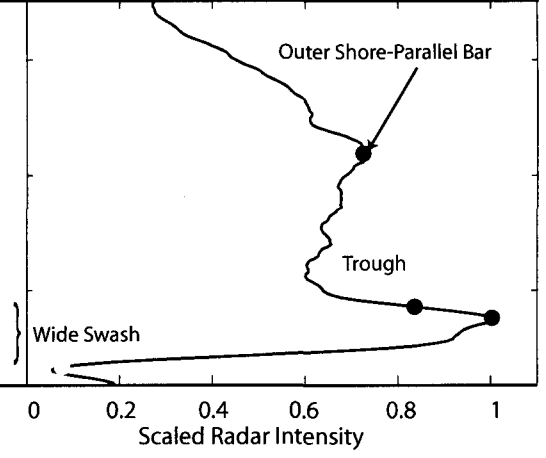


Figure 11.

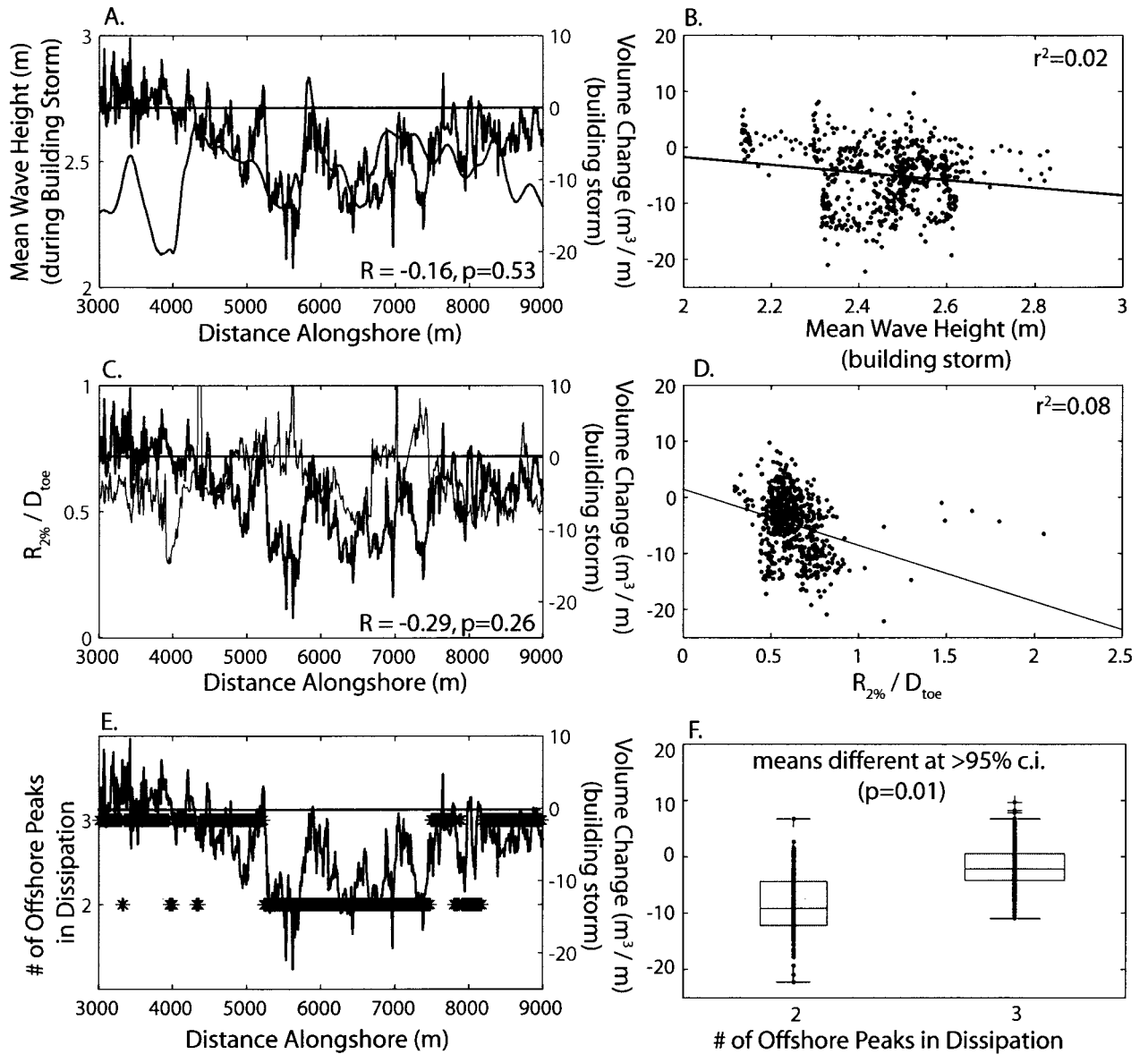


Figure 12.

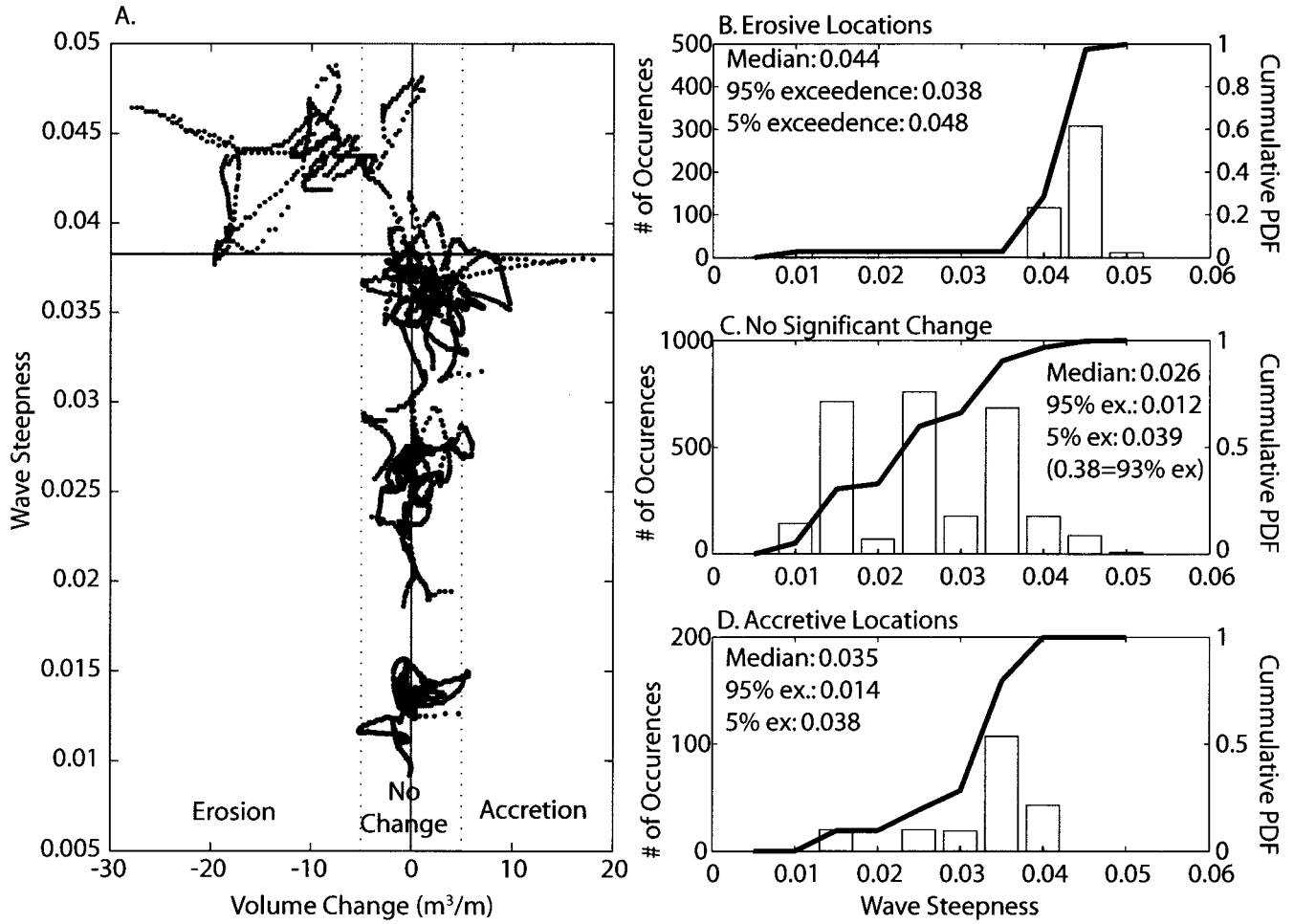


Figure 13.

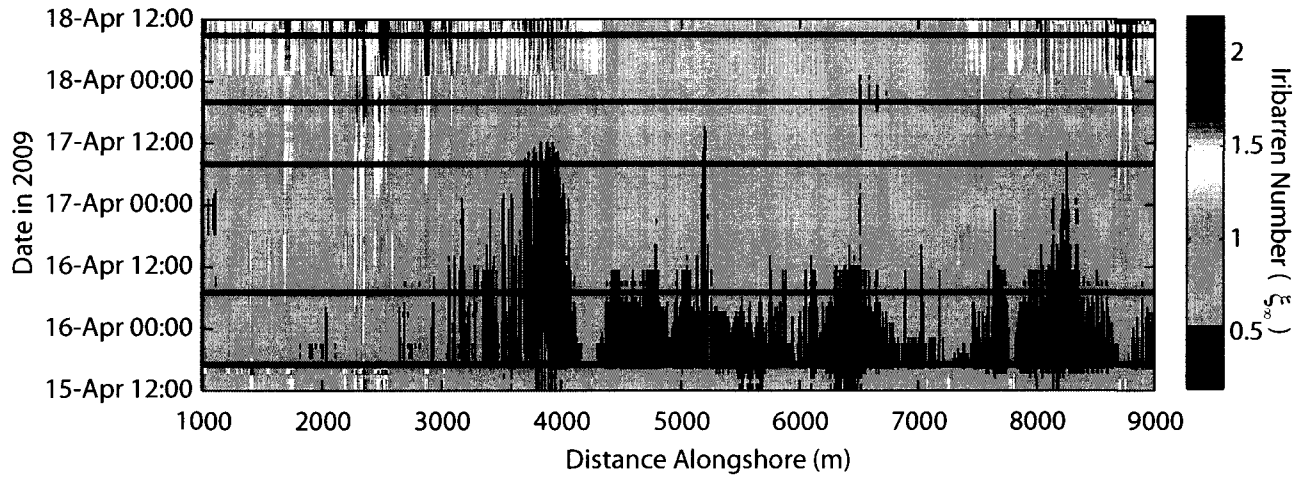


Figure 14.

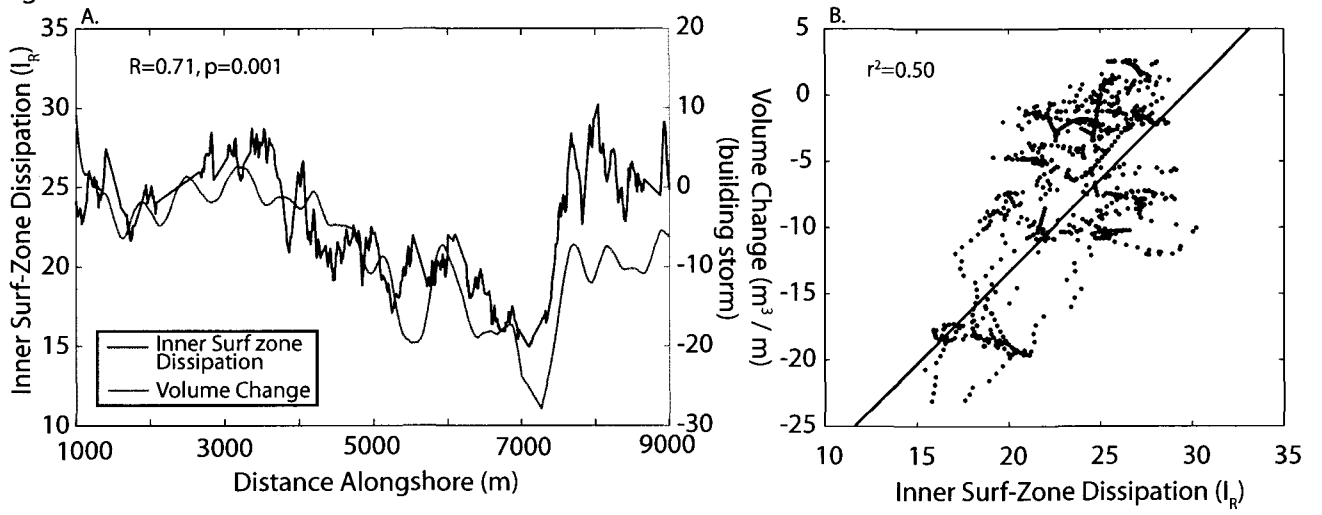


Figure 15.

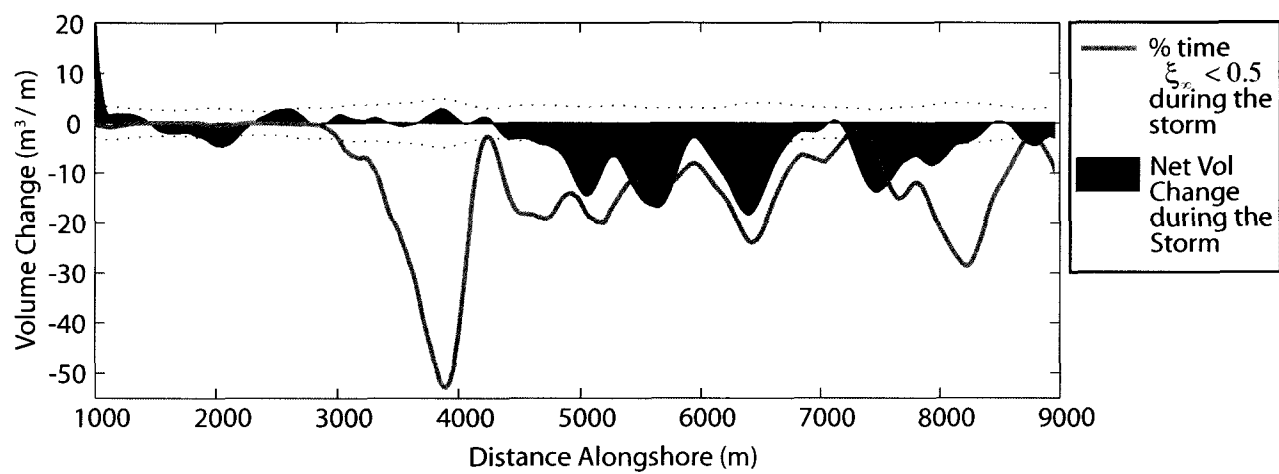
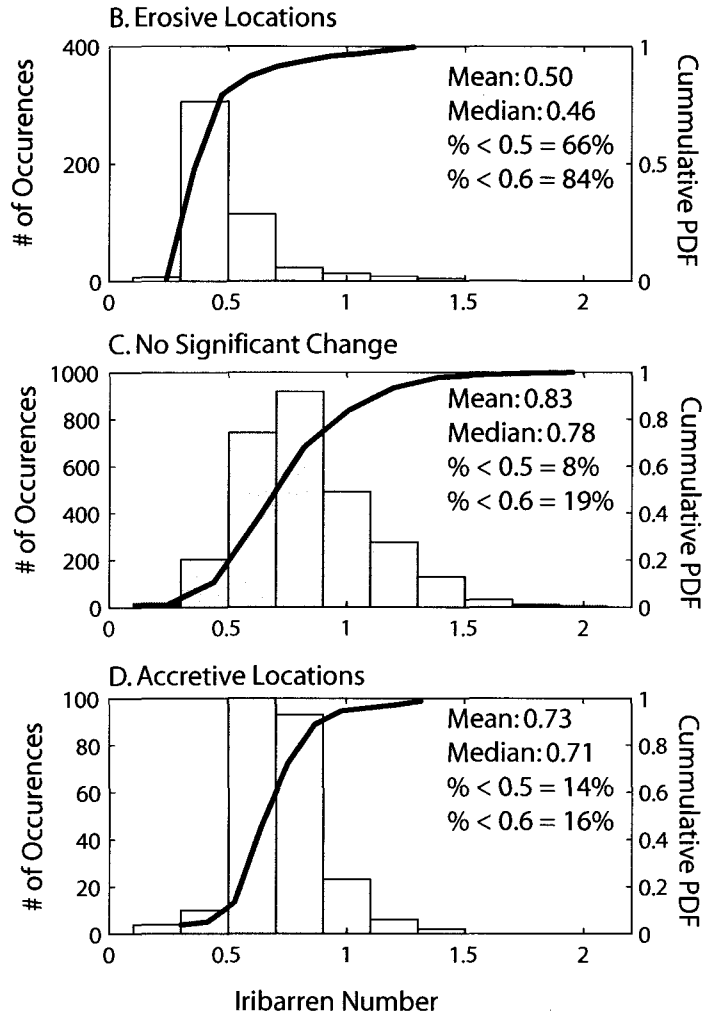
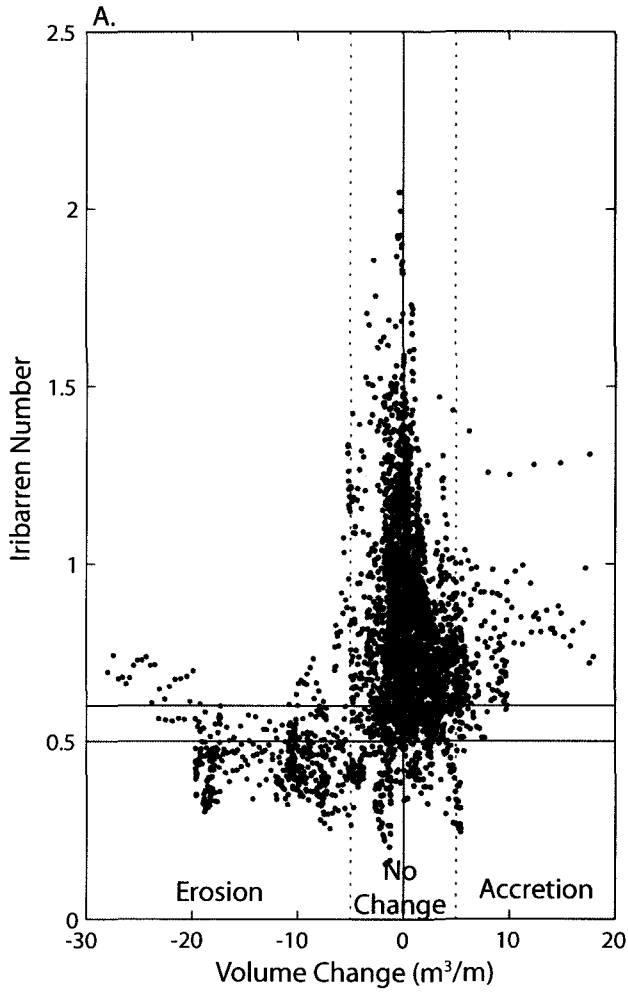


Figure 16.



VITA

Katherine L. Brodie

Born in Duxbury, Massachusetts, 13 October 1984. Graduated magna cum laude from Milton Academy in Milton, Massachusetts. Earned a B.A. in Earth Sciences with High Honors from Dartmouth College in Hanover, New Hampshire, graduating magna cum laude in 2006. At Dartmouth, was the 2006 recipient of the Upham Award in the Earth Sciences department for best senior thesis, and the 2005 recipient of the Estwing Award in the Earth Sciences department for outstanding work in a collaborative environment. Entered the masters of science program at the College of William and Mary, School of Marine Science in 2006, receiving the William J. Hargis, Jr. Fellowship Award in 2007 for superior academic performance in the first year of study. Successfully by-passed the masters of science degree, entering the doctoral program in June of 2009. Graduate work received outstanding student paper awards in 2008 and 2009 at the American Geophysical Union Fall Meeting in San Francisco, California. Will graduate in May 2010 with a Ph.D. in Marine Science, with a concentration in geological oceanography.